Systematic analysis of nuclear reactions with a neutron rich projectile on multiple targets at intermediate energies

A thesis presented for the degree of

Doctor of Philosophy (Ph.D.)

by

Sahil Upadhyaya

Supervisor

T. Kozik

dr hab. Tomasz Kozik

prof. UJ

Marian Smoluchowski Institute of Physics
Jagiellonian University, Kraków, Poland
2017-2021

This thesis is dedicated to my grandparents

Acknowledgement

This thesis would not have been possible without the expertise of my supervisor, dr hab. Tomasz Kozik, who has helped me in every way throughout this journey of my doctoral studies. I would like to thank Dr Diego Gruyer and dr hab. Katarzyna Mazurek for their time and constant support in completing the doctoral research work. A special thanks to the whole FAZIA collaboration for giving me a chance to work with them. I thank dr inż. Michał Ciemała for his help with the GEMINI++ simulations. I would like to thank the Jagiellonian University, Kraków for awarding me the DSC-2018 grant (K/DSC/005311/2018) which helped in facilitating the doctoral research work. A big thanks to Dr Sushil Sharma and Dr Vivek Parkar for their support. I thank my parents, uncle, aunt and the rest of the family for their constant encouragement and support. I also thank all my friends, especially, Magdalena, Narendra, Udai, Akshay and Arun, without whom this journey would not be so easy.

Abstract

Heavy-ion collisions at intermediate energy range (10-100 MeV/A) have been studied since a long time. These studies are used to put constraints on the symmetry energy term (E_{sym}) of the nuclear equation-of-state (EoS). The E_{sym} can be investigated by studying the isospin (N/Z) transport in these nuclear reactions. The FAZIA (Four-π A and Z Identification Array) collaboration aimed at improving the charged particle identification techniques such as pulse-shape analysis (PSA) and $\Delta E-E$ method. After many years of R & D, the FAZIA detector is now capable of a full Z identification and A identification up to $Z \sim 25$. With this excellent isotopic resolution capability, it is possible to study the N/Z of the reaction products from nuclear reactions at intermediate energies. This doctoral research work is focused on the analysis of the data from the FAZIA-PRE experiment performed at LNS-INFN, Italy in February 2018. The objective of the experiment was to study the effects of pre-equilibrium neutron emissions from a neutron rich projectile on the N/Z of reaction products. A neutron rich projectile (^{48}Ca) was bombarded on 3 different targets (^{12}C, ^{27}Al and ^{40}Ca) at 25 and 40 MeV/A. The dependence of the target mass and beam energy on various reaction observables such as charge (Z), mass (A), multiplicity of charged particles (M_{tot}), longitudinal (parallel) velocity ($v_{||}$) and fragment isospin (N/Z) was studied. Furthermore, a detailed comparison of experimental data with the HIPSE model simulations was also done in order to study HIPSE's performance with respect to intermediate energy nuclear reactions.

Contents

List of Tables

List of Figures

Chapter 1

Introduction

1.1 Heavy-ion collisions

The heavy-ion collisions in the nucleonic regime have been of interest in understanding the evolution of the reaction initiating from a highly out-of-equilibrium picture towards a possible post-dissipation thermalized system. The reaction products of these heavy-ion collisions are in extreme states, i.e., they can consist of either very hot or highly exotic nuclei. Excitation energies of the hot nuclei can be close to or even higher than their total binding energies. Studies concentrated at investigating the physics of hot nuclei greatly depend on the physics of the reaction mechanisms, which are accessed through their de-excitation. These signals from the de-excitation processes spread light on the complex dynamical aspects of the reaction. On the other hand, the exotic nuclei have unusual neutron-to-proton (N/Z) ratios. It is important to investigate their static as well as dynamical properties. These can be addressed by using macroscopic or a microscopic approaches involving the constituents of nuclei.

Heavy-ion collisions constitute an important tool to investigate the properties of nuclear matter in large regions of the nuclear phase diagram [1] (see Fig. 1.1) both near and far from normal conditions (temperature T = 0 MeV, nuclear density $\rho = \rho_0 \approx 0.16$ fm^{-3} ; ρ_0 is called the nuclear saturation density). Multiple regions of the phase diagram are explored during these reactions. Away from the normal conditions, the system can experience a compression and then a following expansion and vaporisation [2]. These collisions enable the investigation of different nuclear degrees of freedom that come into play. They also have dependence on the energy and time scale of the collision. During the collisions, the matter gets compressed and becomes hot. Based on initial conditions, different ranges of T and ρ can be addressed and a large scale study of the nuclear matter phase diagram can be made possible from ground state nuclear interaction up to the astrophysical phenomena in supernovae or neutron stars.

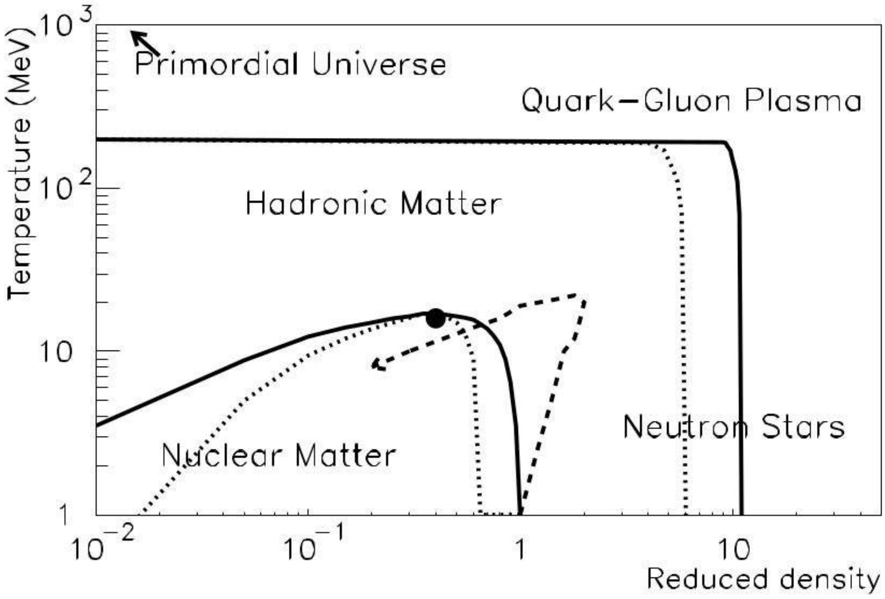

Fig. 1.1: Phase diagram (reduced density ρ/ρ_0 versus temperature T) of nuclear matter. From [1].

1.1.1 Description on the basis of incident energy range

The exploration of a particular region on the phase diagram greatly depends on the beam energy (E_B) and consequently on the relative velocity (v_{rel}) between the reaction participants. The reduced wavelength of the nucleonic collisions corresponding to the v_{rel} is given by,

$$\lambdabar = \frac{\hbar}{m_u v_{rel}} \tag{1.1}$$

where $m_u = 1.66\text{x}10^{-27}$kg is 1 atomic mass unit and $\hbar = h/2\pi$ where h is the Planck's constant. Depending on the value of $\lambdabar$, there can be two scenarios. First, if the value of $\lambdabar$ is greater than the mean distance between two nucleons inside a nucleus (~ 2 fm), which means that the v_{rel} corresponds to the value of incident energy in the low energy domain, usually $E_B < 10$ MeV/A. In this case, the available energy is not sufficient to excite the nucleonic degrees of freedom. This increases the probability of nucleon free states to be excited because of the Pauli exclusion principle which is strongly followed here. Hence, the mean field effect of nucleonic interactions is considered (1-body dynamics). Thus, when individual nucleon interacts with a collective mean field, the thermalization time is given by,

$$\tau_{mf} \approx \frac{R}{v_F} \tag{1.2}$$

where R is the sum of radii of two interacting nuclei and v_F (~ $0.3c$) is the Fermi velocity. In the second case, if the value of $\lambdabar$ is smaller than the size of the nucleon, the elastic collisions between two separate nucleons are considered, i.e. 2-body collision dynamics.

This corresponds to the high energy collision regime (E_B >200 MeV/A). Here, the available energy is sufficiently high to excite the intrinsic degrees of freedom of the nucleons leading to formation of hadronic cascades. The Pauli exclusion principle is neglected in this case. The thermalization time becomes similar to the order of the time between two successive nucleon-nucleon collisions and is given by,

$$\tau_{nn} = \frac{1}{\sigma_{nn}\rho_0 v} \tag{1.3}$$

where σ_{nn} is the nucleon-nucleon cross-section and v is mean velocity of the order of v_F.

The reaction dynamics have been well studied for these incident energy ranges (for example [3–6]). But the challenging case comes while investigating heavy-ion collisions in the range of intermediate incident energy, $\sim 10-200$ MeV/A (also called the Fermi energy range around $\sim$ 30 MeV/A). The intermediate energy range seems to be an interesting region in which nuclear matter is heated and compressed within a broad range of temperatures and densities. In this energy regime, the effects of mean field and 2-body dynamics come into competition. Here, the thermalization time becomes comparable to the interaction time and is given by,

$$\tau_{int} = \frac{R}{v_{rel}} \tag{1.4}$$

Given the fact that the thermalization and interaction times are comparable to one another, there can be two processes:

- A substantial amount of the available energy might be thermalized leading to the formation of very hot excited nuclei from nucleus-nucleus collisions.
- A substantial amount of the available energy might not be thermalized leading to fast emissions, also known as pre-equilibrium emissions [7, 8]. The rate of these emissions largely varies with respect to the initial geometry (impact parameter) and the rate of thermalization.

A brief description of pre-equilibrium emissions can be given with the help of the Fig. 1.2. It shows a schematic representation of two centrally colliding (see § 1.1.2) symmetric nuclei (black circles) in momentum space with relative incident energy around 100 MeV/A. In this case of central collision, fusion is expected to happen. The separation between the nuclei equals the relative velocity between the them corresponding to the incident energy. The red dotted circle corresponds to the sphere of the fusion nucleus located in the middle of both interacting nuclei due to their masses being symmetric. The blue dotted circle corresponds to nucleons that have slightly more velocities due to thermal motion inside the hot fusion nucleus. They are generally trapped within this region. But the nucleons which are outside from this fusion region can escape the interacting system in the form of single nucleons or clusters. The particles escaped in such case as separate nucleons, light charged particles (LCPs) or intermediate-mass fragments (IMFs) correspond to the so called “fast” or pre-equilibrium emissions (marked as Pre-Eq in the Fig. 1.2).

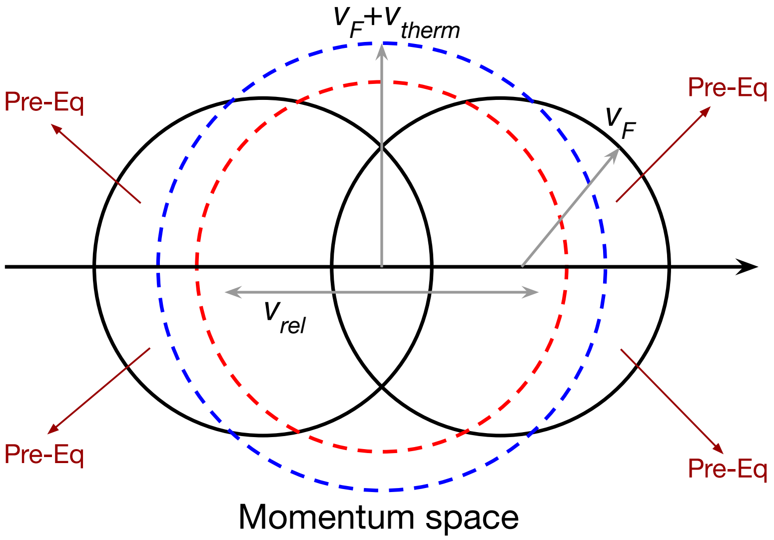

Fig. 1.2: A schematic representation of two colliding nuclei at a relative incident energy of 100 MeV/A for a symmetric entrance channel. The red dotted circle is the Fermi sphere of the fusion nucleus and the blue dotted one corresponds to an extra thermal velocity. Nucleons located outside the blue circle can escape and are called pre-equilibrium emissions (Pre-Eq). Figure and caption adapted from [1].

In the aforementioned intermediate energy range, intrinsic states of the nucleon are not excited from the energy dissipated in the nucleus. This leads to the nuclear matter to get heated up. Also, fraction of this energy is used to excite collective degrees of freedom corresponding to rotation, deformation and/or compression. The proportion of energy used for a given mode depends on the specific timescales for its excitation and also on the initial conditions, i.e. the entrance channel characteristics. One important observable in those characteristics is the impact parameter.

1.1.2 Classification along the impact parameter

The impact parameter (b) in a reaction is basically the distance between the centres of the nuclei of initial reaction partners measured perpendicularly with respect to the beam axis. The measure of b denotes the centrality of the collision. The smaller the value of b, the more is the centrality. Depending on b, there can be central, mid-central and peripheral collisions.

The Fig. 1.3(a) shows the time evolution of a perfectly central collision ($b = 0$) for ^{124}Sn+^{124}Sn reaction at 50 MeV/A. In this energy range, as discussed earlier, the central collisions lead to pre-equilibrium emissions that constitute a significant part of the system in that event. This leads to the formation of a smaller compound nucleus (CN) type structure which has relatively lesser mass and excitation energy (incomplete fusion). But with a substantial excitation energy ($\sim 3-5$ MeV/A), the CN system can decay into smaller fragments via multifragmentation [10].

On the other hand, the Fig. 1.3(b) shows the time evolution of a peripheral collision (b = 6) for ^{124}Sn+^{124}Sn reaction at 50 MeV/A. The peripheral and mid-central collisions at intermediate energy range are generally dominated by binary events. The two main fragments after the primary collision in this case are called quasi-target (QT) and quasi-projectile (QP). The reaction times being sufficiently smaller in this energy range that the QT and QP retain the entrance channel memory, i.e., of the target and projectile, respectively. Their velocities are also close to the centre-of-mass velocities corresponding to the incident energy. During secondary decays, the moderately excited QT and QP decay by emitting smaller particles, generally IMFs [11–14], in a wide range of longitudinal velocity. The final reaction products remaining from QT and QP resemble the target and projectile nucleus. They are called target-like fragments (TLFs) and projectile-like fragments (PLFs). The dissipation increases with increasing energy or decreasing impact parameter. This results in a decreasing cross-section ultimately making the existence of TLF and PLF questionable.

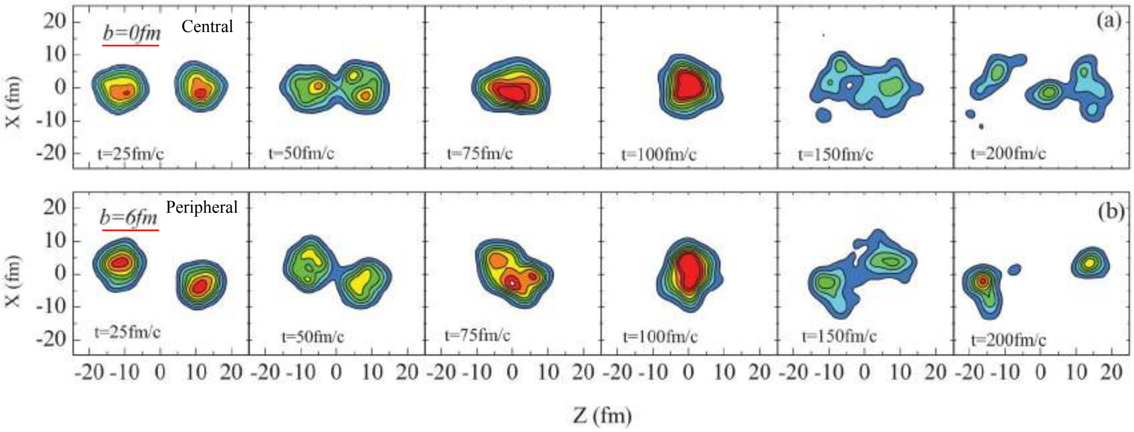

Fig. 1.3: Time evolution of the nucleon density in the reaction plane for ^{124}Sn+^{124}Sn collisions at E_B = 50 MeV/A at (a): b = 0 fm (central collision) and (b): b = 6 fm (peripheral collision). Taken from [9].

Another important aspect of peripheral collisions at intermediate energies is the formation of neck-like structures. In the overlap region of the two initial nuclei, a highly dense and hot region of nuclear matter is produced. This region formed by the overlap of projectile and target is called a neck. In many cases this may become an independent source of emission besides QT and QP. A substantial amount of the emitted fragments may then be concentrated in the mid-velocity region. The fragments emitted from the neck at mid-velocities are mostly light IMFs (Z ~ 3−10) and LCPs [15–17]. The fragmentation of the neck happens basically due to the occurrence of surface instabilities [18]. In particular, in the dynamics of the collision, the overlap region may become very stretched thus leading to formation of possible mechanical ruptures. It is established that neck emissions are connected to the geometrical overlap during of the colliding nuclei [12]. Depending on extent of the overlap, it may either lead to a separate source of nuclear matter or it may be released attached to one of the partners [19].

The influence of the isospin (N/Z) degree of freedom on the composition of the matter produced in the neck region is also a very important topic, especially for this research. Multiple experimental results [20,21] have shown that the emitted fragments from the neck are more neutron rich than the expectations considering isospin equilibration of the system. Isospin related phenomena is discussed in detail in the next section.

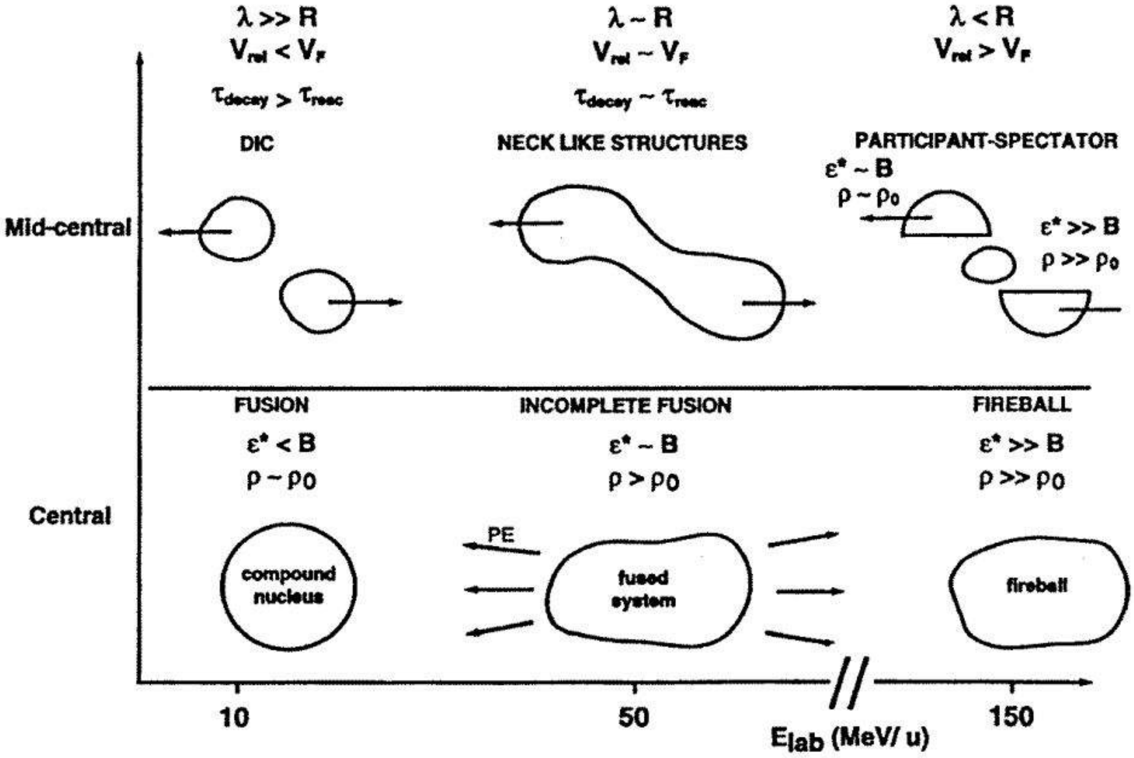

Fig. 1.4: A schematic representation of the various reaction mechanisms occurring in heavy-ion collisions at intermediate energy range. Taken from [1].

So, to summarise the heavy-ion collisions, a schematic representation of the different processes and their evolution as a function of the incident energy is shown in Fig. 1.4. In peripheral/mid-central collisions, pure dissipative collisions are observed around the Coulomb barrier. With increasing incident energy, the system appears to have deformed overlapping neck regions. Above ~100 MeV/A, as the mean free path becomes shorter and the relative velocity becomes significantly larger, the participant–spectator picture comes at play. On the other hand, for central collisions, as incident energy increases, the complete fusion induced CN production becomes less and less probable due to increase of other processes like pre-equilibrium emissions. This leads to formation of a not fully thermalized system (incomplete fusion). At very high energies, where the excitation energies become similar to or greater than the total binding energy of the system, the production of very hot and compressed nuclear matter occurs, which is called a fireball.

1.2 The nuclear equation-of-state and its symmetry energy term

The nuclear Equation-of-State (nEoS) is one of the fundamental properties of the nuclear matter which can describe not only terrestrial nuclei but also astrophysical objects and phenomena. It can help to understand an extremely large range of physical systems and processes, such as reaction mechanisms in laboratory experiments, exotic nuclei, heavy-ion collisions, physics of astrophysical objects like neutron stars, supernovae, binary mergers, etc. Lot of work has been done to put constraints on the nEoS around the nuclear saturation density (ρ_0) [22]. In ground state conditions, the nuclear properties can be understood on the basis of the elementary Bethe-Weizsäcker formula for binding energy given by,

$$B.E. = a_V A - a_S A^{2/3} - a_C \frac{Z^2}{A^{1/3}} - a_A \frac{(A-2Z)^2}{A} \pm \delta(A,Z) \tag{1.5}$$

where Z is the charge of the nucleus, $A(=N+Z)$ is the mass and $\delta(A,Z)$ is the pairing term. The parameters a_V, a_S, a_C and a_A are volume energy, surface energy, Coulomb energy and asymmetry energy coefficients, respectively.

But, far from the normal conditions, the nEoS is still not very well constrained and understood. When there are different conditions like neutron-proton asymmetries, extreme temperature and density variations, then the treatment is different and the nuclear symmetry energy is introduced. Many studies have been done for asymmetric nuclear matter and the symmetry energy term of the nEoS [22–32] This symmetry energy is studied as a function of neutron and proton densities (ρ_n, ρ_p). So, the nEoS then can be written as [31, 32],

$$\frac{E}{A}(\rho, I) = \frac{E}{A}(\rho) + \frac{E_{sym}}{A}(\rho) I^2 + ... \tag{1.6}$$

$$E_{sym}(\rho) = \frac{1}{2} \frac{\partial^2 E(\rho, I)}{\partial I^2}\bigg|_{I=0} \tag{1.7}$$

where $\rho = \rho_n + \rho_p$ is the nucleonic density, $I = (\rho_n - \rho_p)/\rho$ is the isospin asymmetry and E_{sym} is the symmetry energy. Multiple mathematical approaches have been done to develop model predictions for the nEoS. Some of these approaches include:

- phenomenological density functionals – effective density dependent interactions such as Gogny [33, 34] or Skyrme forces [35, 36] or relativistic mean field (RMF) models [37]

- effective filed theory approaches based on density functional theory [38, 39] or on chiral perturbation theory [40–42]

- Ab initio approaches like variational calculations [43, 44], Brueckner-Hartree-Fock (BHF) [45–48] or relativistic Dirac-Brueckner-Hartree-Fock (DBHF) [49–55] calculations and Greens functions Monte-Carlo approaches [56–58].

Symmetry energy predictions as a function of density from most of these approaches are put together and shown in Fig. 1.5.

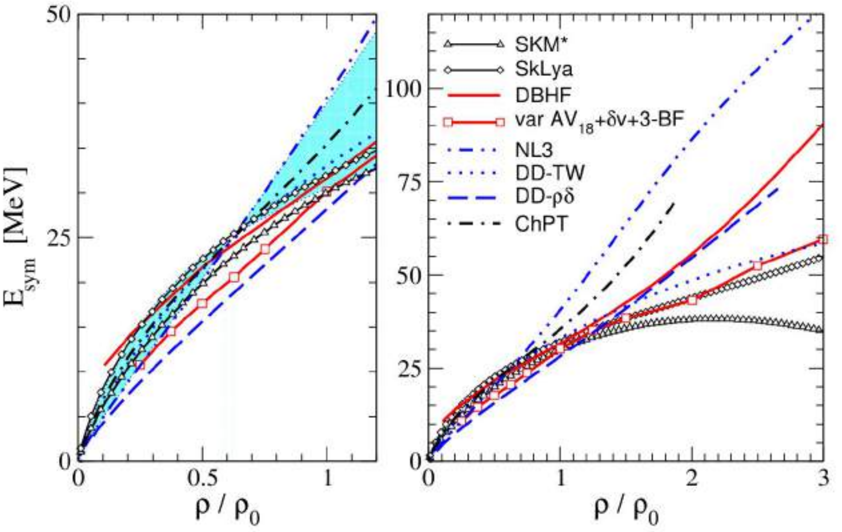

Fig. 1.5: Symmetry energy as a function of density as predicted by different models. The left panel shows the low density region while the right panel displays the high density range. Taken from [32].

Further, it can be useful to do a Taylor series expansion of the symmetry energy term $E_{sym}(\rho)$ in Eq. 1.6 around the saturation density, ρ_0, where the binding energy of symmetric nuclear matter becomes maximum at ~16 MeV. The expansion is given by [59],

$$E_{sym}(\rho) = E_{sym}(\rho_0) - L\epsilon + 1/2K_{sym}\epsilon^2 + O[\epsilon^3] \qquad (1.8)$$

where $\epsilon \equiv (\rho_0 - \rho)/3\rho_0$. L and K_{sym} denote the slope and curvature at ρ_0. Also, L can be written as,

$$L = 3\rho_0 \left.\frac{dE_{sym}(\rho)}{d\rho}\right|_{\rho_0} = \frac{3P_0}{\rho_0} \qquad (1.9)$$

Here, P_0 denotes the pressure from $E_{sym}(\rho_0)$ in pure neutron matter and also contributes to the pressure in neutron stars [60]. This provides a link to the astrophysical regime through L. The value of $E_{sym}(\rho_0)$ and L have been estimated from various terrestrial and astrophysical observations shown in Fig. 1.6. The average values calculated for $E_{sym}(\rho_0) = 31.6\pm0.9$ MeV and for $L = 59\pm17$ MeV.

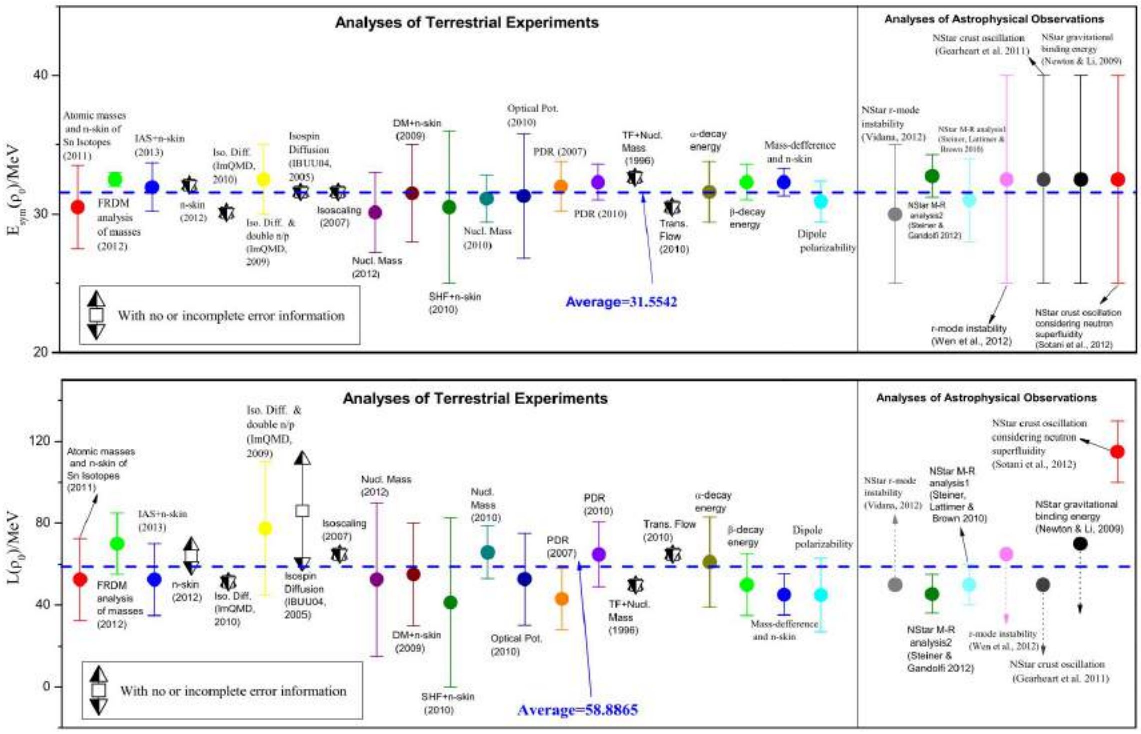

Fig. 1.6: Nuclear symmetry energy (upper) and its slope L (lower) at normal density of nuclear matter from 28 analyses of terrestrial nuclear laboratory experiments and astrophysical observations. Taken from [61].

The density dependence of the E_{sym} can be visualised by using, for example, the stochastic mean-field (SMF) transport approach. The E_{sym} from Eq. 1.6 can be written as a sum of its kinetic and potential parts [25] as,

$$E_{sym} = E_{sym}(kinetic) + E_{sym}(potential) \equiv \frac{\epsilon_F}{3} + C_{sym}(\rho) \tag{1.10}$$

There are three different density parametrizations of the symmetry potentials [2, 62, 63]:

- strong density dependence ($\propto\sim \rho^2$) – Asy-superstiff,

$$E_{sym}(\rho) = a\left(\frac{\rho}{\rho_0}\right)^{2/3} + b\frac{2(\rho/\rho_0)^2}{1+(\rho/\rho_0)} \tag{1.11}$$

- linear dependence on density – Asy-stiff,

$$E_{sym}(\rho) = a\left(\frac{\rho}{\rho_0}\right)^{2/3} + b\frac{\rho}{\rho_0} \tag{1.12}$$

- weaker density dependence with saturation around ρ_0 and further decreasing – Asy-soft,

$$E_{sym}(\rho) = a\left(\frac{\rho}{\rho_0}\right)^{2/3} + 240.9\rho - 819.1\rho^2 \tag{1.13}$$

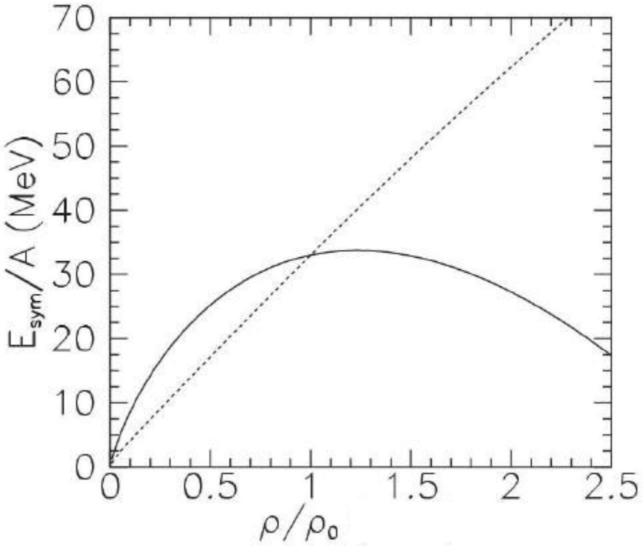

Fig. 1.7: Density dependence of the symmetry energy for Asy-soft (solid) and Asy-stiff (dashed) cases. Taken from [25].

These three conditions intersect at normal density at the value of the asymmetry energy coefficient a_S of Eq. 1.5. The Fig. 1.7 shows the symmetry energy as a function of density for linear and weak dependence. It can be seen that at sub-normal densities ($\rho < \rho_0$) the E$_{sym}$ is larger for Asy-soft case, whereas, at supra-normal densities ($\rho > \rho_0$), the Asy-stiff case has higher E$_{sym}$. So, due to higher value of E$_{sym}$ in the low density region, the isospin effects in the heavy-ion collisions at intermediate energies are stronger. Thus, this is an important point concerning the research work done in this thesis.

1.2.1 Isospin transport

It was discussed that the nEoS can be constrained with the help of the E_{sym}. Specific constraints can be put on E_{sym} by studying processes governed by it, such as isospin (N/Z) equilibration during the reaction. Isospin transport phenomena is a process that is responsible for the isospin equilibration of the reaction system. It basically refers to the migration of nucleons during the reaction process among the participants. The migration of nucleons is controlled by the spatial gradients of their corresponding chemical potentials, μ_q (ρ_p, ρ_n, T), where q can be either proton (p) or neutron (n) and T denotes the temperature. The nucleon current then can be written as [2, 30],

$$\vec{j}_q = -Ct\nabla\mu_q(\rho_p, \rho_n, T) = D^{\rho}_q\nabla\rho - D^{I}_q\nabla I \qquad (q = p, n) \tag{1.14}$$

where C is a constant and D^{ρ}_q and D^{I}_q are drift and diffusion coefficients, respectively. They can be written as,

$$D^{\rho}_q = Ct\left(\frac{\partial\mu_q}{\partial\rho}\right)_{I,T} \tag{1.15}$$

$$D^I_q = -Ct\left(\frac{\partial \mu_q}{\partial I}\right)_{\rho,T} \tag{1.16}$$

In terms of difference of proton and neutron current,

$$\vec{j}_n - \vec{j}_p = (D^\rho_n - D^\rho_p)\nabla\rho - (D^I_n - D^I_p)\nabla I \tag{1.17}$$

There are two terms in the above equation. The first term represents the nucleon migration in the presence of a density gradient $\nabla\rho$. This is known as "isospin drift". The second term represents nucleon migration in the presence of an isospin gradient ∇I. This is known as "isospin diffusion". These two processes are connected to the E_{sym} by,

$$D^\rho_n - D^\rho_p = 4I\frac{\partial E_{sym}}{\partial \rho} \tag{1.18}$$

$$D^I_n - D^I_p = 4\rho E_{sym} \tag{1.19}$$

Thus, the N/Z equilibration of the system is governed by the isospin drift and isospin diffusion processes. The isospin drift is responsible for neutron transfer from high to low density regions. The isospin diffusion minimizes the N/Z gradient via neutron transfer from a high N/Z region to a low N/Z region.

The degree of equilibration is calculated by the isospin transport ratio given by [30],

$$R_i = \frac{2X^M_i - X^H_i - X^L_i}{X^H_i - X^L_i} \tag{1.20}$$

where X is any isospin sensitive observable, for example ⟨N/Z⟩ of the reaction products and i (= P, T) can be either projectile-like or target-like fragment. M represents a mixed reaction between neutron rich and neutron poor nuclei, H denotes the reaction between both neutron rich nuclei and L stands for both neutron poor nuclei. The degree of equilibration increases as R_i approaches zero. The values $R_P = 1$ and $R_T = -1$ are two extremities indicating no isospin transport.

These studies make the N/Z an important isospin observable that must be investigated to climb up to the steps towards understanding the nuclear equation-of-state. Systems with large N/Z asymmetries reacting at intermediate energies can be used to excite the necessary isospin degrees of freedom. Isospin physics can be then extracted from studying the dynamics of such systems. In this research work, such reaction systems have been studied by systematic comparison of N/Z of the reaction products. But first, the details of the experiment and the apparatus used for these studies are presented in the next chapter.

Chapter 2

The FAZIA detector and FAZIA-PRE experiment

The FAZIA (**F**orward-angle **A** and **Z** **I**dentification **A**rray) collaboration [64] began with the aim of constructing a multi-detector array for improving the charged particle identification methods for heavy-ion collisions around the intermediate energy range (10-100 MeV/A). The detector module is built with an idea of a compact device that can be easily coupled to different detection systems and can be used with stable/radioactive beams in various facilities. The detection modules are combined with high quality digital front-end-electronics developed within the collaboration. The research and development (R&D) phase [65] resulted in unprecedented ion identification capabilities using detector prototypes [66, 67]. With a very good mass resolution for fragments with charge up to Z ~ 20, the detector allows to investigate the isospin related physics in the intermediate energy nuclear collisions, which can also help to constrain the symmetry energy (E_{sym}) term of the nuclear equation-of-state. After the R&D phase, experiments have been performed at INFN-LNS in Catania, Italy, using detector demonstrators consisting of up to around 100 FAZIA telescopes over a period of around 4 years (2014-2018). One of those experiments (FAZIA-PRE - discussed in this chapter in Section 2.4)) is the main topic of the research presented in this thesis. Since 2019, the FAZIA detector is coupled to the INDRA detector [68] at GANIL facility in France. In this chapter, information about the detection module and electronics of the FAZIA detector are presented. The different particle identification methods are discussed. The details of the FAZIA-PRE experiment are also presented in later sections.

2.1 FAZIA detector

The smallest detection element of FAZIA, called a telescope, is made up of two silicon layers followed by a thallium activated cesium-iodide scintillator (Si-Si-CsI(Tl)) with a

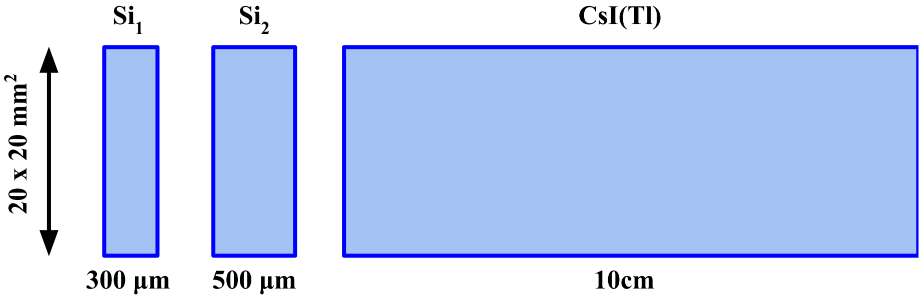

Fig. 2.1: Schematic representation of the Si(300 μm)-Si(500 μm)-CsI(Tl)(10 cm) FAZIA Telescope. Smallest detection element of the detector array. Taken from [69].

total active area of 20x20 mm^2. Fig. 2.1 gives a schematic representation of a FAZIA detector telescope. The first silicon layer (Si$_1$) has a thickness of 300 μm. The second silicon layer (Si$_2$) is generally 500 μm thick. The CsI(Tl) scintillator, with read-out realised by a photo-diode coupled optically to the rear wall of the crystal, has a length of 10 cm.

These single Si-Si-CsI telescopes are then placed in a 2x2 quartet matrices. Then a set of 4 quartets is put in a 2x2 matrix which makes up a total of 16 telescopes in a 4x4 matrix arrangement. This arrangement of 16 telescopes constitutes the basic detection module of the FAZIA detector and is called a FAZIA block (Fig. 2.2). A FAZIA block has an angular acceptance of 0.01 sr of solid angle at about 1 m distance from the target. The signal processing is done behind the telescopes in the frond-end-electronic (FEE) cards.

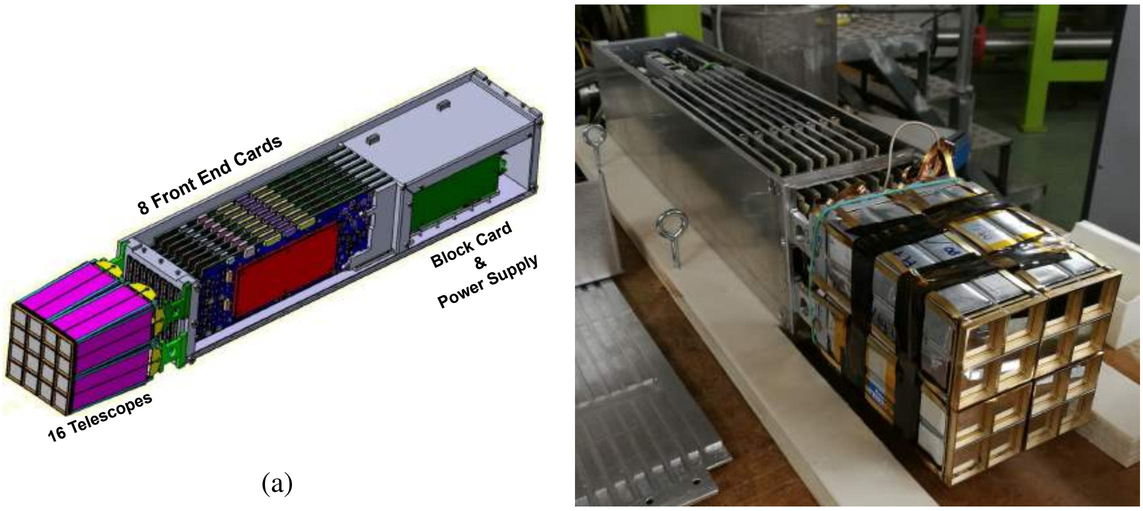

(a)

(b)

Fig. 2.2: (a): The 3-D view of a single FAZIA block with 16 telescopes connected to 8 F.E.E. cards with the block card and power supply card that can be connected to the regional board and data acquisition systems. Taken from [70]. (b): Actual image of a FAZIA block taken in April 2019. The top of the aluminium shielding is opened to make the FEE and block cards visible.

Each FEE card is connected to 2 telescopes. So, there are total 8 FEE cards. A copper plate is placed inside each block for cooling support. The FEE cards are the core component of the FAZIA block that take care of multiple stages for the signal processing. The FEE cards contain six Charge Sensitive Preamplifiers (CSP) each, three per telescope, connected with the three layers of the telescopes. There are three channels for the Si_1 layer: a high range charge channel (QH1), low range charge channel (QL1) and a current channel (I1) ; two channels for Si_2 layer: high range charge (Q2) and current (I2) channels ; single charge channel (Q3) for CsI which is then treated with trapezoidal shaping filter to extract fast and slow signal for PSA. At the end of the block, there is a block card for event building and communication and a power supply card. These cards have high noise so they are screened by a metallic enclosure. The block has very few ports, one for power supply (48V) 2 ports for optical fibre for signals and data acquisition and 2 tubes connecting to the cooling system.

The portability and modularity of the apparatus is one of the most important required features leading to a compact size of the block. A detailed explanation of the FAZIA electronics is given in [70, 71].

2.2 Particle identification

Identification of the charge (Z) and mass (A) of the detected charged particles and improvement of the identification methods has always been the basic aim of FAZIA. Pulse shape analysis (PSA) and $\Delta E-E$ techniques are the two main identification methods used in FAZIA [72, 73]. Successful results due to improvements in these techniques have led the FAZIA detector to identify the particle charges up to $Z\approx55$ and isotopic resolution till $Z\approx20$. The so called "FAZIA recipe" (see [65]) also plays a big role in the identification quality improvement. It basically discusses the main factors studied during the R&D phase that would affect the identification quality in Si detectors. The FAZIA recipe gave the following features:

1. Usage of nTD (neutron Transmutation Doped) silicon layers with uniform doping homogeneity ($< 3\%$) for better PSA.

2. Si layers are cut at 7° with respect to the major crystallographic axis to provide a random distribution of nodes in the active region to avoid the effects of channelling.

3. Reverse mounting of Si detectors gives better PSA identifications.

4. Si detector having uniformity of thickness ($\sim 1\mu m$) gives better $\Delta E-E$ correlation.

5. 30 nm Al layer put on both sides of detectors to reduce sheet resistance.

6. The electric field is kept constant inside the detectors by careful online monitoring of the reverse current.

7. The pre-amplifiers are kept close to the detector telescopes inside the vacuum chamber to avoid any noise or disturbance from long cables.

Along with these factors, the issue of radiation damage in the detectors has also been addressed. For CsI crystals, to increase scintillation efficiency for heavy ions, a Tl concentration is around ~2000 ppm and the response, resolution and homogeneity along the detector length were improved by wrapping the crystals with a highly reflective material (3M Vikuity^{TM} ESR) [74]. The fast digital electronics and excellent algorithms for signal shaping developed within the collaboration have given successful results for particle identifications in multiple FAZIA tests and experiments.

At this point, it is important to discuss the ΔE−E and PSA identification techniques in detail. The implementation of these techniques depends on the path of the incident particle. As shown in the Fig. 2.3, there can be 3 possible paths: (1) the particle can enter and release all of its energy and stop in Si_1 ; (2) the particle can enter and release fractional energy in Si_1, punch through it and then deposit the remaining energy in Si_2 and stop there ; (3) the particle punches through both Si_1 and Si_2 depositing some fractions of its energy and releasing the remainder in CsI to stop there. Depending on these 3 paths, there can be 2 ways of ΔE−E (Si_1-Si_2 ; (Si_1+Si_2)-CsI) and 2 ways of PSA (Si PSA ; CsI PSA) identification methods.

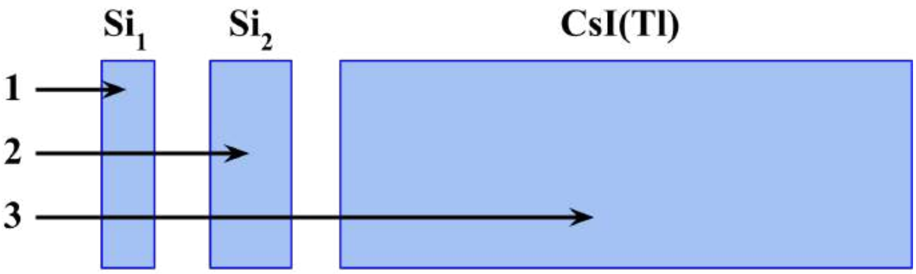

Fig. 2.3: Schematic representation of different possible scenarios for a particle entering inside the FAZIA telescope. Trajectories of particles stopping in 1: Si_1 ; 2: Si_2 ; 3: CsI.

2.2.1 ΔE-E method

The ΔE-E identification technique is a very commonly used method for particle identification. The principle of this technique is based basically on the concept of "stopping power". The stopping power of any detector material is equal to the energy loss of the incident particle per unit path length inside the detector, $-dE/dx$, also known as "specific energy loss". The Bethe-Bloch formula for this specific energy loss in the detector material is written as,

$$-\frac{dE}{dx} = \frac{4\pi e^4 Z^2}{m_0 v^2} Nz \left[ln\frac{2m_0 v^2}{I} - ln(1 - \frac{v^2}{c^2}) - \frac{v^2}{c^2} \right] \tag{2.1}$$

where, Z and v are the atomic number and velocity of the incoming particle, m_0 and e are electron rest mass and electronic charge and N is the number of nuclei per unit volume of the detector material. z and I are the atomic number and ionisation potential of the of detector material, respectively, and are constant for a given material.

In the non-relativistic regime ($v << c$), The term inside square brackets is generally constant due to weak dependence on v. Ultimately, the particle energy loss has the following dependence,

$$-\frac{dE}{dx} \propto \frac{Z^2}{v^2} \propto \frac{Z^2 A}{E} \tag{2.2}$$

where, A and E are atomic mass and total kinetic energy of the incident particle. For FAZIA, the first detector (Si_1) with small thickness "t", the energy deposited by a particle passing through is,

$$\Delta E = -\frac{dE}{dx} t \tag{2.3}$$

or,

$$\Delta E = C\frac{Z^2 A}{E} t \tag{2.4}$$

The residual energy (E_r) of the particle deposited in the second detector (Si_2) will be,

$$E_r = E - \Delta E \tag{2.5}$$

or,

$$E_r = C\frac{Z^2 A}{\Delta E} t - \Delta E \tag{2.6}$$

The above equation shows that every particle with a specific Z and A will have its own path of energy loss for the ΔE−E plane. This is used in FAZIA for the particles following the trajectories 2 and 3 from Fig. 2.3. For the particles passing through Si_1 and stopping in Si_2, the ΔE-E correlation is used for energy loss in Si_1 vs energy loss in Si_2 (shown in Fig. 2.4 for ^{48}Ca+^{27}Al at 25 MeV/A). For the particles passing through Si_1 and Si_2 and then stopping in CsI, the ΔE-E correlation is used for combined energy loss in Si_1 and Si_2 vs the light output of CsI (Fig. 2.5). Here, the ^{48}Ca+^{27}Al system is shown at 40 MeV/A because at 25 MeV/A, most of the heavier fragments tend to stop in Si_2. So the Si-CsI correlation does not show large range of fragments. But at 40 MeV/A, the energy is high enough that these fragments pass through Si_2 and reach CsI.

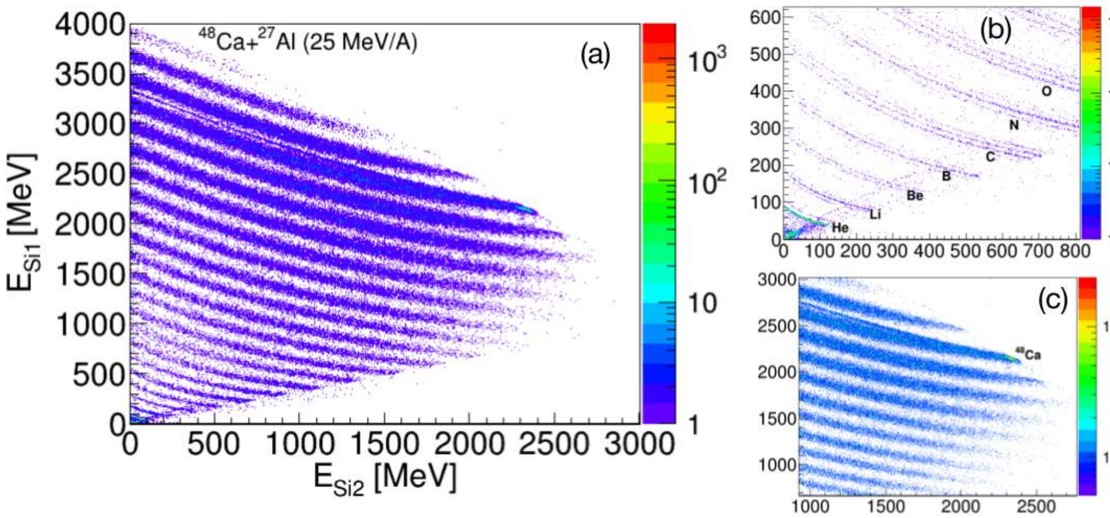

Fig. 2.4: (a): Si$_1$-Si$_2$ ΔE−E matrix for ^{48}Ca+^{27}Al (25 MeV/A). Insets show expansion around (b): lighter fragments and (c): projectile.

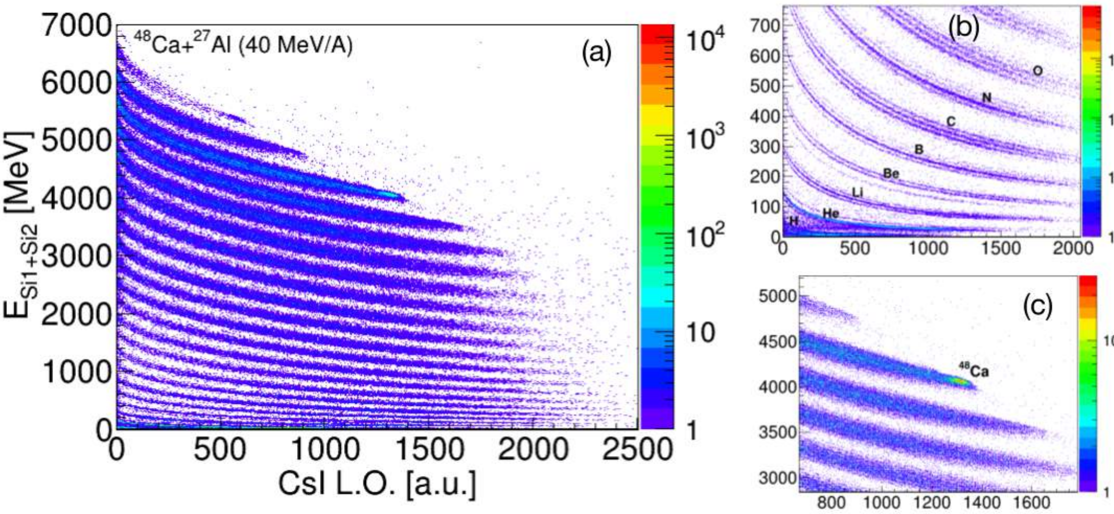

Fig. 2.5: (a): (Si$_1$+Si$_2$)-CsI ΔE−E matrix for ^{48}Ca+^{27}Al (40 MeV/A). Insets show expansion around (b): lighter fragments and (c): projectile.

2.2.2 Pulse shape analysis (PSA)

The pulse shape analysis (PSA) technique has been used since long time to investigate the signals produced in detectors by charged particles and radiation. With advancement of the electronics and digitisation of pulses, PSA is now used at a very large scale. In the FAZIA detection systems, PSA can be used to identify particles from a single detector from the output pulse. PSA is used in two cases, for the particles following the paths (1) and (3) in Fig. 2.3. So, if a particle is stopped in Si$_1$, there is no information for Si$_2$, so ΔE−E method cannot be used. Also, when the particle punches through Si$_1$ and Si$_2$ and stops in CsI, the ΔE−E method for (Si_1+Si_2) and CsI correlation makes it a little difficult to identify the light-charged particles. Then the CsI fast-slow PSA is used which gives isotopic identification for $Z \leq 5$.

Silicon PSA

The PSA technique in Si detectors has been used previously for particle identification in detectors like CHIMERA [75] and KRATTA [76]. But FAZIA has properly used and improved this technique for a wider range of particle identification [72]. The rise-time of the signal from charge deposition ($Q_{risetime}$) and the maximum value of the current (I_{max}) are its two common shape dependent parameters. As each particle with different A, Z and E has separate pulse (see Eq. 2.2) leading to different charge collection times, the study of signal evolution in Si in terms of $Q_{risetime}$ and I_{max} can help to identify the corresponding incident particle. The Fig. 2.6 (taken from [77]) shows different pulses for different fragments detected in the Si_1 layer of FAZIA detector. The $Q_{risetime}$ increases and the I_{max} decreases with increasing Z, respectively. Both these parameters have been extensively studied during the FAZIA R&D phase. The studies have shown the lowering of identification thresholds using both the parameters, but I_{max} gives a better correlation with the energy deposited in the Si. Here, a “better correlation” means that the separation of isotopic ridges is relatively better with I_{max}. Fig. 2.7(a) shows the deposited energy and I_{max} correlation matrix for Si_1 layer. Most of the particles punch through the layer. Only low energy fragments can stop in this layer due to its low thickness. An inset shows some light fragments. The Fig. 2.7(b) shows the deposited energy and I_{max} correlation matrix for Si_2 layer. It can be seen that fragments that stop completely inside the Si_2 layer form a thick ridge on the left side of the matrix. The inset show zoom on the projectile (^{48}Ca).

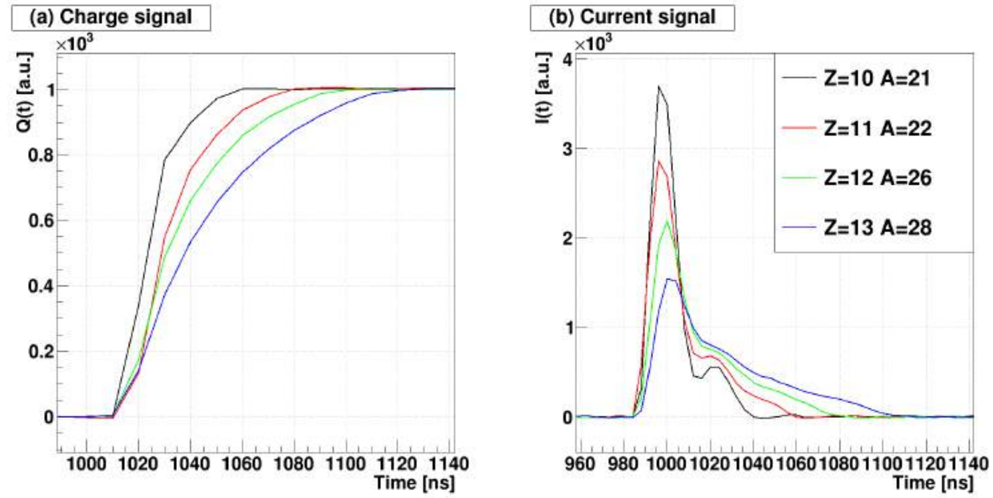

Fig. 2.6: (a): Charge (Q) and (b): Current (I) signals produced by same Si_1 detector by 4 different fragments for the same deposited energy (1000 a.u.): ^{21}Ne, ^{22}Na, ^{26}Mg and ^{28}Al. Taken from [77].

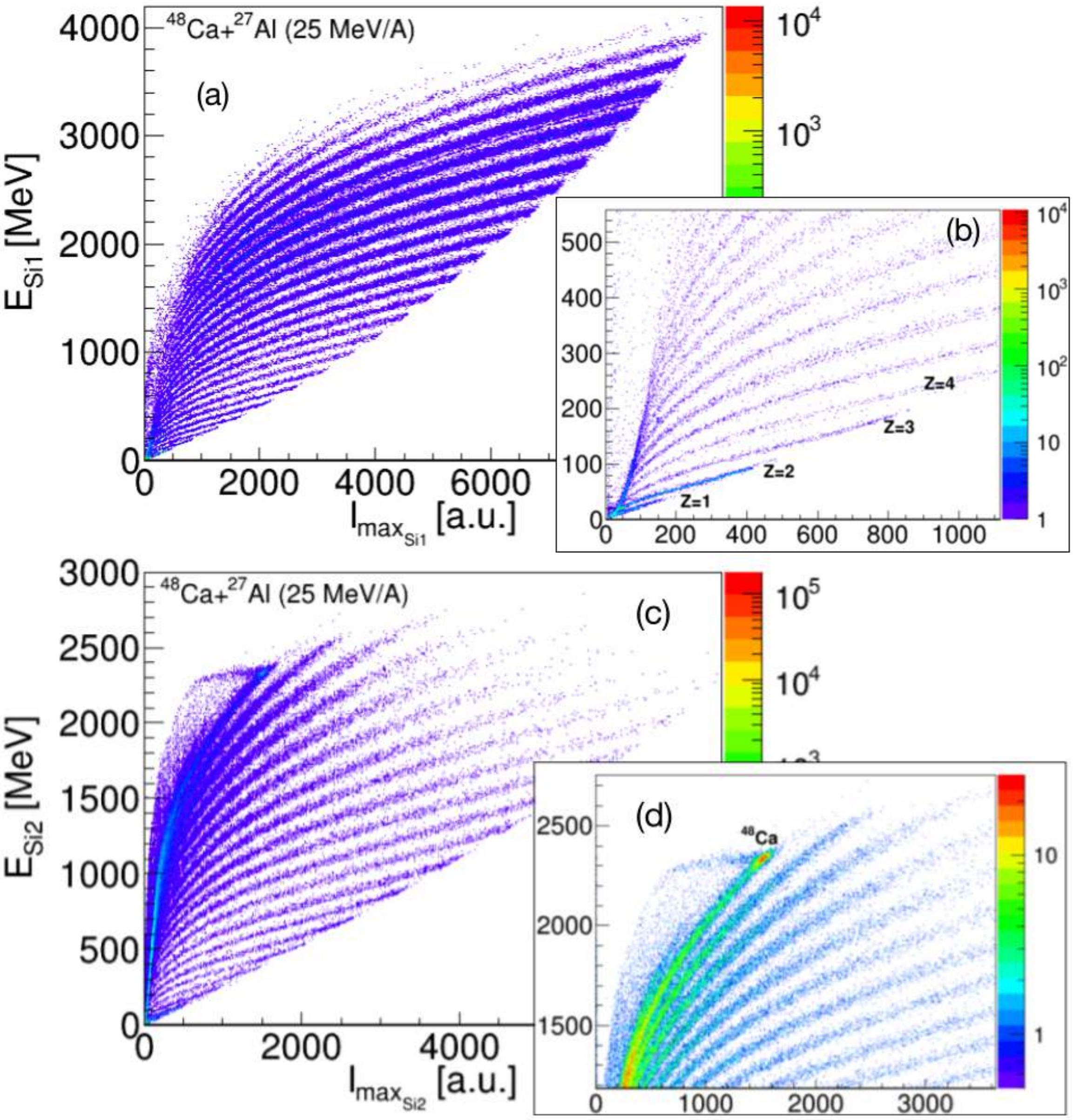

Fig. 2.7: Energy vs I$_{max}$ correlation PSA matrix from (a): Si$_1$ layer and (c): Si$_2$ layer, for ^{48}Ca+^{27}Al (25 MeV/A). The insets show expansion around (b): lighter fragments and (d): projectile.

CsI fast-slow PSA

The particles that follow the path (3) in Fig. 2.3, have usually very high energies. So, they pass through both the Si detectors and as a result, the energy loss in both Si is relatively small. If the signal from Si$_2$ becomes small due to lower energy loss, it can mix within the electronic noise and the isotopic separation can be lost in ΔE−E matrices. This usually happens with the lighter fragments. But when these light fragments reach CsI, their pulses are well separated isotopically.

The scintillation light pulse decay at time t is written, according to [78], in terms of fast and slow components as,

$$L(t) = L_f e^{t/\tau_f} + L_s e^{t/\tau_s} \tag{2.7}$$

where, L_f and L_s are amplitudes of the fast and slow light output and τ_f (~ 0.4−0.7 μs) and τ_s (~ 7 μs) are time constants for fast and slow components, respectively. The value of τ_s is constant for a detector material irrespective of the incoming particle, whereas, $1/\tau_f$ increases with dE/dx. Thus, the fast component depends on the Z, A and E of the incoming particle. This produces separate loci for each isotope in CsI fast-slow correlation matrices (see Fig. 2.8). As stated in [79], the value of τ_f and fast-slow amplitude ratio saturates for $Z \geq 4$. So, the ridges for fragments with $Z \gtrsim 5$ merge together (thick single line at the upper side in Fig. 2.8). For FAZIA, the CsI fast-slow matrices have good separation of isotopes till Z~5 and are used for particle identification by PSA.

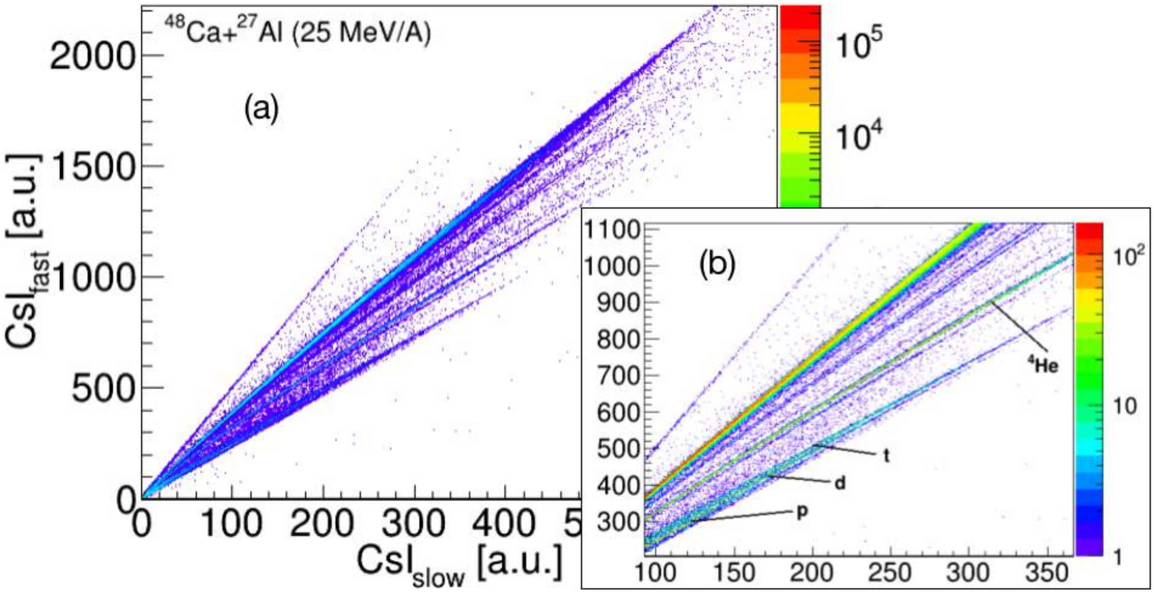

Fig. 2.8: (a): CsI fast-slow PSA matrix for ^{48}Ca+^{27}Al (40 MeV/A) ; (b): Inset shows separate isotopes of LCPs reaching the CsI.

2.3 Identification procedure

The particle identification procedure for all the different correlation matrices shown in the preceding section is more or less similar. To explain this, the data from the FAZIA-PRE experiment are used. The particle identification from Si PSA, Si$_1$-Si$_2$ ΔE−E and Si-CsI ΔE−E and the detector calibrations were done by P. Ottanelli. The procedure for detector calibration and ΔE−E identification is explained in detail in his Ph.D. thesis [77]. I did the particle identification from the CsI PSA and it is discussed below.

Signal Processing

The total charge signal from CsI (Q3) is digitized in the ADC. Two trapezoidal shapers with different time characteristics corresponding to fast and slow signals are applied in parallel to the pre-amplifier output. The slow shaper gives the total amplitude of the signal ($Q3_{max}$) and the fast shaper gives the fast component of the scintillation light ($Q3_{fast}$). To get the fast-slow correlation matrix, the fast and slow signals are separately required. To get the slow signal, the fast signal can be subtracted from the total signal output: $Q3_{slow} = Q3_{max} - (0.8^{*}Q3_{fast})$.

For the FAZIA-PRE data, the CsI fast-slow PSA method requires the matrices to have well separated ridges for different isotopes from Z=1 to Z=5. It was noticed that during the experiment, the performance of CsI was significantly lower than that from the previous experiments. In addition, the average quality of fast-slow matrices was much lower than before. It was suspected that the reduction of the pre-trigger length was not correctly taken into account while calculating the baseline level. In fact, the baseline was calculated on 100 samples (1 μs) which was very close to the pre-trigger length. Changing this value to 70 samples (700 ns) did not solve the situation at all (see Fig. 2.9*), ruling out a baseline estimation problem.

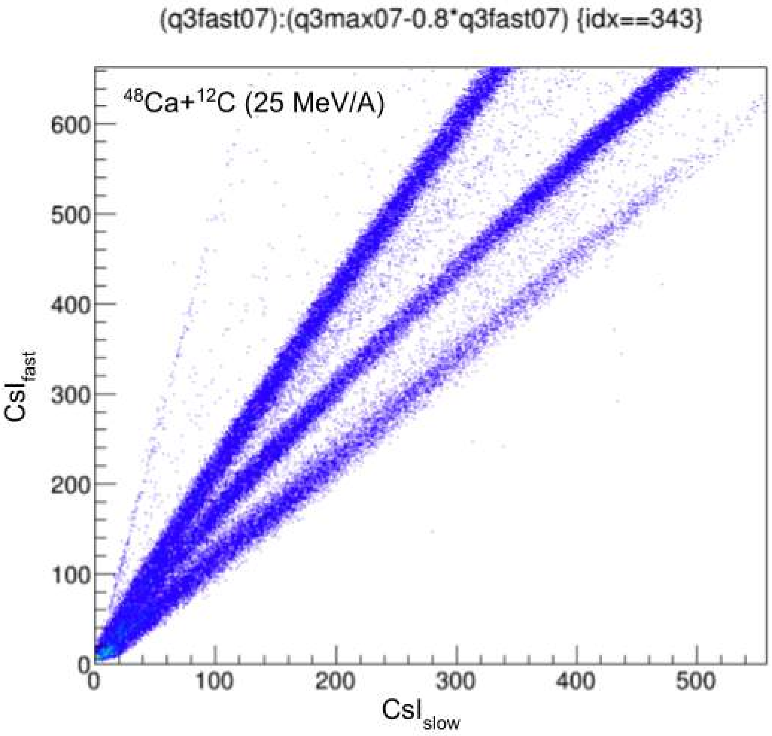

Fig. 2.9: CsI fast-slow matrix computing the baseline level on 70 samples for idx* = 343.

---

*The "idx" is an ID number assigned to a FAZIA telescope. It follows a simple relation: idx = B*100+Q*10+T*1. B, Q and T stands for the number of the block, quartet and telescope, respectively. For FAZIA-PRE experiment, see Fig. 2.17(b).*

To understand this behaviour, CsI signals from the pulser (Fig. 2.10(a)) were observed. A new noise component (~1 kHz) could be clearly seen. This noise was not cut by the trapezoidal filter using the standard shaper rise time (0.7 μs). The only solution was to eliminate this noise component by significantly increasing the rise time to 3 μs, leaving the flat top at 0.5 μs for the fast component and 10 μs for the total signal (Fig. 2.10(b)).

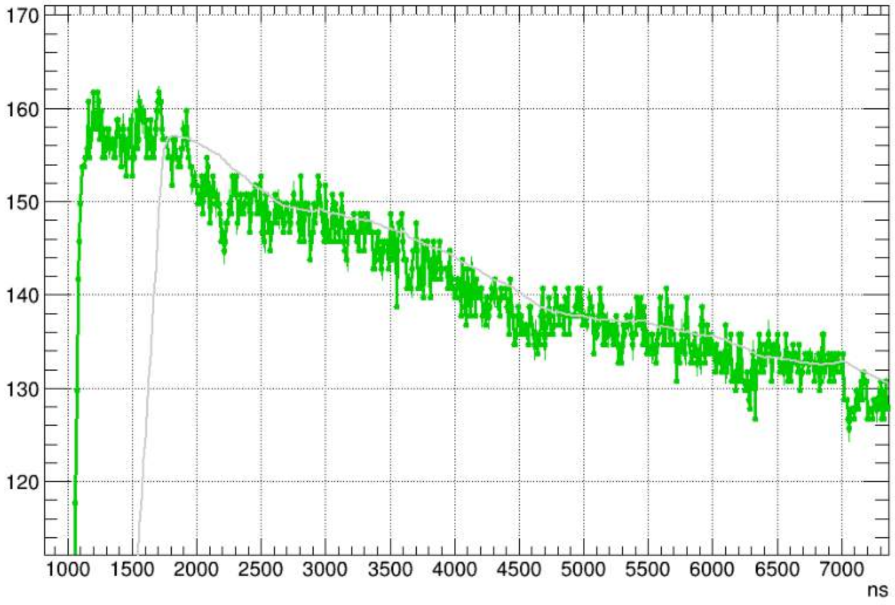

(a)

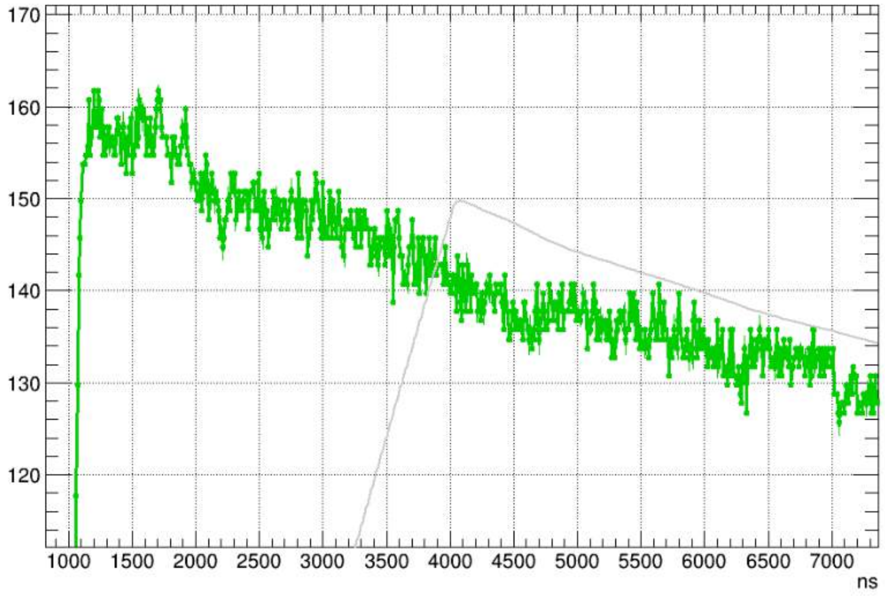

(b)

Fig. 2.10: CsI pulser signal (green) for idx = 32. The gray line is the filtered signal. (a): 0.7 μs risetime. (b): 3.0 μs risetime.

The price to pay is a small deficit in the maximum estimation due to the lack of pole zero compensation. This new set of parameters was then applied to pulser data and a significant reduction of the first pulser peak standard deviation was seen while increasing the trapezoidal shaper risetime from 0.7μs to 3μs. The effect on fast-slow matrices can be seen in Fig. 2.11. Increasing the shaper risetime to 3 μs filtered the ~1kHz noise contribution and fast-slow matrices got better. The p, d, t discrimination was also recovered in most cases. The quality of already good matrices was also increased slightly. The global shape of the matrix was also affected as the maximum value was slightly reduced due to the lack of pole zero compensation. On the other hand, the fast component increased. With these improved matrices, the particles were properly identified.

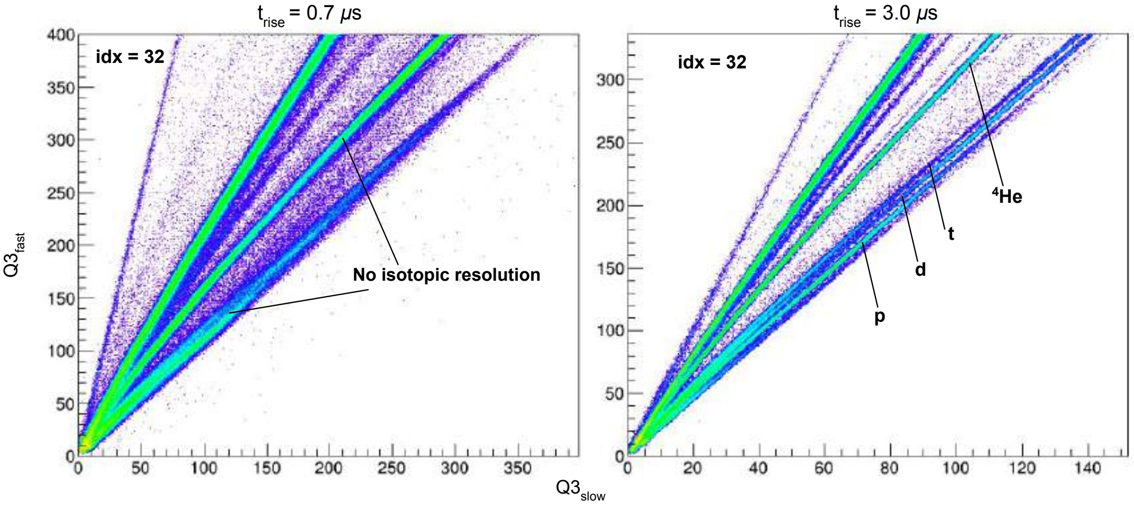

Fig. 2.11: CsI fast-slow matrices with 0.7 μs (left) and 3.0 μs (right) risetime (idx = 32).

KaliVeda Toolkit

All the data handling and reconstruction is done using the KaliVeda toolkit [80] developed by the INDRA collaboration [81] which is now updated to be compatible with the FAZIA frameworks. It is an object oriented data analysis toolkit based on frameworks of ROOT [82]. It was originally developed for simulating and calculating nuclear properties and reaction kinematics and data analysis for the INDRA and FAZIA charged particle detector arrays, but now it provides many tools of general interest like treatment of large data sets from multi-particle events. The energy loss and range calculations can also be done in KaliVeda which helps for particle data reconstruction. It can load arbitrary multi-detector geometries. It can be used for particle identification by PSA and ΔE−E techniques. The data analysis and particle identification presented here was also done within the KaliVeda frameworks. There is also an interface to the GEMINI++ statistical decay code which was also used for data analysis and will be discussed in further chapters.

Grid clicking and particle identification spectra

The first step after obtaining the identification matrices is the placement of the grids on specific isotopic ridges. Separate grid lines (black lines) are manually placed on each isotope and the Z and A is assigned to each line with the help of grid manager in KaliVeda. Fig. 2.12 shows the grids placed on a CsI fast-slow matrix. An inset with zoom in on grid lines is also shown. Multiple functions are present around the canvas pads to control and edit the grids. There are two cuts (red lines) put in the whole grid. Cut on the lower end is put to exclude all the contribution of the electromagnetic radiation. The cut on the upper edge is to exclude the region where the contribution of all the fragments for Z>5 merges into a single ridge. After the grid placement, a simple inbuilt linearization process assigns a particle identification number (PID) to each grid line corresponding to its Z and A value. This provides a correlation between the PID and the CsI light output (L.O.) as shown in Fig. 2.13. From this linearised correlation, it is possible to create a 1-dimensional PID spectra as shown in Fig. 2.14. PID assigned to each grid line generates a group of peaks around a specific Z value with respect to (w.r.t.) the corresponding A values that helps to identify the isotopes of a specific element. This PID spectra further generates a Z vs N nuclear chart using the KVNuclearChart class of KaliVeda that shows the isotopes identified in the whole identification procedure (Fig. 2.15).

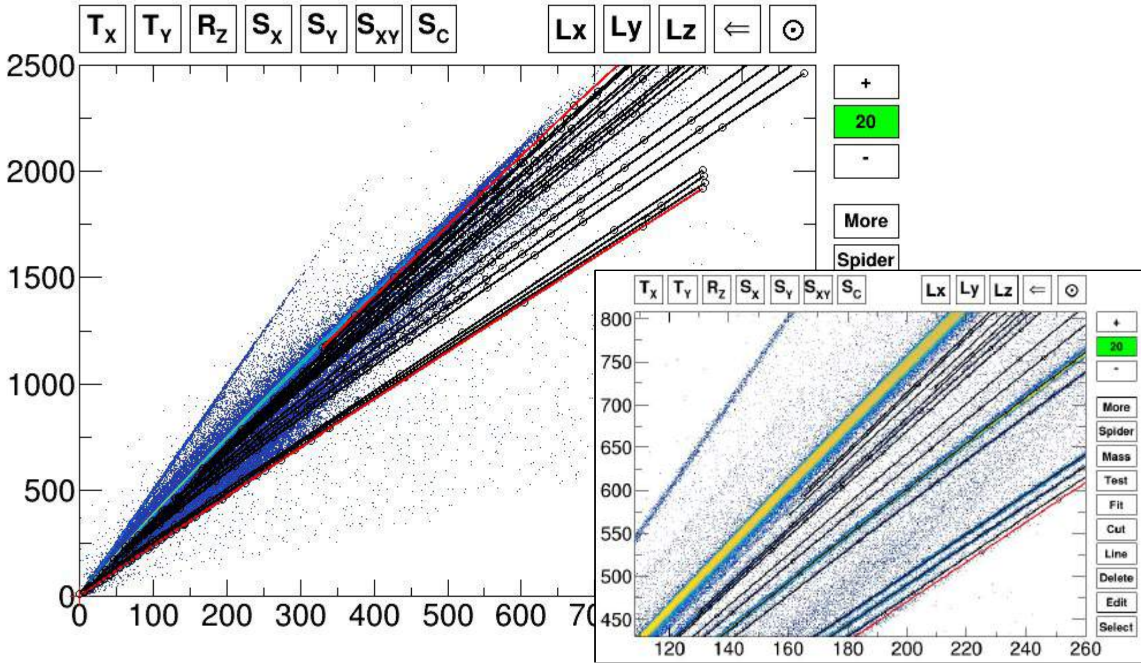

Fig. 2.12: Grid placement on ridges in CsI fast-slow matrices for PSA. Black lines are the lines for particle identification. Red lines are the graphical cuts in the data to exclude contributions of electromagnetic radiation and non-separated IMF ridges (Z>5). Different functions around the canvas pad are used to control and edit the grids.

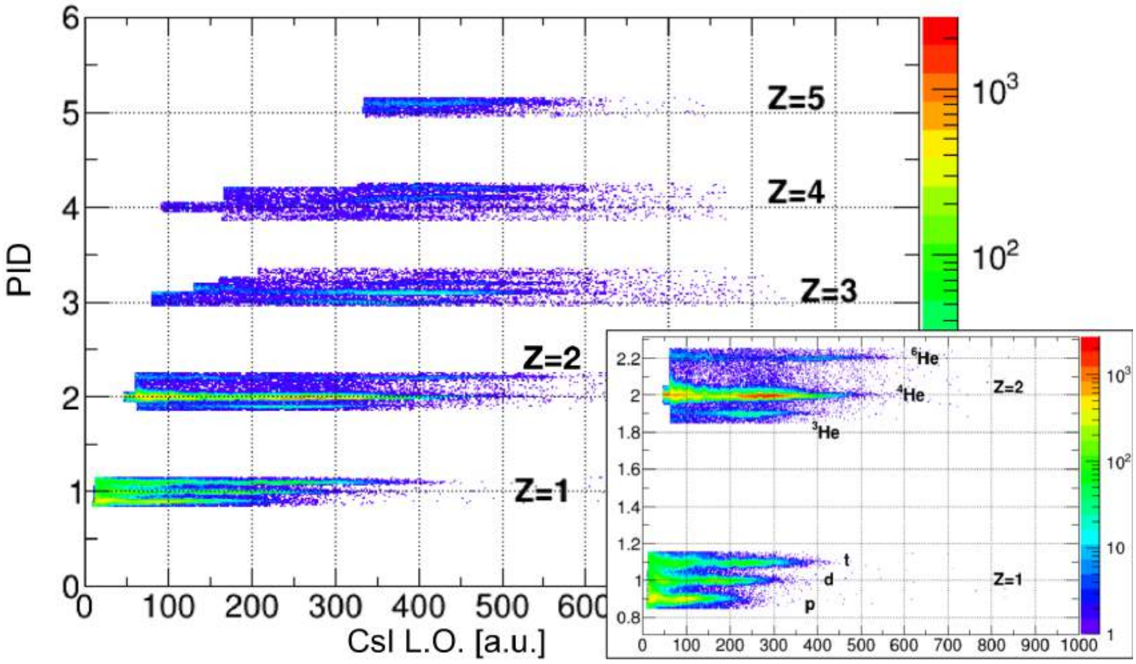

Fig. 2.13: PID vs CsI L.O. correlation after linearization algorithm applied on grids in CsI fast-slow matrices.

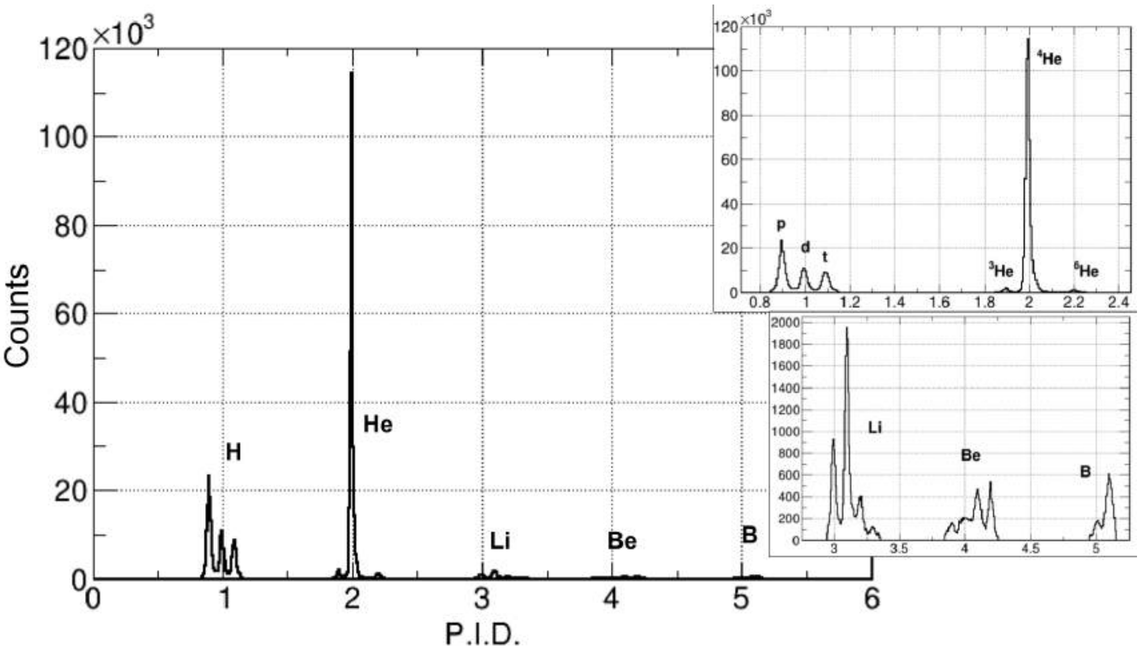

Fig. 2.14: 1-dimensional PID spectra generated from Fig. 2.13 showing the isotopes identified in CsI fast-slow PSA method.

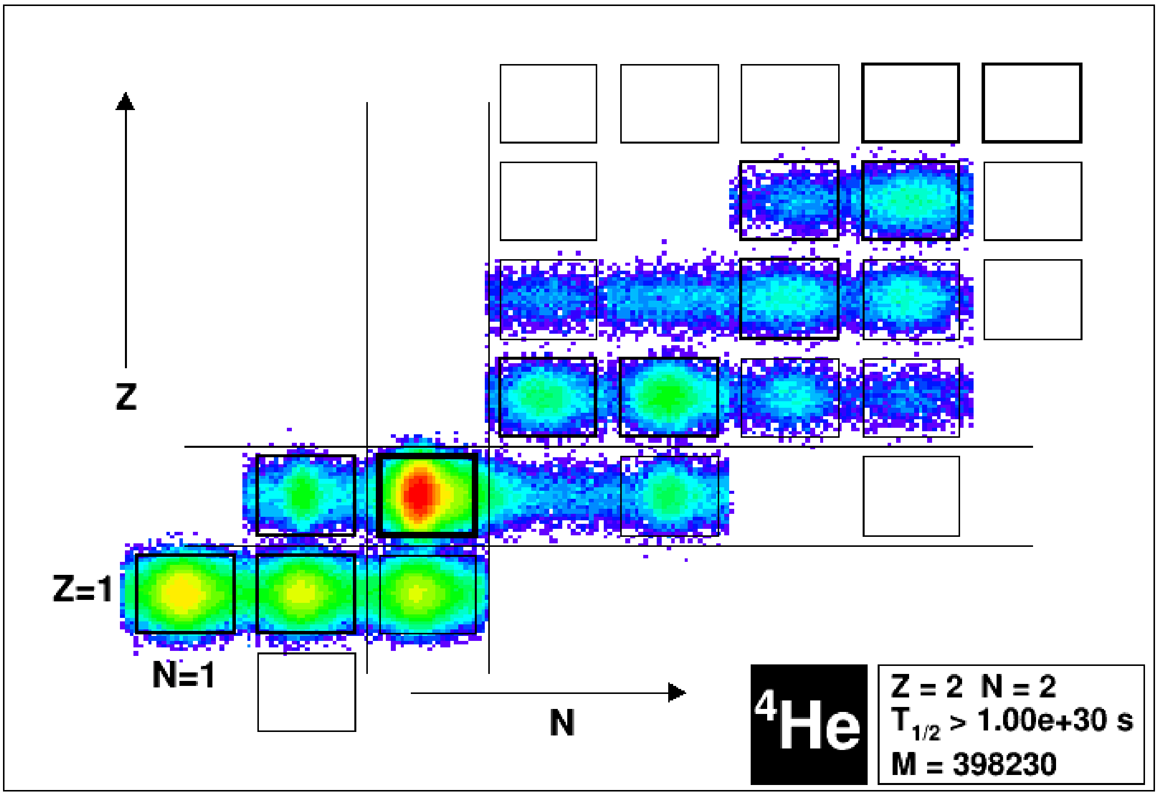

Fig. 2.15: Z vs N nuclear chart for isotopes detected in CsI fast-slow PSA. In KaliVeda graphical user interface (GUI), double clicking on a specific isotope on the nuclear chart gives the information about its half-life ($T_{1/2}$) and the total number of particles of that isotope (M)

2.4 The FAZIA-PRE experiment

The isospin transport phenomena have been studied using the FAZIA detector since a few years now [83–86]. The excellent isotopic resolution of the detector discussed in the previous sections has been the most important property that has made it eligible for studying such physical phenomena. The N/Z being an isospin sensitive observable has been one of the main observables of interest during recent FAZIA experiments. The studies have been done using both symmetric and asymmetric projectile and target systems interacting at the Fermi energy range in order to compare the flow of isospin (N/Z) within the system by analysing the detected fragments.

The FAZIA-PRE experiment was based on a similar approach of using a neutron rich beam to excite the isospin degree-of-freedom of the symmetry energy term (E_{sym}) of the nuclear equation of state (EoS). The initial neutron abundance can be helpful to study different observables like the fission probability [87, 88], the width of fragment isotopic distributions [89] and odd-even yield staggering [90, 91]. However, the initial conditions of neutron richness can be diminished due to pre-equilibrium (fast) neutron emission. Fast emissions have been clearly reported for neutrons and light particles within the Fermi energy range [92]. It can be seen in Fig. 2.16 that the pre-equilibrium (PE) neutron multiplicity (M_n) keeps on increasing with increasing beam energy. The fast emissions can be dominated by neutrons if the N/Z of the system increases, i.e., a neutron rich entrance channel. Although, the fragment properties can depend on the N/Z of the participants in the Fermi energy range, it has not been systematically addressed so far with specific measurements. So, to observe the effects on the fragment features due to high initial N/Z of the system with increasing energy was one of the main aims of the experiment.

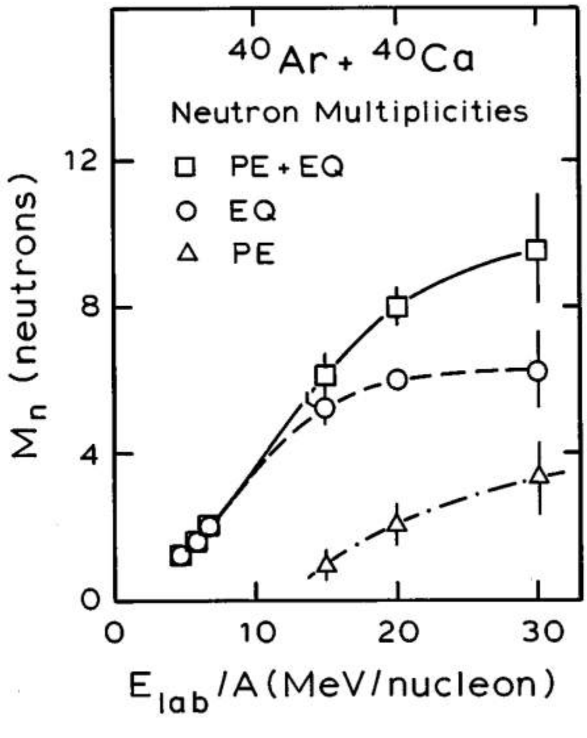

Fig. 2.16: Neutron multiplicities (M_n) as a function of beam energy. PE and EQ denote the pre-equilibrium and equilibrium components, respectively. Taken from [92].

The experiment took place at the Laboratori Nazionali del Sud (LNS), Catania, Italy in February 2018. It was performed using 4 blocks in a wall structure and two more blocks, one on each side of the wall (Fig. 2.17(a)), i.e., a total of 6 blocks of FAZIA, placed at a 100 cm distance from the target inside the LNS-Ciclope chamber. So, a total of 96 (6x16) Si (300 μm) – Si (300/500 μm) – CsI (10 cm) telescopes were used. Due to limited availability of 500 μm Si_2 layers for a moment, 300 μm Si_2 layers were used in some of the telescopes.

The overall angular coverage of the detector setup was from θ ~2-8° and ~12-18° as shown in Fig. 2.17(b). It also shows how the id of each telescope (*idx*) was assigned in this experiment. To avoid irradiation of telescopes closest to the beam axis with elastic scattering of the beam, shielding disks were used.

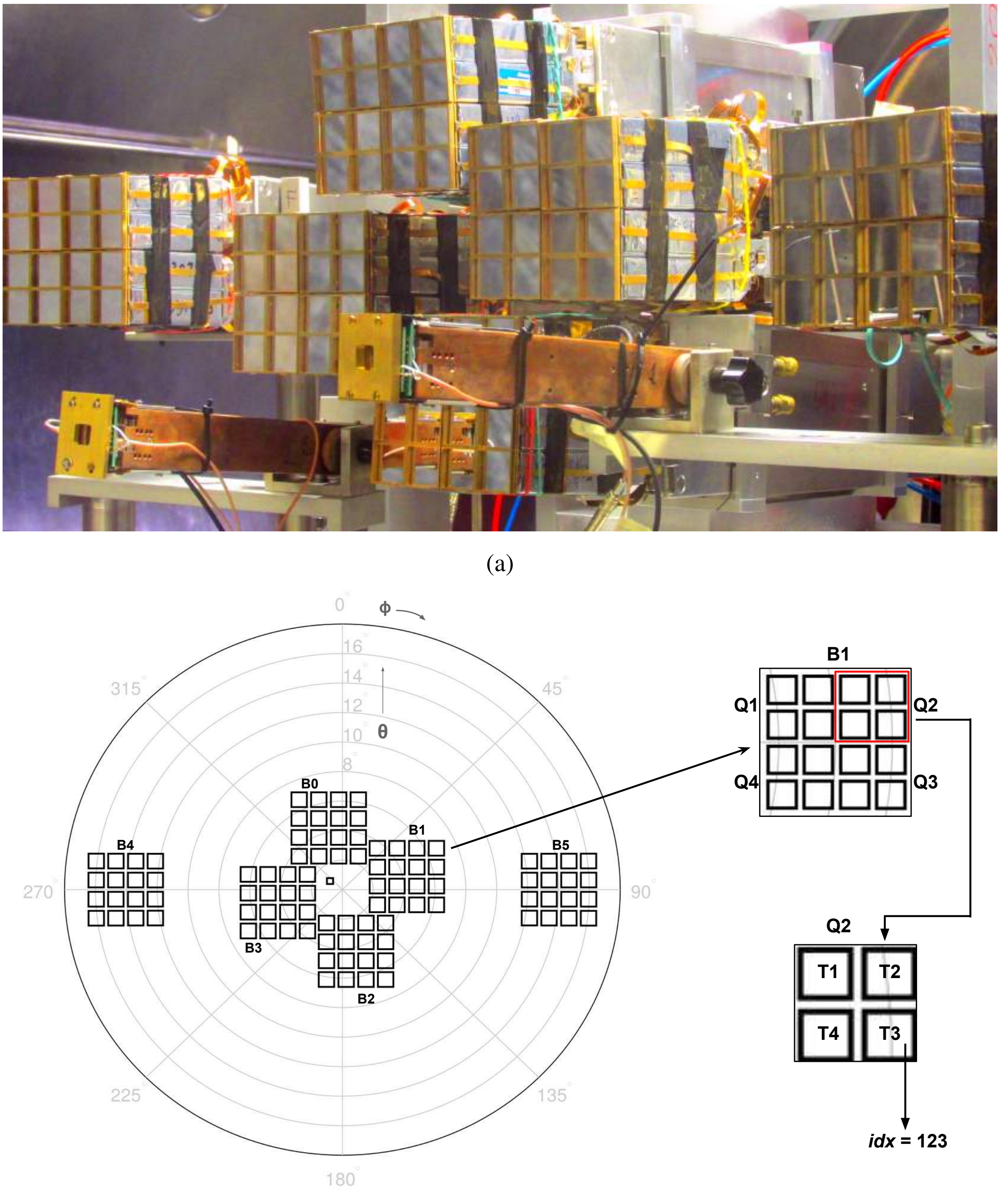

(a)

(b)

Fig. 2.17: (a): Photograph of the actual experimental setup at LNS, Catania (taken from [77]). (b): Angular coverage of the FAZIA-PRE experimental setup. The four blocks in wall structure cover ~2-8° of θ. The remaining 2 blocks on the sides have a coverage of ~12-18° of θ. Direction of ϕ is also marked. Assignment of telescope ID (idx) according to the block, quartet and telescope numbers (B*100+Q*10+T*1) is also shown.

In this experiment, ^{40,48}Ca beams at 25 and 40 MeV/A were used on ^{12}C, ^{27}Al and ^{40}Ca targets. A study of isospin evolution with N/Z symmetric (^{40}Ca+^{12}C) and N/Z asymmetric (^{48}Ca+^{12}C) systems at 25 and 40 MeV/A has been done by P. Ottanelli in his doctoral thesis work [77]. However, in this doctoral research work, the data concerning ^{48}Ca projectile impinging at energy 25 MeV/A on ^{12}C, ^{27}Al and ^{40}Ca targets, and at energy 40 MeV/A on ^{12}C and ^{27}Al targets has been analysed. The motive for this choice is to study the evolution of isospin transport properties in reaction products both as a function of beam energy and target mass of the system together. The N/Z values of each participating nuclei and corresponding reaction systems is given in Table 2.1. The ^{48}Ca projectile is a neutron rich nucleus with N/Z = 1.4. The targets ^{12}C and ^{40}Ca are symmetric with N/Z = 1 and ^{27}Al has one extra neutron making its N/Z = 1.07. The total N/Z of the system, i.e., N/Z of the projectile and target combined ranges from 1.2 to 1.31.

Nucleus	N/Z
^{48}Ca	1.4
^{12}C	1.0
^{27}Al	1.07
^{40}Ca	1.0

System	N/Z total
^{48}Ca+^{12}C	1.31
^{48}Ca+^{27}Al	1.27
^{48}Ca+^{40}Ca	1.2

Table 2.1: N/Z values for participant nuclei (left) and reaction systems (right) from FAZIA-PRE experiment

Other experimental details like beam velocities (v_B), target thickness (t), centre-of-mass velocities (v_{CM}), available energy in centre-of-mass (E^{av}_{CM}) and grazing angles in laboratory frame (θ_{gr}) of the concerned systems are given in the Table 2.2.

Projectile	$^{48}_{20}$Ca				
E_B [MeV/A]	25			40	
v_B [cm/ns]	6.81			8.51	
Target	$^{12}_{6}$C	$^{27}_{13}$Al	$^{40}_{20}$Ca	$^{12}_{6}$C	$^{27}_{13}$Al
t [μg/cm^2]	239	216	500	239	216
v_{CM} [cm/ns]	5.48	4.4	3.76	6.87	5.53
E^{av}_{CM} [MeV/A]	3.99	5.74	6.18	6.38	9.17
θ_{gr}	0.89°	1.81°	2.69°	0.55°	1.12°

Table 2.2: FAZIA-PRE experimental details. $^{48}_{20}$Ca projectile on $^{12}_{6}$C, $^{27}_{13}$Al and $^{40}_{20}$Ca targets at 25 and 40 MeV/A beam energies (E_B) along with their corresponding beam velocities (v_B), target thickness (t), centre-of-mass velocities (v_{CM}), available energy in centre-of-mass (E^{av}_{CM}) and grazing angles in laboratory frame (θ_{gr}).

The ^{12}C and ^{27}Al targets have nearly same thickness t. The ^{40}Ca target is about twice as thick as the other targets. Also, as the target becomes heavier, the E$_{CM}^{av}$ decreases. With the target becoming heavier, the size of nucleus also increases leading to increase in θ_{gr}. The effects of increasing or decreasing target mass and beam energy along with the effects of the above reaction observables will be discussed in further chapters.

Chapter 3

Data analysis

The details of the FAZIA-PRE experiment discussed in the previous chapter showed that the detector geometry provided good acceptance at forward angles (~ $2^\circ - 8^\circ$ and $12^\circ - 16^\circ$) as was shown in Fig. 2.17(b). With this constraint, only the quasi-projectile (QP) region of the reaction systems (fragments around Z~20 and A~48 for ^{48}Ca projectile) was expected to be detected along with a few fragments from the neck region and/or pre-equilibrium emissions in the forward direction towards the detector setup. The quasi-target (QT) region cannot be observed because it is spread majorly in the transverse plane (X-Y plane, as Z axis is along the beam), i.e., around $\theta = 90^\circ$ because it is stationary in the laboratory frame. This can be confirmed from Fig. 3.1 showing the fragment charge (Z) and longitudinal velocity ($v_{||}$) correlation for Z>2. For all the five systems under study in this research, the peaks in fragment yield can be observed around Z~20 and $v_{||} = v_B$ (vertical black dotted line), where v_B is the corresponding beam velocity given in Table 2.2. The centre-of-mass velocity (v_{CM}) is also marked for each system by vertical red dotted lines. So, the data acquired from the experiment basically consists of the QP fragments which are supposed to be coming from the neutron rich projectile, ^{48}Ca.

Here, the reaction products can be studied in such a way that the effects of changing the mass of the target (^{12}C, ^{27}Al and ^{40}Ca) and the energy of the beam (25 and 40 MeV/A) can be observed. This change in target mass and beam energy can be further separated for the kind of physics to be observed. For basic reaction dynamics, fragment charge , mass, velocity and total multiplicity of charged particles (Z>1) can be plotted. For more complex phenomena, such as isospin transport, the isospin evolution of fragments can be compared, which is among the objectives of the whole experiment. Hence, in this chapter, the analysis of the FAZIA-PRE experimental data is presented in two sections. The first section deals with the data comparison for basic reaction observables such as mass (A), charge (Z), longitudinal velocity ($v_{||}$) and multiplicity (M_{tot}) of the reaction products. The second section deals with the comparison of the isospin content of the fragments (N/Z). The comparison of the data to study the effects of changing the target mass and beam energy is further discussed inside these two sections of the chapter.

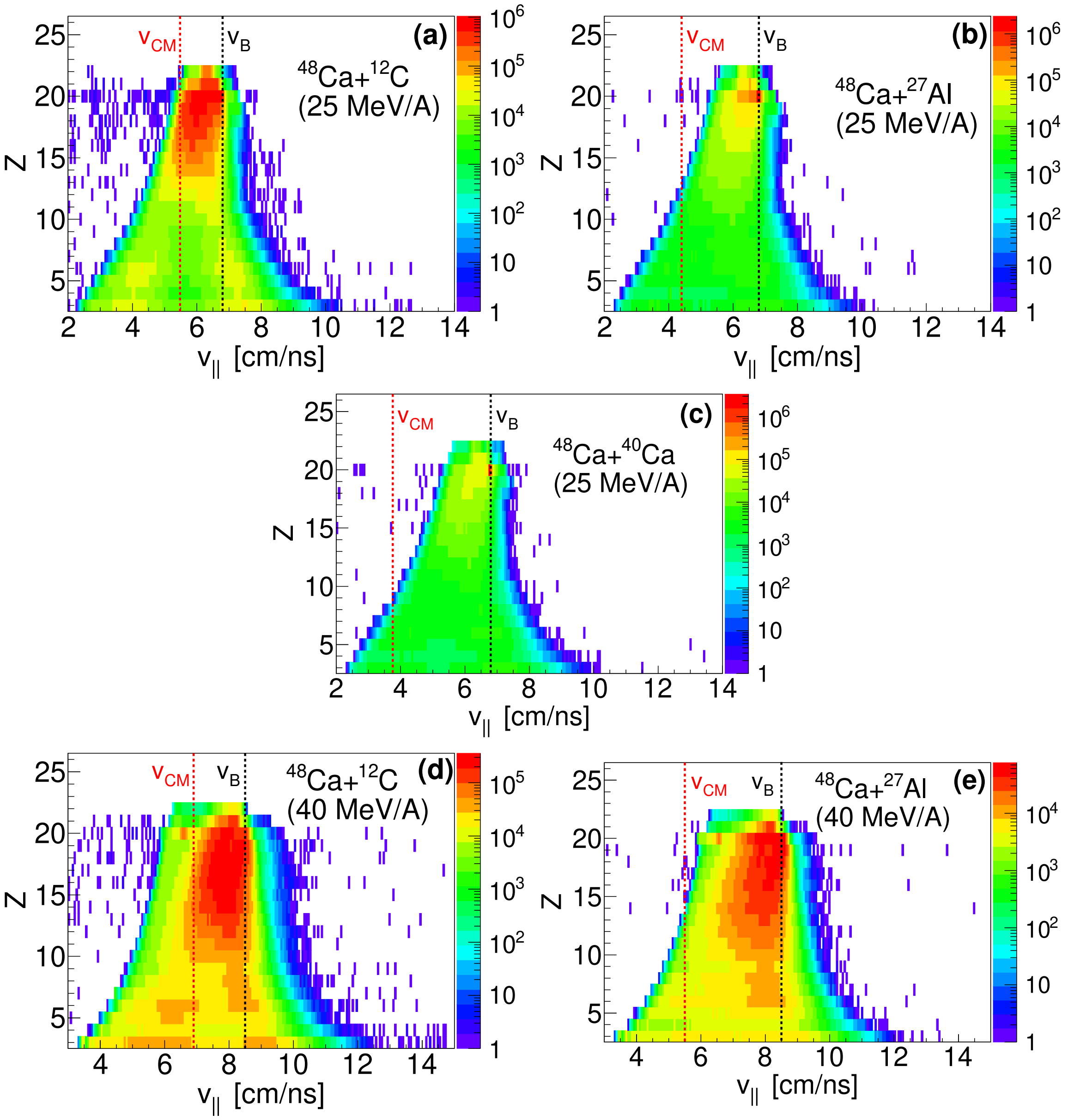

Fig. 3.1: Fragment charge (Z) vs longitudinal velocity ($v_{||}$) for Z>2. (a): ^{48}Ca+^{12}C (25 MeV/A), (b):^{48}Ca+^{27}Al (25 MeV/A), (c): ^{48}Ca+^{40}Ca (25 MeV/A), (d): ^{48}Ca+^{12}C (40 MeV/A) and (e): ^{48}Ca+^{27}Al (40 MeV/A). Vertical red and black dotted lines mark the corresponding v_{CM} and v_B.

The mean values of the fragment charge (Z), fragment mass (A), total multiplicity of charged particles (M_{tot}) and longitudinal velocity ($v_{||}$) extracted from the experimental data are given in the Table 3.1 for each FAZIA-PRE system. The ⟨Z⟩ and ⟨A⟩ values for ^{27}Al target systems are higher than that of ^{12}C target systems at both E_B and ^{40}Ca target system at E_B = 25 MeV/A. The M_{tot} is higher in E_B = 40 MeV/A systems than E_B = 25 MeV/A systems. M_{tot} is lower for ^{27}Al target systems than other systems. The $v_{||}$ is more or less the same for systems corresponding to a specific E_B. The reasons behind these trends in the mean values are discussed in further sections about the experimental data comparison.

Projectile	^{48}Ca (25 MeV/A)			^{48}Ca (40 MeV/A)	
Target	^{12}C	^{27}Al	^{40}Ca	^{12}C	^{27}Al
$\langle Z \rangle$	11.49	13.54	11.61	8.37	8.99
$\langle A \rangle$	25.14	30.49	26.16	17.83	19.22
$\langle M_{tot} \rangle$	1.29	1.06	1.24	1.52	1.2
$\langle v_{\parallel} \rangle$ [cm/ns]	6.31	6.4	6.4	7.6	7.62

Table 3.1: Mean values of basic reaction observables for each FAZIA-PRE system. Z: fragment charge, A: fragment mass, M_{tot}: total multiplicity of charged particles, $v_{\parallel}$: longitudinal velocity.

The mean multiplicities of the light-charged particles (LCPs) are also given in the Table 3.2. These values were calculated from all events including the ones with zero LCP multiplicities. It can be seen that ^{4}He is most abundant and ^{3}He is the least abundant among these LCPs.

Projectile	^{48}Ca (25 MeV/A)			^{48}Ca (40 MeV/A)	
Target	^{12}C	^{27}Al	^{40}Ca	^{12}C	^{27}Al
$\langle M_p \rangle$	0.04	0.03	0.05	0.07	0.06
$\langle M_d \rangle$	0.02	0.02	0.03	0.04	0.04
$\langle M_t \rangle$	0.02	0.01	0.02	0.04	0.03
$\langle M_{^3He} \rangle$	0.007	0.003	0.01	0.02	0.01
$\langle M_{^4He} \rangle$	0.3	0.1	0.3	0.4	0.3

Table 3.2: Mean multiplicities of proton (M_p), deuteron (M_d), triton (M_t), helium-3 ($M_{^3He}$) and helium-4 ($M_{^4He}$) for each FAZIA-PRE system.

The Fig. 3.1 and the tables shown above provide an idea of the overall data obtained from the FAZIA-PRE experiment for all the five systems. The detailed comparison of this data is given in the next section.

3.1 Comparison for basic reaction observables

With respect to target mass

To compare the data w.r.t. the target mass, the other variable, i.e. beam energy (E_B) has to be kept fixed for the compared systems. The systems are compared in the following manner: (1): ^{48}Ca (25 MeV/A) beam with ^{12}C, ^{27}Al and ^{40}Ca targets; (2): ^{48}Ca (40 MeV/A) beam with ^{12}C and ^{27}Al targets. So, there are two sets of data w.r.t. target mass, each for 25 and 40 MeV/A beams. The colour scheme adapted in this chapter is solid circles for E_B

= 25 MeV/A systems, solid triangles for E_B = 40 MeV/A systems and black, red and blue colours representing ^{12}C, ^{27}Al and ^{40}Ca target systems, respectively. The basic reaction observables, Z, A and M_{tot} of the fragments are shown in Fig. 3.2 w.r.t. target mass. There are two columns for each E_B (= 25 and 40 MeV/A).

In the Z distributions (Fig. 3.2(a) and (b)), the peak around Z=20, i.e. the Z of projectile, confirms the abundance of QP fragments. The relative probability of the light and medium mass fragments is expected to increase with increasing target mass. This is correlated to the fact that with increasing target mass, the interaction cross-section increases. So, due to increasing cross-section, there is more interaction between the participants resulting into more dissipative collisions for higher target mass. But this effect is only seen for Z∼7-13. For the fragments with Z<7, fragments from ^{27}Al target systems have strange behaviour. They have relative probability lower than what is expected (to be in the middle of ^{12}C and ^{40}Ca target systems). A possible explanation to this observation can be that it can be seen from Table.3.3, that the values of neutron and proton separation energies (S) for ^{27}Al target is lower than that of the other targets. So there could possibly be an increased pre-equilibrium emission of light fragments in all directions leading to lesser light fragments reaching the detector. Coming back to Z=20, the relative probability of the fragments increases with increasing target mass at this point. This can be connected to the fact that with increasing target mass, there is an increase in the grazing angle, θ_{gr} (see Table 2.2) which ultimately leads to an increase in the elastic scattering events. Thus, increasing the target mass leads to increased elastic collisions and more detection of projectile-like fragments (PLFs). It is to be noted that although the collisions are more dissipative with increasing energy, but in the given acceptance range of the detector, these elastic scattering events overshadow the dissipative nature of the whole system. This increase in the elastic collisions also explains the distribution of fragments in the range of Z∼13-19. As increased amount of PLFs are detected, there are less heavy fragments other than the PLFs coming in as evaporation residues from the reaction. Thus, there is lower relative yield of fragments closer to the projectile coming from a heavier target system. This was also reported in [94].

	$^{12}_{6}$C	$^{27}_{13}$Al	$^{40}_{20}$Ca	$^{48}_{20}$Ca
S(2n) [MeV]	18.72	13.06	15.64	9.95
S(2p) [MeV]	15.96	8.27	8.33	15.81

Table 3.3: Separation energies (S) of $^{12}_{6}$C, $^{27}_{13}$Al, $^{40}_{20}$Ca and $^{48}_{20}$Ca, taken from [93].

A similar explanation can be given for the trends seen in fragment mass (A) distribution given in Fig. 3.2(c) and (d). The main points to be noted from A distribution is that the fragment yields become very low at two points, A=5 (^{5}He) and A=8 (^{8}Be). This is due to a very short lifetime of ^{5}He with half-life ≈ 10^{-22}s and ^{8}Be being highly unstable state with half-life ≈ 10^{-16}s breaking into two ^{4}He atoms. The rest of the A distribution has similar

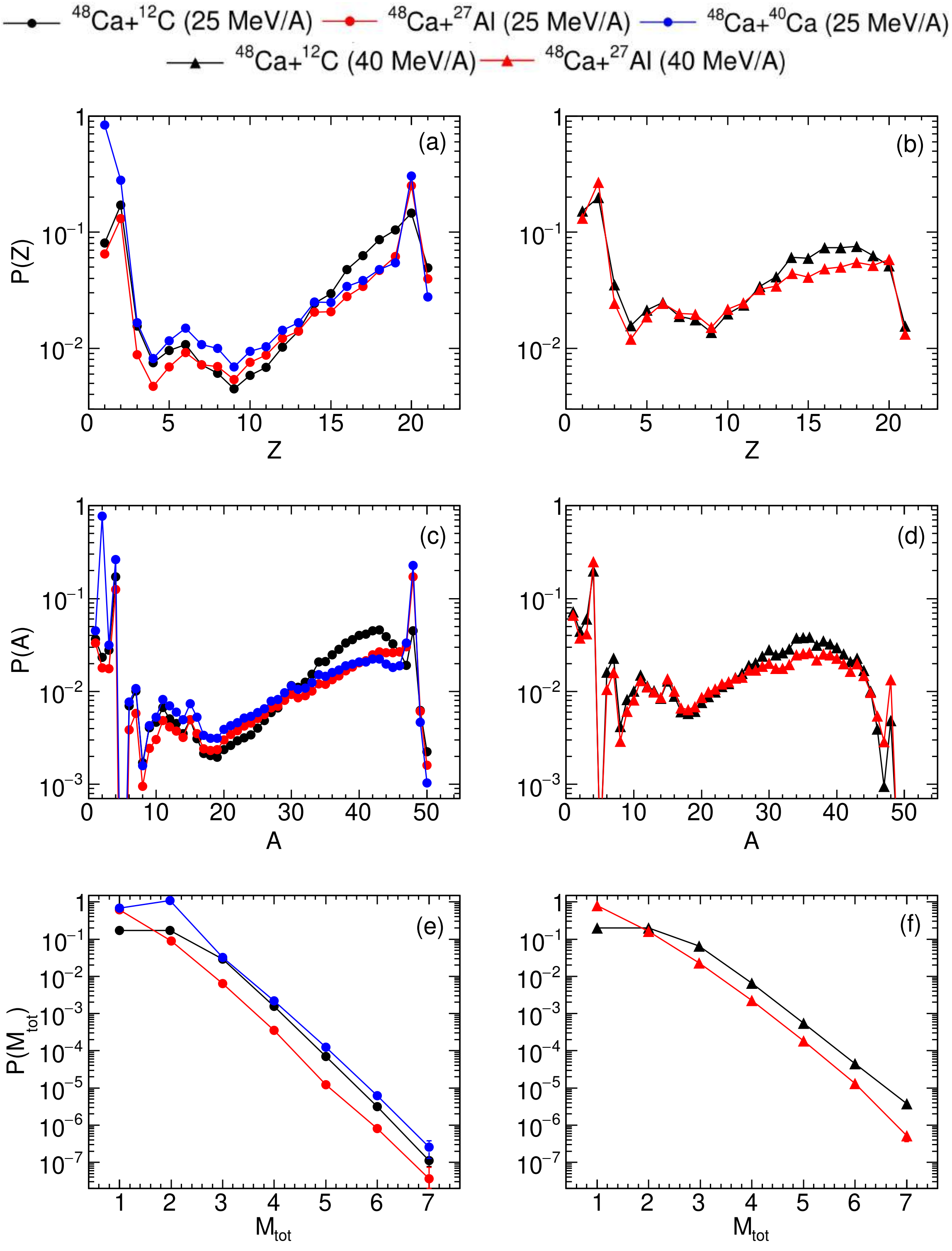

Fig. 3.2: Comparison of basic reaction observables w.r.t. target mass. Fragment charge (Z), mass (A) and charged particle multiplicity (M_{tot}) distributions for (a), (c), (e): ^{48}Ca at 25 MeV/A (circles) and (b), (d), (f): ^{48}Ca at 40 MeV/A (triangles), respectively, on ^{12}C (black), ^{27}Al (red) and ^{40}Ca (blue) targets. There is no ^{40}Ca target for ^{48}Ca beam reaction at 40 MeV/A.

trends w.r.t. target mass like the Z distribution.

The M_{tot} distribution is shown in Fig. 3.2(e) and (f). Recalling the fact that the interaction between projectile and target increases with increasing target mass leading to formation of more fragments, the relative probability for M_{tot} should also increase with increasing target mass. For ^{27}Al target systems, the relative probability for M_{tot} >1 decreases due to the same reason of its lowest neutron and proton separation energies explained previously. At M_{tot} = 1, the increase of elastic scattering with target mass increases relative probability of a single nucleus detection.

Another reaction observable is the longitudinal velocity of the fragments ($v_{||}$), i.e. the fragment velocity along the beam axis. The Z and $v_{||}$ correlation was presented in Fig. 3.1 for all systems. The comparison of this correlation between 25 MeV/A systems (Fig. 3.1(a), (b) and (c)) shows that the overall distribution of the fragments is relatively similar due to detection of mostly QP fragments. The only difference that can be pointed out is the effect of elastic scattering events around the PLFs ($Z \sim 20$, $v_{||} \sim v_B$). The spread of the PLFs (red area) becomes narrower as the target mass increases indicating that there are more elastic scattering events in heavier target systems. For 40 MeV/A systems (Fig. 3.1(d) and (e)), it is difficult to observe the narrowing of the red area because at this beam energy, the whole system gets fragmented producing a large number of smaller fragments. This reason can be backed up from the comparison of the data w.r.t. beam energy.

With respect to beam energy (E_B)

For the comparison of experimental data w.r.t. beam energy (E_B), there are four such systems out of five. ^{48}Ca + ^{12}C and ^{48}Ca + ^{27}Al systems, both at 25 and 40 MeV/A. Comparison is done w.r.t. E_B by keeping the systems fixed for each target. There is no data for ^{48}Ca + ^{40}Ca at 40 MeV/A so this system cannot be investigated w.r.t. E_B.

The comparison of Z, A and M_{tot} distributions w.r.t. E_B is presented in Fig. 3.3. There are two columns for the two systems. Looking at the Z and A distributions in Fig. 3.3(a)-(d), it can be observed that the relative probability of fragments (light to medium-heavy) is much higher in 40 MeV/A systems. Also, around the Z and A of the projectile (heavier fragments), the fragment yield is lower at 40 MeV/A than at 25 MeV/A suggesting that there is increased fragmentation at higher E_B. Thus, at 40 MeV/A, multi-fragmentation should be a dominant channel. The M_{tot} distribution shown in Fig. 3.3(e) and (f) also confirms that multi-fragmentation should dominate at E_B = 40 MeV/A. The relative probability of the events with M_{tot} >2 is higher in 40 MeV/A systems than the 25 MeV/A systems. So, relatively more fragments are produced per event while moving from lower to higher beam energy.

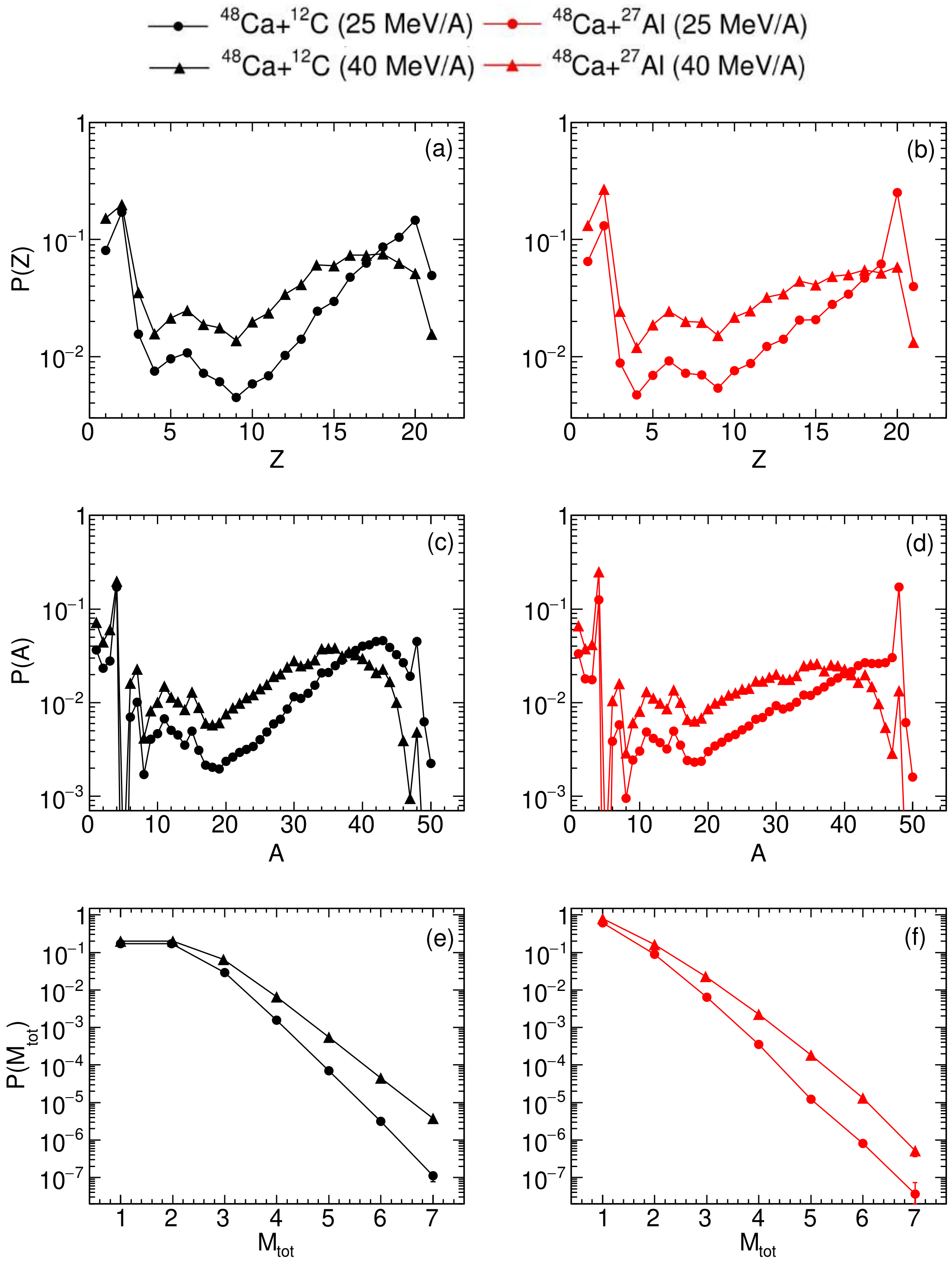

Fig. 3.3: Comparison of basic reaction observables w.r.t. beam energy. Fragment charge (Z), mass (A) and charged particle multiplicity (M$_{tot}$) distributions for (a), (c), (e): ^{48}Ca + ^{12}C (black) and (b), (d), (f): ^{48}Ca + ^{27}Al (red) at 25 (circles) and 40 MeV/A (triangles), respectively.

3.2 Comparison for isospin observables

To compare the FAZIA-PRE data w.r.t. target mass and beam energy for isospin content of the fragments, a similar approach to the one used in [83] was followed. To observe the effects of isospin transport on the fragments, the neutron-to-proton ratio (N/Z) is the isospin related observable that was chosen. To obtain the N/Z content of the fragments, a fine detailed neutron distribution for each Z value is important. It should be noted that there is no neutron detection in FAZIA. Due to the good isotopic resolution of the FAZIA detector, up to Z~20, the neutron distribution from experimental data could be plotted for each isotope by directly using N = A − Z.

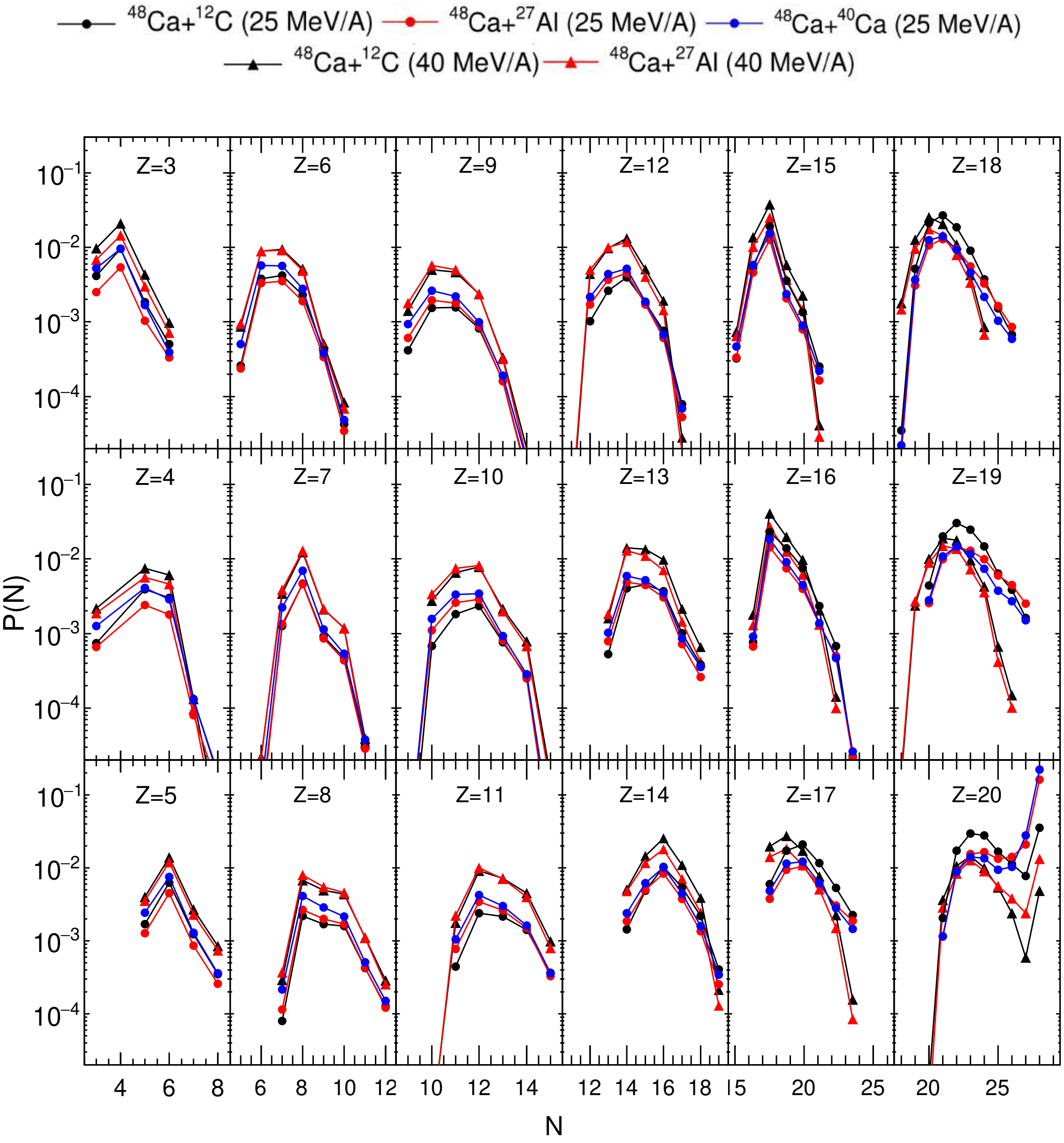

Fig. 3.4: Neutron (N) probability distribution w.r.t. the target mass for all FAZIA-PRE systems representing the isotopic content of fragments for Z=3−20.

Due to the good isotopic resolution of the FAZIA detector, up to Z~20, the neutron distribution from experimental data could be plotted for each isotope by directly using N = A − Z. Fortunately, the FAZIA-PRE data had a range of Z also up to ~20 ($^{48}_{20}$Ca projectile) because of the presence of mostly QP fragments. So, N distributions for all systems is shown in Fig. 3.4 for all Z (>2). These N distributions show the isotopic content of the reaction products formed in the experiment for each given Z. In general, the relative yield of neutrons is observed to be increasing with increasing target mass and beam energy. For Z=20, the relative yield is highest at N=28, pointing towards an abundance of projectile-like fragments (PLFs). Moreover, the main purpose of these N distributions is to get the mean neutron number ⟨N⟩ for each Z to investigate the fragment isospin content. In this part of research, only the data for fragments with Z>2 was used because the ⟨N⟩ for Z=1, 2 fragments is always fixed due to abundance of protons and ^{4}He. For the fragments with Z>2, the ⟨N⟩ should depend on the most probable isotope for each Z. This data is compared w.r.t. target mass and beam energy in further sub-sections.

With respect to target mass

Following the procedure from [83], to investigate the isospin transport, the ⟨N⟩/Z values obtained from Fig. 3.4 were plotted as a function of Z and are shown in Fig. 3.5 w.r.t. target mass. There are two panels, (a) and (b) for 25 and 40 MeV/A systems, respectively. It is observed that the lighter fragments have higher ⟨N⟩/Z than the heavier ones.

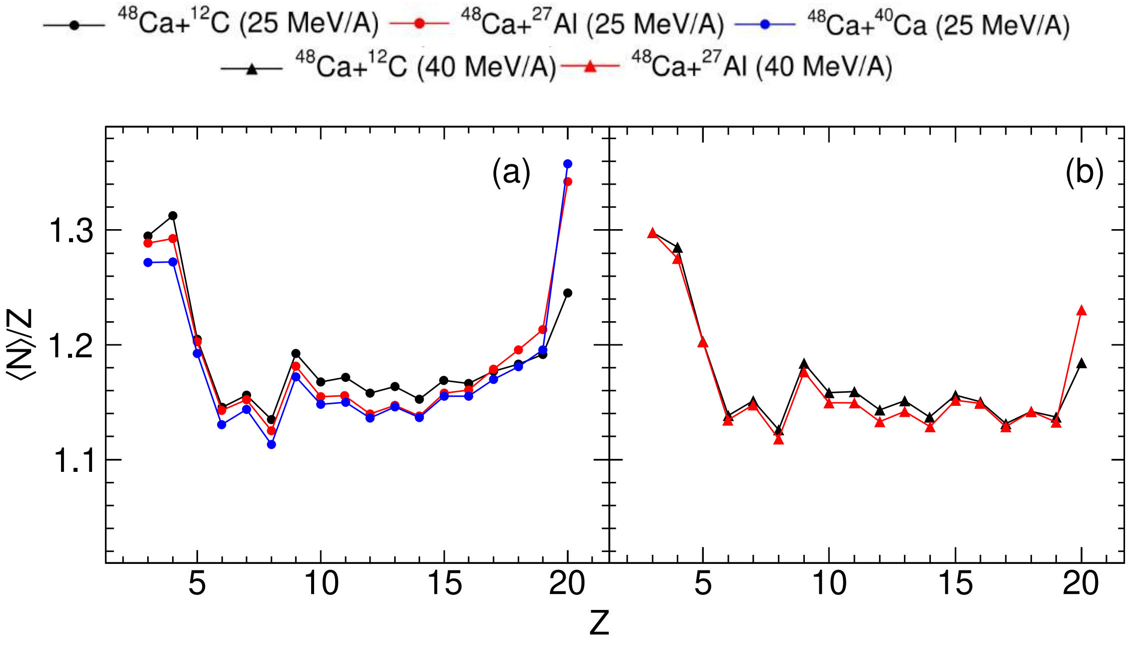

Fig. 3.5: ⟨N⟩/Z as a function of Z w.r.t. target mass for (a): ^{48}Ca projectile at 25 MeV/A (circles); (b): ^{48}Ca projectile at 40 MeV/A (triangles) on ^{12}C (black), ^{27}Al (red) and ^{40}Ca (blue) targets. There is no ^{40}Ca target for ^{48}Ca at 40 MeV/A.

Also there is a sudden increase in ⟨N⟩/Z at Z=20 because the projectile, ^{48}Ca, is neutron rich. Unlike the observations from [94], where no significant difference in the ⟨N⟩/Z of the fragments was seen w.r.t. target mass, in this FAZIA-PRE data, target dependence was observed because targets under consideration were almost N/Z symmetric. So the detected QP fragments should show the effect of changing target mass on N/Z. The main outcome here is that the fragment ⟨N⟩/Z decreases with increasing target mass. This observation is confirmed by Fig. 3.6. It shows the difference (δ_T⟨N⟩/Z) between fragment ⟨N⟩/Z of different target systems as a function of Z. The Fig. 3.6(a), shows the $\delta_T\langle N\rangle/Z = \langle N\rangle/Z_{^{27}Al} - \langle N\rangle/Z_{^{12}C}$ (red solid circles) and $\delta_T\langle N\rangle/Z = \langle N\rangle/Z_{^{40}Ca} - \langle N\rangle/Z_{^{12}C}$ (blue solid circles) target systems for ^{48}Ca (25 MeV/A) beam. The Fig. 3.6(b) shows the $\delta_T\langle N\rangle/Z = \langle N\rangle/Z_{^{27}Al} - \langle N\rangle/Z_{^{12}C}$ (red solid triangles) target systems for ^{48}Ca (40 MeV/A) beam. In all cases, the δ_T⟨N⟩/Z stays negative (except for PLFs) which indicates that the fragment ⟨N⟩/Z is lower for higher target mass systems. Also, the for 25 MeV/A beam, δ_T⟨N⟩/Z corresponding to the ^{40}Ca target system is more negative than the δ_T⟨N⟩/Z for ^{27}Al target system. This also confirms that fragment ⟨N⟩/Z decreases with increasing target mass.

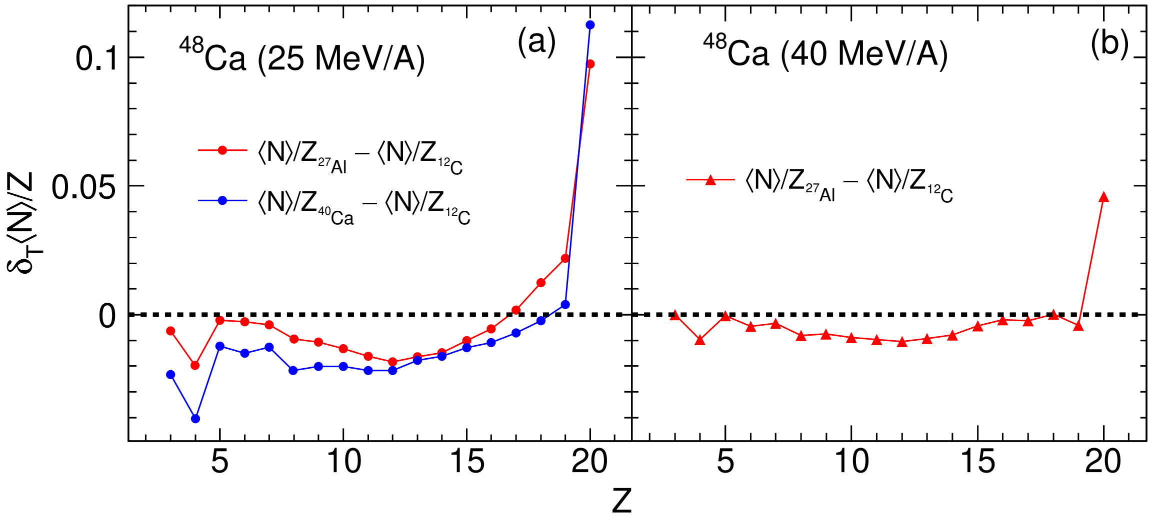

Fig. 3.6: The difference δ_T⟨N⟩/Z as a function of Z w.r.t. target mass for (a): $\langle N\rangle/Z_{^{27}Al} - \langle N\rangle/Z_{^{12}C}$ (red circles) and $\langle N\rangle/Z_{^{40}Ca} - \langle N\rangle/Z_{^{12}C}$ (blue circles) target systems with ^{48}Ca (25 MeV/A) beam and (b): $\langle N\rangle/Z_{^{27}Al} - \langle N\rangle/Z_{^{12}C}$ (red triangles) target systems with ^{48}Ca (40 MeV/A) beam.

This could be correlated to the fact that the total N/Z of the system decreases with increasing target mass (see N/Z total in Table 2.1). A simple reason being that for smaller target mass, there are less target nucleons to interact with, which can easily be exchanged in the interactions. On increasing the target mass, the number of target nucleons increases and also the elastic scattering of the projectile increases due to increase in the grazing angle (θ_{gr}). So, the nucleon exchange becomes difficult. For the same reason, at Z=20, i.e., the Z of the projectile, this effect on N/Z is opposite due to the dominance of the elastic scattering events and PLFs staying neutron rich on detection.

There are also small contributions of fragments coming from the dilute neck region and some pre-equilibrium emissions. These fragments are emitted in all directions, but the ones that are emitted in the direction of the multi-detector and are energetic enough to reach it, can be detected. The pre-equilibrium emissions in such case where detector acceptance is small (~2−16°), would mostly be only LCPs (Z<3). Thus, the effect on the ⟨N⟩/Z from pre-equilibrium emission of charged particles cannot be accounted from this data. Due to the superior forward acceptance angles of the detector setup, the neck fragments could not be chosen using angular correlations. So, to look for neck contributions, the ⟨N⟩/Z as a function of the longitudinal velocity ($v_{||}$) can be plotted (Fig. 3.7). It is observed for 25 MeV/A systems in Fig. 3.7(a), that the ⟨N⟩/Z is quite high around the beam velocity (v_B). It can be explained that around the v_B, ⟨N⟩/Z is higher due to the detection of the QP coming from a neutron rich projectile which retains some memory of the entrance channel also with an increased effect from elastic scattering events. For 40 MeV/A systems in Fig. 3.7(b), the ⟨N⟩/Z near v_B is not high as the whole system gets fragmented at this beam energy and the QP breaks into lighter fragments to normalise the ⟨N⟩/Z. On the other hand, high ⟨N⟩/Z around v_{CM} is observed in all systems. These fragments with high ⟨N⟩/Z and $v_{||}$ comparable to the v_{CM} could have either been emitted in the backward direction in the QP reference frame or they could have been emitted from the neck region formed between the

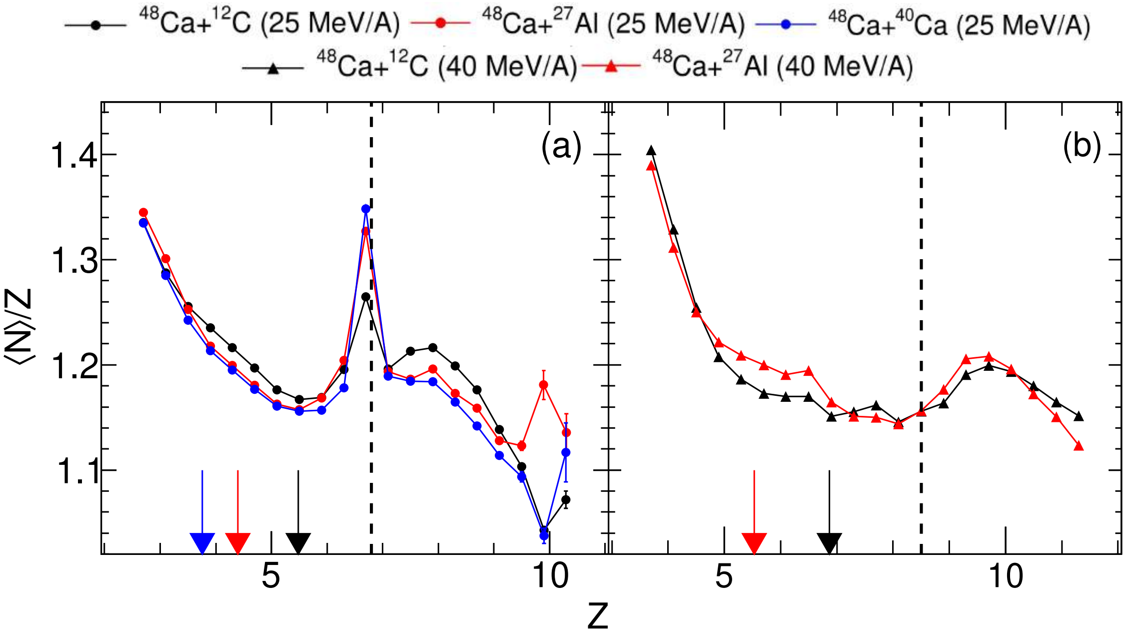

Fig. 3.7: ⟨N⟩/Z as a function of longitudinal velocity ($v_{||}$) w.r.t. target mass for (a): ^{48}Ca projectile at 25 MeV/A (circles); (b): ^{48}Ca projectile at 40 MeV/A (triangles) on ^{12}C (black), ^{27}Al (red) and ^{40}Ca (blue) targets. There is no ^{40}Ca target for ^{48}Ca at 40 MeV/A. Downward arrows represent the v_{CM} for each system and vertical dashed lines mark the v_B.

projectile and target in peripheral collisions [95–97].

There are two important points regarding the nuclear collisions at intermediate energies to understand the results presented further. The Fig. 3.8(a) is taken from [9] and modified to explain the underlying physics:

- The Fig. 3.8(b) shows the QP in its frame of reference. The fragments with $v_{||}$ comparable to the v_B are emitted in forward direction (FWD) and the fragments with slightly lower $v_{||}$ are emitted in the backward direction (BWD) in the QP reference frame.

- The Fig. 3.8(c) shows the elongated neck formation between the projectile and target in a peripheral collision. The "hierarchy effect" [98, 99] shown by these neck fragments leads to emission of light fragments (Z~3-6) with lower $v_{||}$ which is comparable to the v_{CM} from the very central dilute region of the neck. The fragments emitted from denser parts of the neck, i.e., near QP and QT have higher $v_{||}$ than v_{CM} but lower than the BWD or FWD fragments.

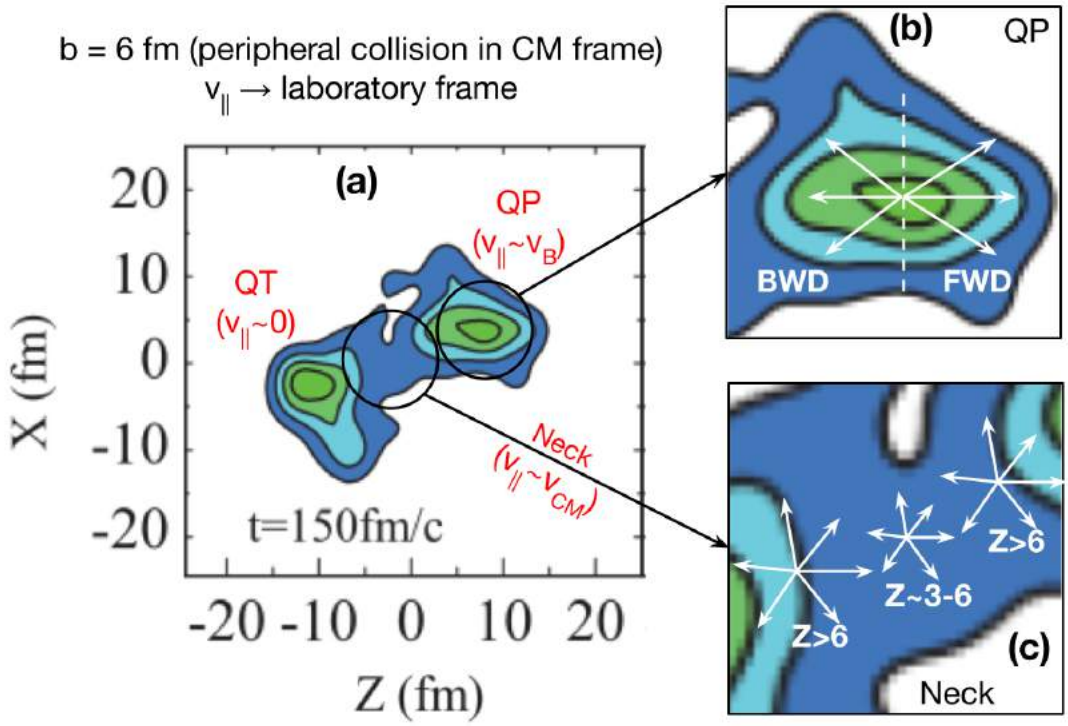

Fig. 3.8: Schematic diagram of (a): neck formation in peripheral collision (b=6 fm), taken and modified from [9]; (b): Zoom in on the QP region showing the directions of backwards (BWD) and forward (FWD) emitted fragments in QP reference frame; (c): Zoom in on the neck region of the colliding system showing the hierarchy effect in fragment emission.

Continuing the approach of [83], the presence of isospin drift was confirmed for the FAZIA-PRE data. For this, the ⟨N⟩/Z as a function of $v_{||}$ w.r.t. target mass for every Z from Z=3 to Z=20 as shown in Fig. 3.9 and Fig. 3.10 for 25 and 40 MeV/A systems, respectively provides a detailed structure of fragment ⟨N⟩/Z. Here, the range of $v_{||}$ for 25 and 40 MeV/A systems was chosen in such a way that it covers both v_{CM} and v_B regions of velocity space for all systems. From these plots, one can see that the dependence of ⟨N⟩/Z on target mass is similar to what was observed in Fig. 3.5, i.e., decreasing ⟨N⟩/Z with increasing target mass. For lighter fragments (Z ~ 3 – 6), there are higher values of ⟨N⟩/Z around the v_{CM}. Then, with increasing Z, the ⟨N⟩/Z trend becomes more flat and then increases again for heavier fragments (Z ~ 16 – 20).

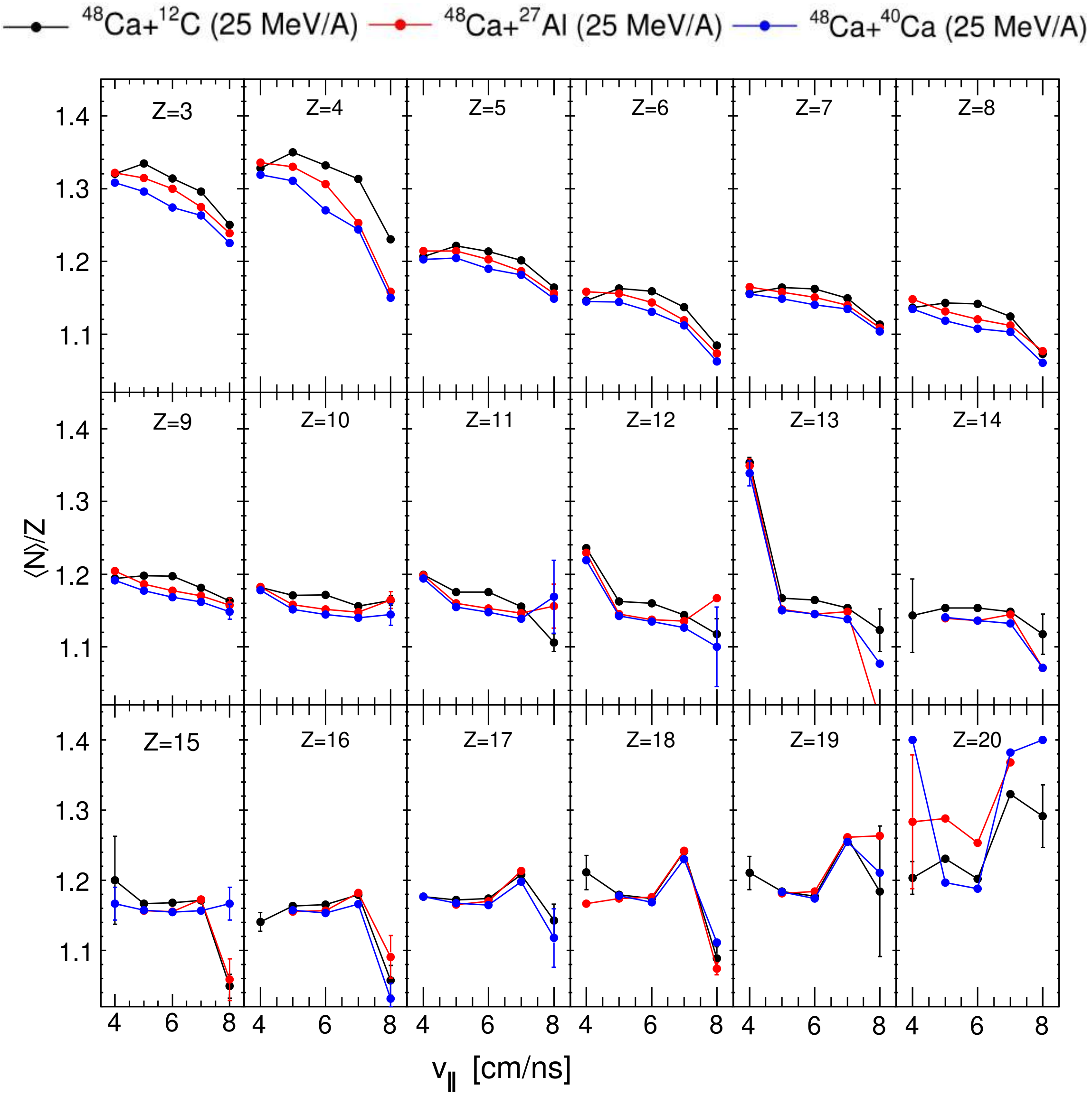

Fig. 3.9: ⟨N⟩/Z as a function of longitudinal velocity ($v_{||}$) w.r.t. target mass for 25 MeV/A systems for each Z = 3 – 20, separately. Black, red and blue circles represent ^{12}C, ^{27}Al and ^{40}Ca targets, respectively.

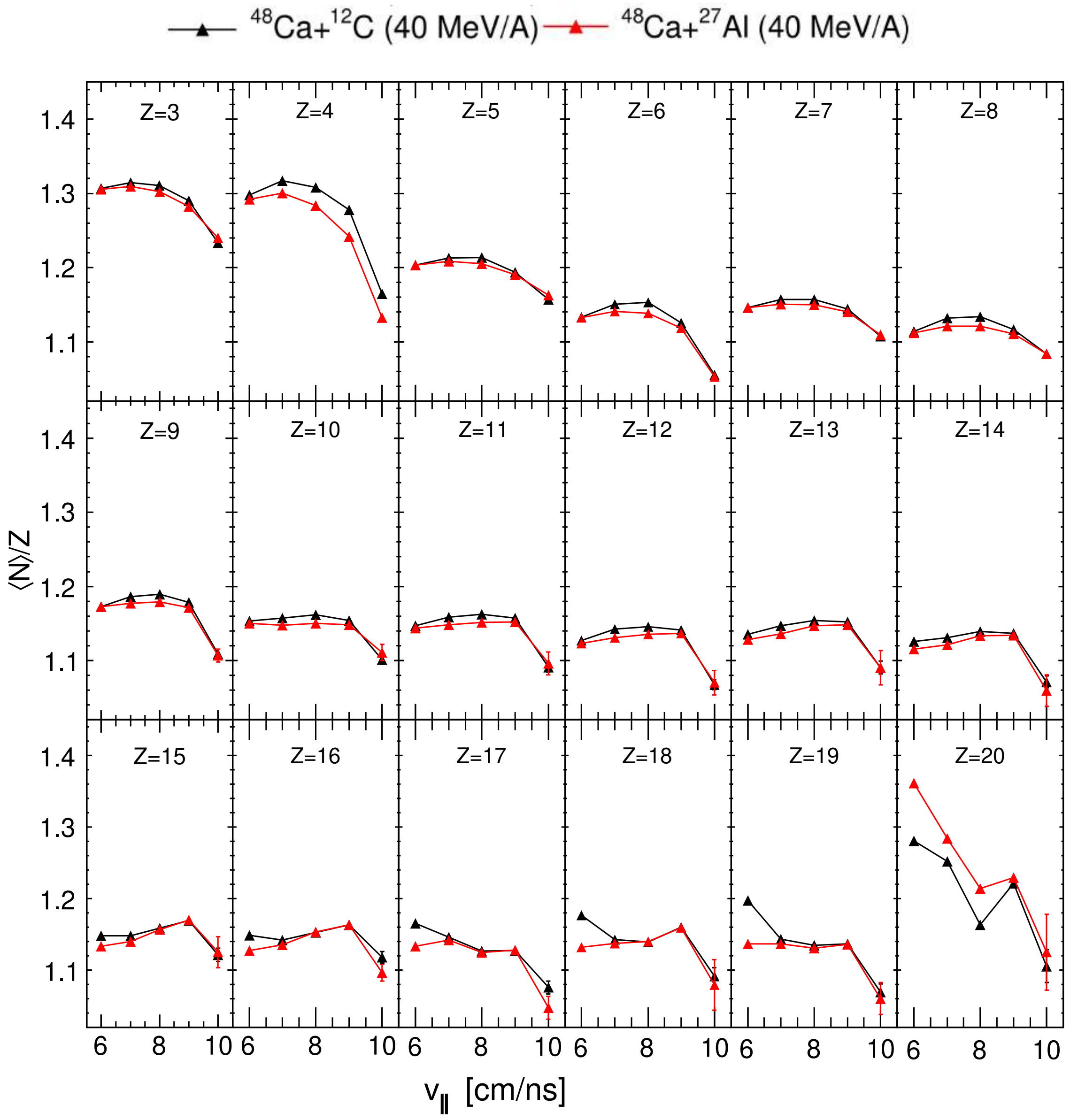

Fig. 3.10: ⟨N⟩/Z as a function of longitudinal velocity ($v_{||}$) w.r.t. target mass for 40 MeV/A systems for each Z = 3 – 20, separately. Black and red triangles represent ^{12}C and ^{27}Al targets, respectively.

The heavier fragments, i.e. fragments that have Z closer to the projectile (Z=20), have higher ⟨N⟩/Z around v_B simply because they are heavy residues from the projectile that was neutron rich. Also for Z=20 in 40 MeV/A systems, the v_{CM} region has higher ⟨N⟩/Z than the v_B. This is possible due to increased fragmentation and pre-equilibrium emissions from projectile at this beam energy (discussed in next sub-section).

According to the explanation for Fig. 3.8(c), the lighter fragments near v_{CM} region must be emitted from the most central part of the neck. The high ⟨N⟩/Z of these fragments is a possible evidence of neutron enrichment of the neck, also known as isospin drift. Due to the lack of projectiles with different N/Z in this research work, effects of isospin diffusion process could not be discussed. But the effects of isospin drift could still be investigated. To verify the possible evidence for isospin drift, the fragments were selected according to their $v_{||}$ within the QP phase space. Just like in [83], the phase space was split for FWD and BWD fragments. In the Fig. 3.9 and Fig. 3.10, the $v_{||}$ was plotted within a range of around 4 cm/ns. So, to divide the space in to two parts, the values of $v_{||}$ which were slightly lower than each v_B were chosen (see Fig. 3.11). For 25 MeV/A systems, the phase space was divided at 6 cm/ns and for 40 MeV/A systems, at 8 cm/ns. The region with $v_{||} \leq 6$ cm/ns (for 25 MeV/A) or 8 cm/ns (for 40 MeV/A) should have BWD fragments along with some possible neck emissions. On the other hand, the region with $v_{||} > 6$ cm/ns (for 25 MeV/A) or 8 cm/ns (for 40 MeV/A) should consist of the FWD fragments.

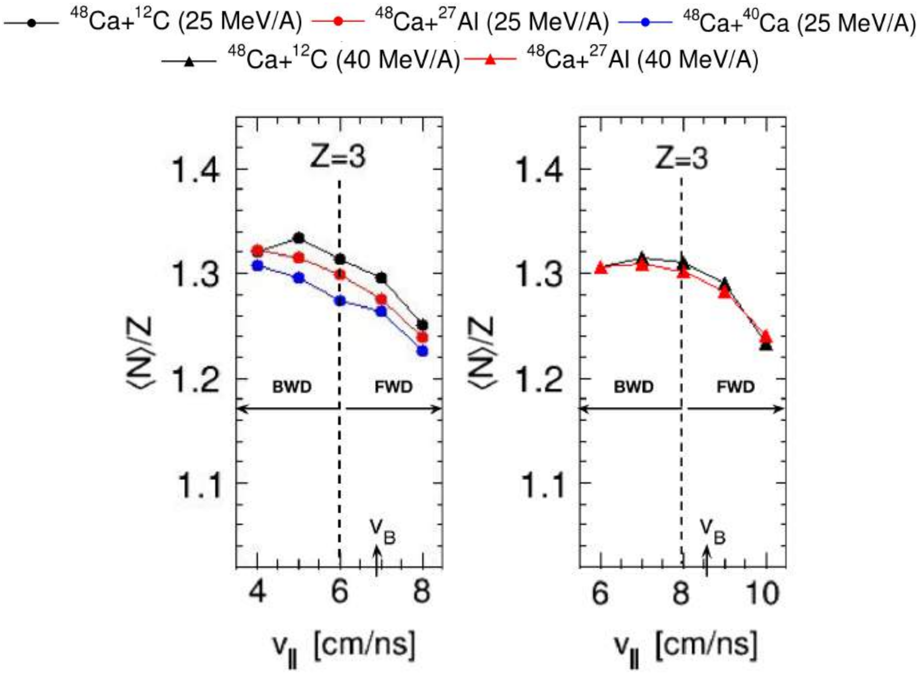

Fig. 3.11: Splitting the velocity space from ⟨N⟩/Z vs $v_{||}$ correlation to select backward (BWD) and forward (FWD) emitted fragments in the QP phase space.

It was established from Fig. 3.9 and Fig. 3.10 that the lighter fragments (Z~3-6) have high ⟨N⟩/Z around the v_{CM} and heavier fragments have high ⟨N⟩/Z around v_B. This was confirmed by plotting the difference of ⟨N⟩/Z of BWD and FWD fragments, $\Delta\langle N\rangle/Z = \langle N\rangle/Z_{BWD} - \langle N\rangle/Z_{FWD}$ as a function of Z as shown in the Fig. 3.12(a) and (b) for 25 and 40 MeV/A systems, respectively. The Δ⟨N⟩/Z for fragments with $Z \sim 7-15$ almost approaches zero. This is visible due to the effect of isospin diffusion, that should affect all the BWD and FWD fragments in same ways, gets cancelled out. This suggests that the positive value of Δ⟨N⟩/Z for lighter fragments is due to the high ⟨N⟩/Z of the fragments coming from the neutron enriched neck. This confirms the effects of isospin drift. The negative Δ⟨N⟩/Z for 25 MeV/A systems in Fig. 3.12(a) is related to the fact that the ⟨N⟩/Z of FWD fragments

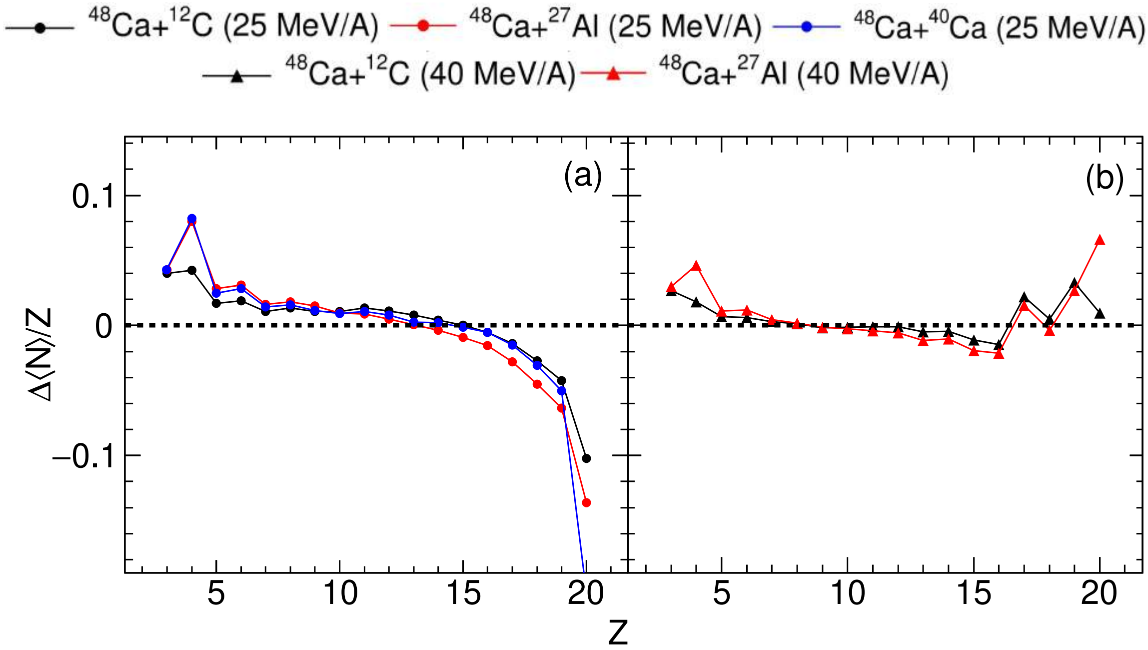

Fig. 3.12: Δ⟨N⟩/Z = ⟨N⟩/Z_{BWD}−⟨N⟩/Z_{FWD} as a function of Z w.r.t. target mass for (a): ^{48}Ca projectile at 25 MeV/A (circles) ; (b): ^{48}Ca projectile at 40 MeV/A (triangles) on ^{12}C (black), ^{27}Al (red) and ^{40}Ca (blue) targets. There is no ^{40}Ca target for ^{48}Ca at 40 MeV/A.

is high due to the elastic scattering events leading to detection of a neutron rich PLF. The target dependence can be seen at Z=20 because of these elastic scattering events in such a way that the heavier is the target, the more is the negative value of Δ⟨N⟩/Z. The same can not be said for 40 MeV/A systems in Fig. 3.12(b) as the Δ⟨N⟩/Z completely changes from negative to positive as Z approaches near the projectile. This effect is probably related to the fast-neutron emissions and is discussed in the next sub-section. For the rest of the fragments, in general, the effects of N/Z in backward or forward directions in QP reference frame increase with increasing target mass.

With respect to beam energy (E_B)

This sub-section presents the results of research on the effect of beam energy on fragment N/Z. A similar procedure from the previous sub-section was used using N distributions to plot ⟨N⟩/Z as a function of Z (Fig. 3.13) but with respect to the beam energy (E_B). Due to the detection of mostly QP fragments, the evolution of ⟨N⟩/Z as a function of Z w.r.t. E_B is expected to be higher with higher E_B. One may say that with increasing energy, the interaction time between the participants reduces and the nucleon exchange also reduces. Therefore, due to n-rich projectile, the N/Z should be relatively higher with higher E_B. But the result is opposite. It is seen in Fig. 3.13 that for both systems, (a)^{48}Ca+^{12}C and (b) ^{48}Ca+^{27}Al, the fragment ⟨N⟩/Z decreases with increasing energy.

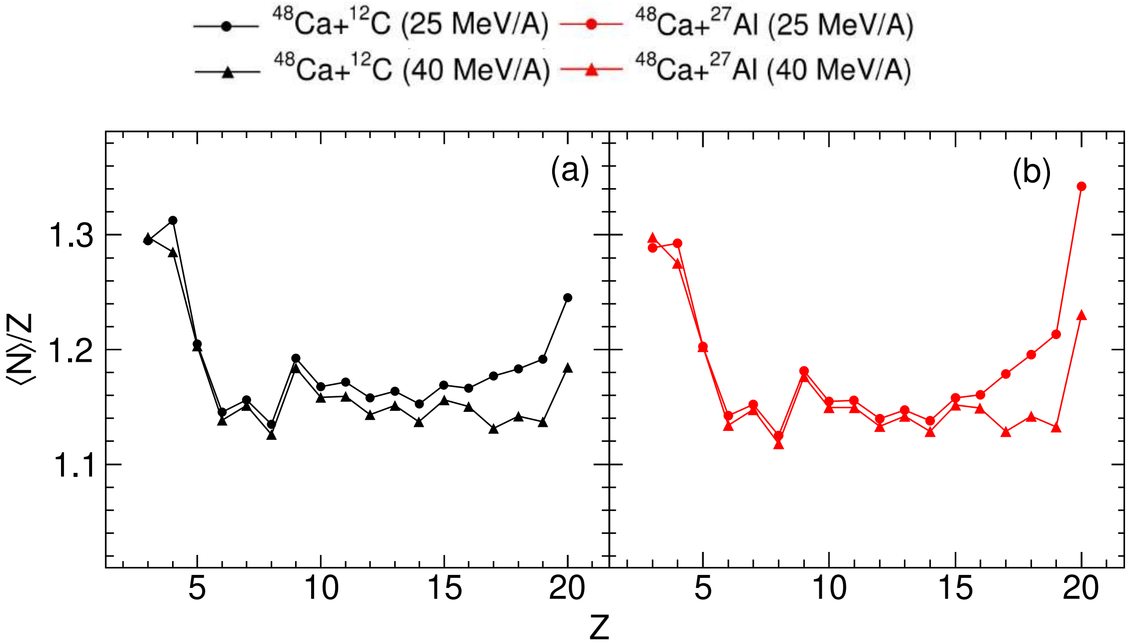

Fig. 3.13: ⟨N⟩/Z as a function of Z w.r.t. beam energy for (a): ^{48}Ca + ^{12}C (black) and (b): ^{48}Ca + ^{27}Al (red) at 25 (circles) and 40 MeV/A (triangles), respectively.

To confirm this observation, the difference between the ⟨N⟩/Z for 25 MeV/A system and 40 MeV/A system, δ_E⟨N⟩/Z = ⟨N⟩/Z$_{25}$ − ⟨N⟩/Z$_{40}$ is shown in Fig. 3.14.

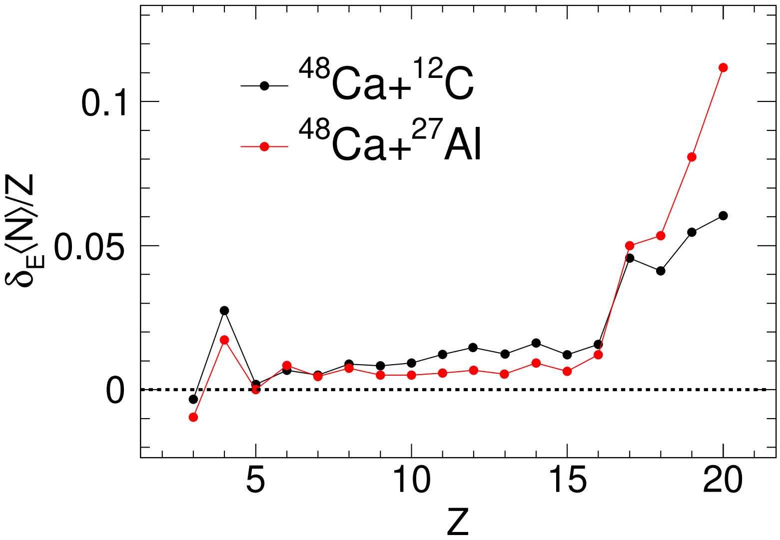

Fig. 3.14: δ_E⟨N⟩/Z = ⟨N⟩/Z$_{25}$ − ⟨N⟩/Z$_{40}$ as a function of Z w.r.t. E$_B$ for ^{48}Ca + ^{12}C (black circles) and ^{48}Ca + ^{27}Al (red circles) systems.

The value of δ_E⟨N⟩/Z is greater than zero for almost all Z, so it is confirmed that the ⟨N⟩/Z of fragments decreases with increasing beam energy. Its value is very small for fragments with Z<17 and becomes higher for Z≥17. Thus, for fragments with Z≥17, ⟨N⟩/Z changes substantially. A reasonable explanation to these observed effects could be that with higher beam energies, there are higher excitation energies for fragments. Thus, there is supposed to be higher isospin equilibration at higher beam energies due to increased multi-fragmentation. Also contributing to this effect is a rising amount of pre-equilibrium neutron emission (fast neutrons) from the projectile (here at Z=20) with increasing E_B [92]. The charged particle pre-equilibrium emissions, however, saturate around $E_B \approx 20$ MeV/A. Due to these reasons, there could be a decrease in overall N/Z of the system, both pre and post equilibrium, thus reducing the $\langle N \rangle/Z$ of the reaction products. The investigation of effects of initial neutron abundance and fast neutron emissions on N/Z of reaction products was also one of the main motives of the FAZIA-PRE experiment.

Now, by using the same procedure of splitting the fragments on the basis of their $v_{||}$ into BWD and FWD fragments, and plotting the difference $\Delta\langle N \rangle/Z$ vs Z w.r.t. E_B (Fig. 3.15), it was observed that the isospin effects on backward and forward regions in the QP phase space are more prominent (spread farther from zero line) in the 25 MeV/A systems than the 40 MeV/A systems. A simple explanation to this observation is the relation of interaction time and the beam energy. So, at higher beam energies, the interaction time between participants decreases, pre-equilibrium emission increases and hence, the effects of isospin transport decrease. Also, to explain the fact observed in previous sub-section that the $\Delta\langle N \rangle/Z$ becomes positive for $Z \geq 17$ for 40 MeV/A is due to the increased pre-equilibrium emission from projectile at higher energy which might lead to a slight fall in the $v_{||}$ of heavy fragments. Then enough of these fragments might fall in the backward emission region of the QP phase space which could lead to a positive $\Delta\langle N \rangle/Z$ for $Z \geq 17$.

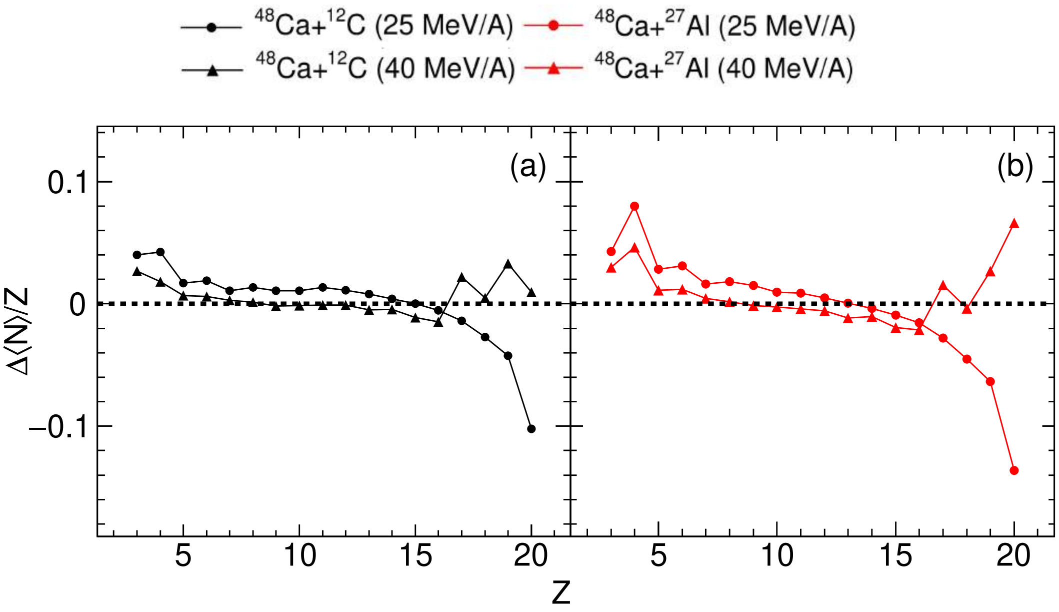

Fig. 3.15: $\Delta\langle N \rangle/Z$ as a function of Z w.r.t. beam energy E_B for (a): $^{48}Ca+^{12}C$ (black) and (b): $^{48}Ca+^{27}Al$ (red) systems at 25 (circles) and 40 (triangles) MeV/A.

The conclusions that have been drawn from this comparison of the experimental data with respect to target mass and beam energy can be further verified by making a comparison of the experimental data with some theoretical models which can reproduce the reaction dynamics. A comparison with such a model is presented in further chapters.

Chapter 4

Description of intermediate energy nuclear reactions using HIPSE

In the ongoing research for the study of nuclear reactions at the Fermi energy range (10-100 MeV/A), there are different kinds of mathematical models that explain the reaction properties and outline the dynamical characteristics of the interacting nuclei and the products formed (for example, antisymmetrized molecular dynamics (AMD) model [100] and constrained molecular dynamics (CoMD) model [101,102]). For this doctoral research work, HIPSE (Heavy-Ion Phase-Space Exploration) event generator developed by Denis Lacroix, Aymeric Van Lauwe, and Dominique Durand, explained in [103,104] was chosen for comparison with the experimental data from the FAZIA-PRE experiment (discussed earlier in Chapter 2). HIPSE event generator is a phenomenological model, i.e., it consists of both microscopic and macroscopic statistical modelling approaches, which can simulate nuclear reaction at all impact parameter ranges and can be a valuable tool for understanding different reaction processes such as neck-emissions or multi-fragmentation in peripheral and/or central collisions. It is claimed that due to a detailed reproduction of the isotopic contents of fragments, HIPSE can be a valuable tool to explore the N/Z effects in nuclear collisions around the Fermi-energy range. So, a direct comparison with the FAZIA-PRE data can help us verify whether HIPSE can actually correctly reproduce all aspects of the reaction dynamics around the Fermi energy range. In this chapter, are briefly presented, the important parts of the HIPSE model and some simulations from HIPSE model calculations for one of the systems from the FAZIA-PRE experiment.

4.1 The HIPSE framework

The HIPSE model describes the reaction in three parts, namely, approaching, re-aggreg--ation and after-burner phase. All the calculations in the model are done in the centre-of-mass frame.

1). **The approaching phase** is the one where the projectile with beam energy E_B, approaches the target at a specific impact parameter b, up to the point of maximum overlap between the two. Considering a classical two-body dynamics, the interaction potential between the projectile and target is well known for larger relative distances. For shorter distances ($r < R_T + R_P$, where R_T and R_P are target and projectile nuclear radii, respectively), it depends on the reorganization of the degrees-of-freedom (d.o.f.) as well as energy. So, the potential at $r = 0$ is given by,

$$V(r = 0) = \alpha_a V^{Froz}_{A_T A_P}(r = 0) \tag{4.1}$$

where, r is the relative distance between target and projectile, $V^{Froz}_{A_T A_P}(r = 0)$ is the energy of the system in a total overlap in the frozen density approximation and the evolution of potential as a function of α_a represents the hardness of the potential during the interaction (Fig. 4.1). One must note that in the case of near fusion barrier collisions, α_a might be the degree of reorganization of internal d.o.f. A very hard potential or α_a=1 means that there is no reorganization of the d.o.f. On the other hand, $\alpha_a < 0$ refers to an instantaneous reorganization of d.o.f. and formation of compound nucleus.

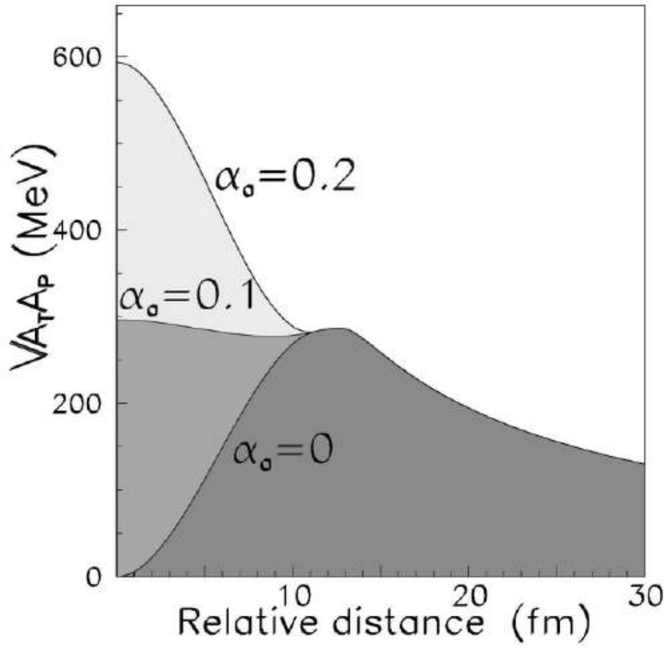

Fig. 4.1: Evolution of the nuclear potential, $V_{A_T A_P}$ as a function of the relative distance for the $^{129}Xe +^{120} Sn$ system for α_a = 0, 0.1 and 0.2. Taken from [103].

2). **The re-aggregation phase** deals with the organisation of nucleons into different fragment clusters and light particles depending upon the impact parameter, b. These clusters of particles, when created in the simulation, are called a "partition". The partition is constructed with the help of some coalescence rules in position and momentum spaces and it shows kinetic energy and angular distributions having a strong memory of the entrance channel. The determination of quasi-projectile (QP) and quasi-target (QT) regions using a participant-spectator picture concept, pre-equilibrium emissions of light charged particles (LCP) and intermediate mass fragments (IMF) is explained in this phase. Two important parameters are obtained from this phase, i.e., the percentage of nucleon-nucleon collisions within the overlap region of projectile and target (x_{coll}) and the fraction of nucleons transferred from the target (or projectile) to the projectile (or target).

Thermalization of the nucleons takes place after re-aggregation phase. Since, thermalization is not explained in microscopic approach, the excitation energy of the fragments can be calculated only by global energy balance of the whole reaction. The total energy balance of the reaction in the center-of-mass frame,

$$E_0 = Q + E_K + E_{pot} + E^* + E_{rot} \tag{4.2}$$

where E_K and E_{pot} are the sum of the kinetic and potential energies of the fragments, E_{rot} is the total rotational energy, Q is the mass energy balance between the entrance channel and the considered partition and E^* corresponds to the total excitation energy. The partition is rejected if E^* is negative because it represents inaccessible phase space. Light nuclei are considered separately from medium and heavy nuclei due to discrete nature of excited states and then E^* is shared among all fragments. The partition is then propagated in the phase space until it reaches to a chemical freeze-out. The final state interactions are considered and complex clusters get reorganised into simpler ones.

3). In **the after-burner phase**, the constructed fragments are propagated in the Coulomb field along with secondary decays. The secondary decay is achieved using statistical decay codes like SIMON and GEMINI++ event generators. SIMON is the default de-excitation code for HIPSE, but GEMINI++ is also a commonly used secondary decay code. So, it would be practical to consider both the secondary decay codes and maybe to point out certain differences in their results, if any.

SIMON event generator [105] is a statistical decay model for reactions around the Fermi energy range. It is based on facts such as, incomplete fusion dominates in this energy range, multi-fragmentation instead of LCP emission and deviations from other models at lower energies associated to time scales of particle emissions, altogether suggesting strong dynamical effects. It simulates the pre-equilibrium emissions from entrance channel and a transition to a model based on simultaneous emission of multiple fragments in the exit channel instead of successive binary decays. Thus, SIMON takes into account all possible decay channels like evaporation and symmetric fission. So, in this approach, fragments and light particles are produced at all time scales from the very early instants of the collision until freeze-out.

GEMINI++ [106] is an upgraded version of the statistical model code GEMINI. It deals with the generation of complex fragments in reactions involving light to heavy participants. Gemini++ follows the decay of a compound nucleus by a series of binary divisions. It is useful in cases where the excitation energy and spin distributions of the compound nuclei can be well defined. The partial decay widths are taken from the Hauser-Feshbach formalism for light-particle evaporation and from Moretto's generalized transition-state formalism for more symmetry divisions. This prescription provides an adequate description of the decay process for light compound nuclei. For heavier systems, the Bohr-Wheeler formalism is now used for symmetric fission and the width of the mass distributions of the fission fragments is interpolated from systematics. Overall, the GEMINI++ code works sufficiently for spin and excited states populated by heavy-ion fusion reactions.

Just to summarize, these were the three main phases briefly explaining the working of the HIPSE model. In the Fig. 4.2 (adapted from [104]), a pictorial representation of how these phases generate the partition after the primary collision, the re-organisation of the clusters and then the final fragments from the secondary decays is given. The Fig. 4.2(a) shows the approaching phase with QP and QT formation in a participant-spectator type scenario. Fig. 4.2(b) shows the partition at $t = 0$ fm/c in space configuration. Fig. 4.2(c) shows the propagated partition in the re-aggregation phase at $t = 50$ fm/c. Emission of lighter fragments is evident at this point. In Fig. 4.2(d), an intermediate de-excitation state is shown, representing the possible in-flight simultaneous statistical emissions of multiple fragments.

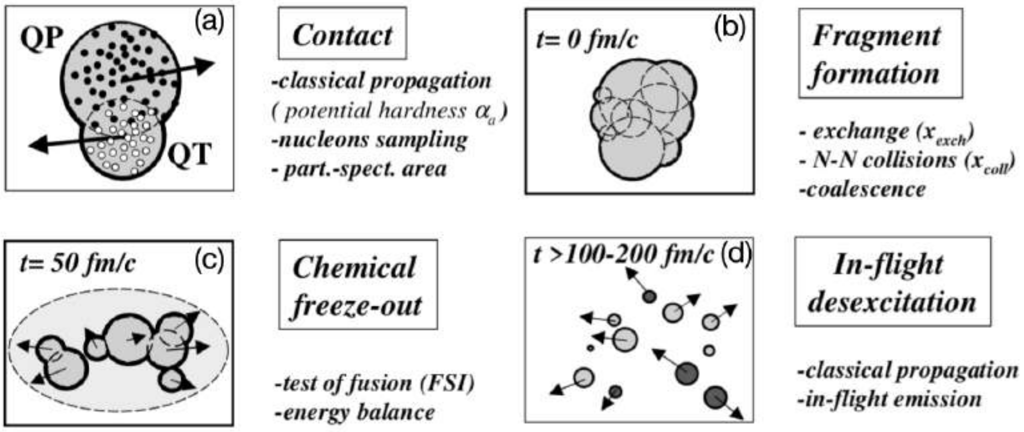

Fig. 4.2: Illustration of the different steps used to build the event generator HIPSE. (a): the entrance channel phase ; (b): the step of early formation of fragments ; (c): the phase of chemical freeze-out taking into account final state interactions (after 50 fm/c) ; (d): the after-burner step (after a few hundred fm/c). Adapted from Ref. [104]

4.2 Inputs for the Model

The HIPSE framework is completed at this point consisting of three main parameters: the hardness of the interaction potential (α_a), percentage of nucleons transferred (x_{tr}) between the projectile and target, and the percentage of nucleon-nucleon collisions inside the overlap region (x_{coll}). The values for these parameters were adjusted by comparing the calculation results with experimental data from the INDRA collaboration [68] for Xe+Sn (25, 50 MeV/A) and Ni+Ni (32, 52, 82 MeV/A) systems [107]. Variation of these parameters is shown in Fig. 4.3 as a function of beam energy (E_B). The parameters α_a and x_{coll} increase and x_{tr} decreases with E_B, respectively. Providing the fixed values of the three parameters for specific E_B, one can generate the results from the model calculations.

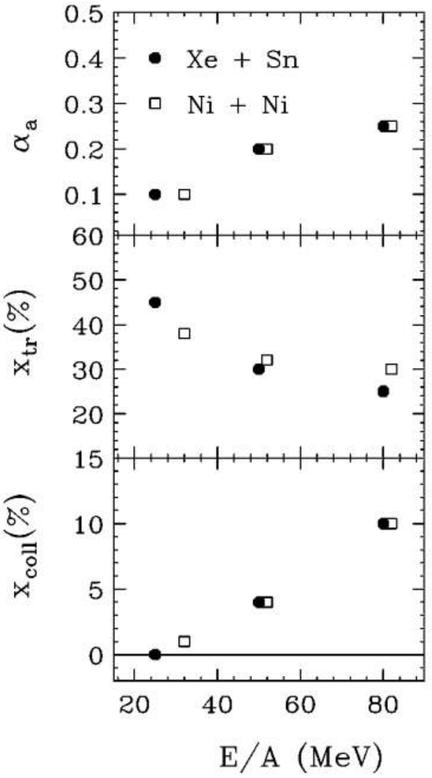

Fig. 4.3: Values of the different parameters of the model as a function of the beam energy for the reaction ^{129}Xe+^{120}Sn (filled circles) and ^{58}Ni+^{58}Ni (squares). From top to bottom, respectively, the evolution of the parameter associated with the potential hardness α_a, the rate of exchange of particles between the target and projectile, x_{tr} (in percentage), and the percentage of nucleon-nucleon collisions in the overlap region, x_{coll}. Taken from Ref. [103]

4.3 Results of HIPSE simulations

To get an idea of the data produced by HIPSE simulations, the raw results (unfiltered full 4π distribution) for ^{48}Ca+^{27}Al (40 MeV/A) system (Fig. 4.4) with respect to some basic reaction observables (charge, mass and multiplicity) are presented in this section. This system was chosen as it was a part of the FAZIA-PRE experiment and it is sufficient to describe the raw output of HIPSE simulations. For the chosen system, the values of the three main HIPSE parameters were, α_a = 0.2, x_{tr} = 0.3 and x_{coll} = 0.05. The beam energy for the system was E_B = 40 MeV/A and the maximum value of the impact parameter

$b_{max}(= R_T + R_P)$ was 8 fm. The b_{max} was chosen specifically so as to stay within the semi-peripheral collision region and not to enter the ultra-peripheral domain where the energy is insufficient to create the QP and QT.

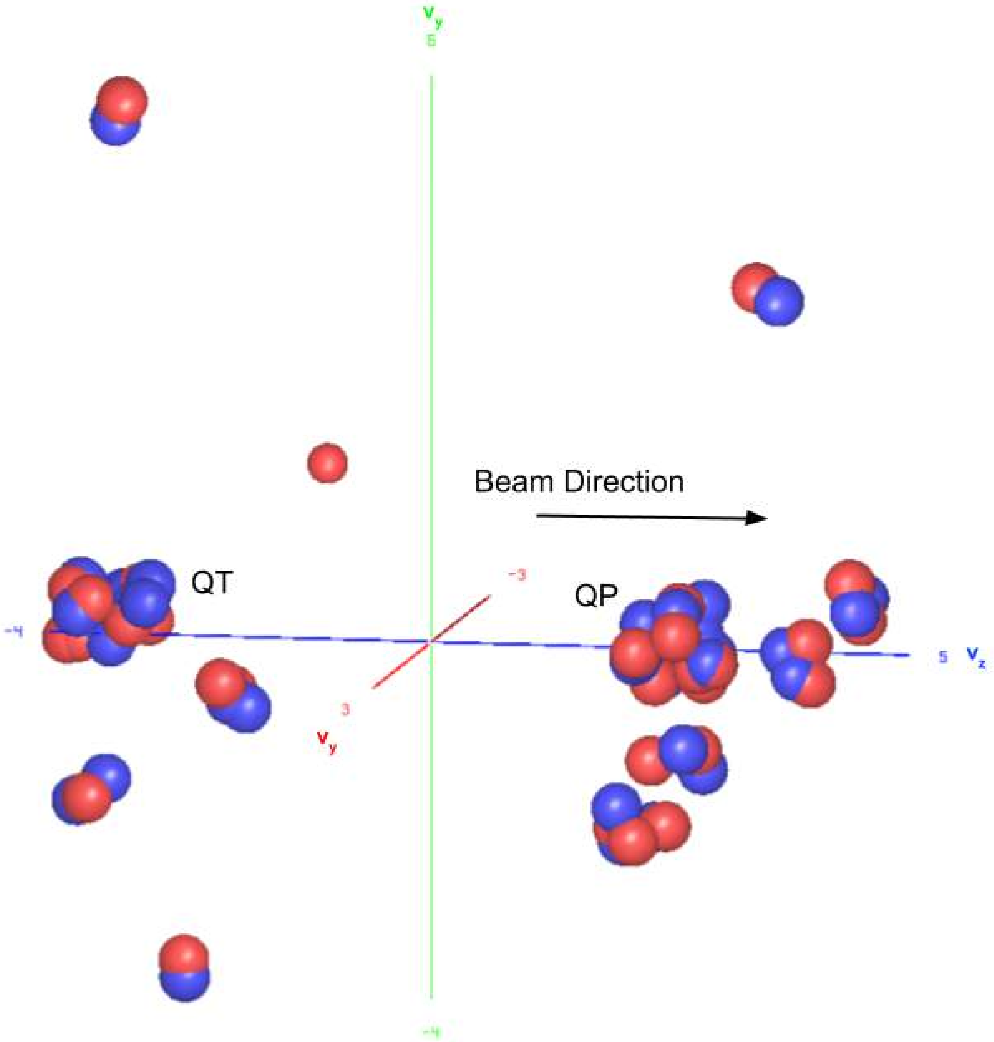

Fig. 4.4: 3-D visualisation of a primary collision from HIPSE simulation for ^{48}Ca+^{27}Al reaction at 40 MeV/A in the velocity space in CM frame at t ≈ 50 fm/c. The QT and QP are also marked.

The distribution of the excitation energy among the primary fragments is shown in Fig. 4.5(a) as a correlation between the fragment charge (Z) and excitation energy of fragments (E^*). It can be seen that the E^* is properly distributed among the fragments with the help of Eq.4.2. A detailed structure of the E^* distribution can be observed by splitting the primary fragments according to their emission sources (see Fig. 4.5(c)). These fragments may come from various emission sources like the excited QP or QT, compound-nucleus (CN) or other sources (Others) like pre-equilibrium emissions. The higher the E^* of the fragments, the faster is their de-excitation and they are more likely to decay into larger number of smaller fragments. The CN fragments appear to have the largest E^* and hence should decay faster and much more than fragments from all other sources. QP and QT fragments have E^* spread through a wider range and the ones with high E^* should undergo de-excitation. Most of the fragments from other sources like pre-equilibrium emissions are emitted at early stages of the reaction and reach their ground states quickly even before secondary decays. The LCPs mainly come from these emission sources. All these observations are also supported by the value of mean excitation energy ($\langle E^* \rangle$) for each emission source in Table 4.1.

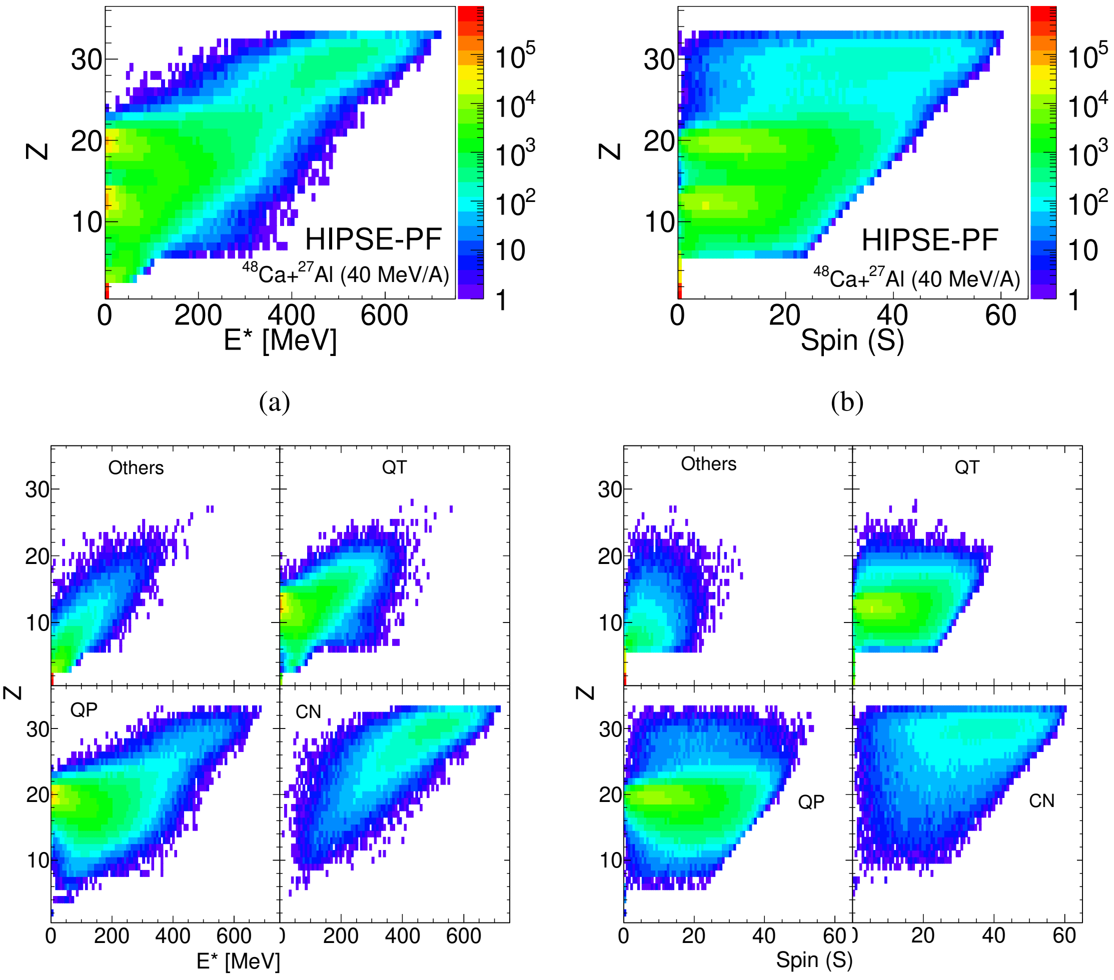

(a)

(b)

(c)

(d)

Fig. 4.5: (a): Fragment charge (Z) vs Excitation energy (E*) of primary fragments for ^{48}Ca+^{27}Al at 40 MeV/A. (b): Fragment charge (Z) vs spin angular momentum (S) for ^{48}Ca+^{27}Al at 40 MeV/A. (c): Z vs E* and (d): Z vs S, both split into contributions from various emission sources (Others, QT, QP and CN), respectively.

Similar observations can be made from the charge (Z) and spin angular momentum (S) correlation given in Fig. 4.5(b). The spin angular momentum is calculated from the output of the HIPSE primary fragment data file. It provides the s_x, s_y and s_z components and then the magnitude of spin angular momentum can be found using $S = \sqrt{s_x^2 + s_y^2 + s_z^2}$. The contributions of different emission sources are given in Fig. 4.5(d). Just like the E^* distributions, the heavier fragments have higher S. The heavier fragments corresponding to higher S will emit more smaller particles than the ones with low S. The LCPs and IMFs up to Z∼5 have negligible spin suggesting that these fragments have already reached ground states. This was also observed in E^* distributions. Similarly, QP and QT fragments have the S spread over a wide range. All these observations can be also confirmed from the mean values of spin ($\langle S \rangle$) given in Table 4.1.

	$\langle E^* \rangle$ [MeV/A]	$\langle S \rangle$
All	1.258 ± 0.001	7.492 ± 0.005
QP	1.701 ± 0.001	14.47 ± 0.008
QT	1.711 ± 0.002	9.601 ± 0.006
CN	6.854 ± 0.005	31.15 ± 0.047
Others	0.381 ± 0.001	0.16 ± 0.001

Table 4.1: Mean values of the total excitation energy of fragments $\langle E^* \rangle$ and spin angular momentum $\langle S \rangle$ of all fragments combined (All) and also for separate emission sources (QP, QT, CN and Others).

The data has been presented here as comparison between the primary collision fragments (HIPSE-PF) and the data from secondary de-excitation phase simulated by SIMON (HIPSE-SIMON) and GEMINI++ (HIPSE-GEMINI++) statistical decay codes. One can understand the transformation of the reaction system from primary fragments to secondary decay fragments from this comparison.

The total multiplicity M_{tot} of charged particles ($Z \geq 1$) is shown in Fig. 4.6 as a probability distribution. For HIPSE-PF (blue solid line), the value of M_{tot} does not go very high due to formation of larger clusters and heavier fragments that are in excited states. The formation of compound nucleus in this phase corresponds to the value of $M_{tot} = 1$. After the secondary decays, the excited clusters emit multiple fragments via multi-fragmentation, simultaneous fission, evaporation, etc. Then the multiplicities increase much more after the secondary decays as the total number of fragments per event increases. Both HIPSE-SIMON (solid black line) and HIPSE-GEMINI++ (dotted black line) data produce similar M_{tot} distributions. Also, there are no events with $M_{tot} = 1$ suggesting that all compound nuclear clusters should have decayed.

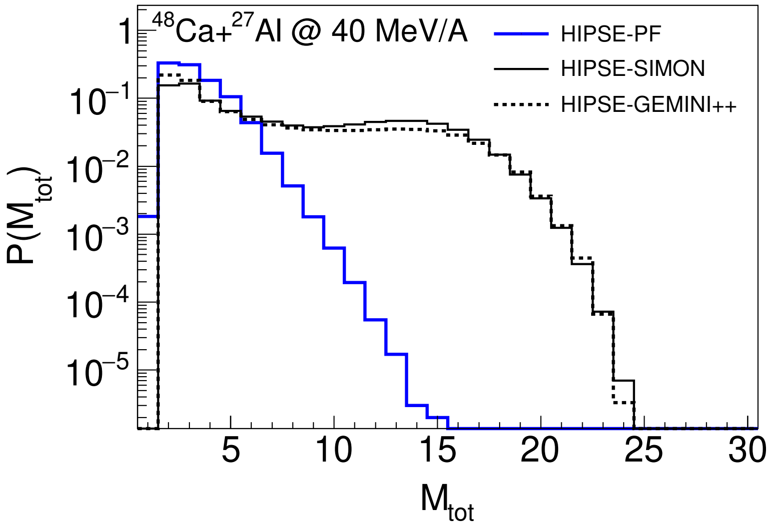

Fig. 4.6: Total multiplicity (M_{tot}) of charged particles ($Z \geq 1$) simulated by HIPSE for ^{48}Ca+^{27}Al at 40 MeV/A.

In the fragment charge (Z) probability distribution (Fig. 4.7), 3 peaks in HIPSE-PF , namely from QT (Z ~ 13), QP (Z ~ 20) and CN (Z ~ 30) can be observed. The CN peak is absent in HIPSE-SIMON and HIPSE-GEMINI++ confirming that CN fragments have undergone de-excitation producing lighter fragments (mostly light-charged particles (LCPs) and intermediate-mass fragments (IMFs)). As a result, an increase in overall statistics in HIPSE-SIMON and HIPSE-GEMINI++ for LCPs and IMFs can be observed. The QP and QT yields for secondary fragments slightly decrease probably due to some emissions of lighter fragments from excited clusters.

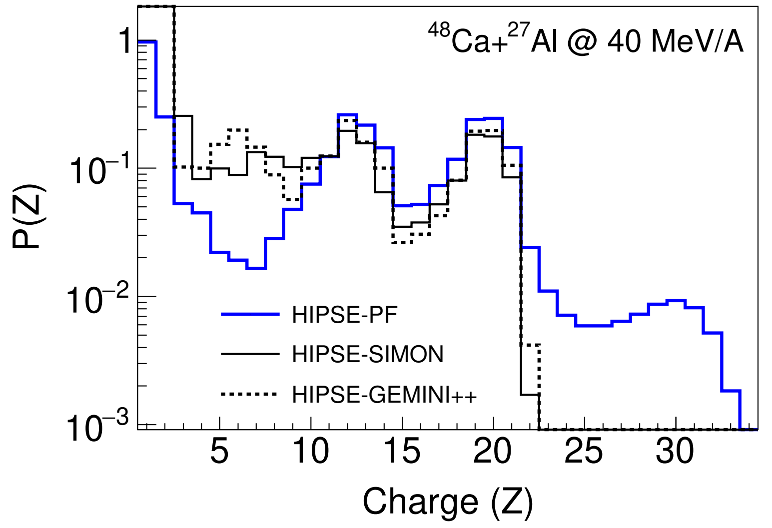

Fig. 4.7: Fragment charge (Z) simulated by HIPSE for ^{48}Ca+^{27}Al at 40 MeV/A.

Looking at the fragment mass (A) in Fig. 4.8, the same peaks can be observed for QT

(A ~ 27), QP (A ~ 48) and CN (A ~ 70). There are similar trends in A distribution like in Z distribution except a few points. There is a sudden drop of statistics at A=8 corresponds to the break-up of the ^{8}Be into two ^{4}He. Also, in HIPSE-GEMINI++ there are no particles for A=5, i.e. there is no ^{5}He, which is correctly produced because ^{5}He has extremely short life-time ($\approx 10^{-22}$ s). HIPSE-SIMON produces some ^{5}He but the reason might be the time period provided in the simulations for the secondary fragments to propagate in the phase space. The ^{5}He nucleus being a meta-stable state might be present in the data if the afterburner time period was short (few hundred fm/c).

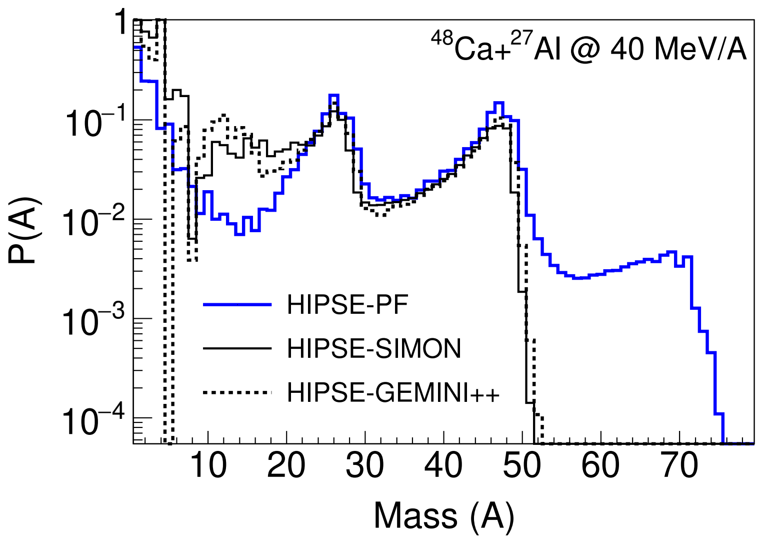

Fig. 4.8: Fragment charge (Z) simulated by HIPSE for ^{48}Ca+^{27}Al at 40 MeV/A.

The mean values of the basic reaction observables for ^{48}Ca+^{27}Al (40 MeV/A) system previously discussed are given in Table 4.2 for the primary HIPSE-PF and secondary HIPSE-SIMON and HIPSE-GEMINI++ fragments.

Observables	HIPSE-PF	HIPSE-SIMON	HIPSE-GEMINI++
$\langle Z \rangle$	10.019 ± 0.004	4.371 ± 0.002	4.875 ± 0.003
$\langle A \rangle$	22.409 ± 0.010	9.316 ± 0.005	10.326 ± 0.007
$\langle M_{tot} \rangle$	3.294 ± 0.001	7.549 ± 0.005	6.769 ± 0.006

Table 4.2: Mean values of all the basic important reaction observables for ^{48}Ca+^{27}Al (40 MeV/A) system, namely, mass (A), charge (Z) and total charged particle multiplicity (M_{tot}) produced by HIPSE simulations.

For the mean values of Z and A, the HIPSE-PF has higher values than the secondary fragments suggesting the presence of heavier fragments. These values become lesser for secondary fragments because the heavier fragments decay into smaller ones. HIPSE-SIMON and HIPSE-GEMINI++ have similar mean values for Z and A. The $\langle M_{tot} \rangle$ supports the previous observation that HIPSE-PF has lower multiplicities due to heavy excited clusters. These clusters decay into smaller fragments and increase the $\langle M_{tot} \rangle$ of secondary fragments.

Also, the multiplicities of protons (M_p), deuterons (M_d), tritons (M_t), helium-3 ($M_{^3He}$) and alphas ($M_{^4He}$) are given in Table 4.3. It can be said that after secondary decays, the proton and alpha production greatly increases as compared to deuteron, triton and ^{3}He.

Observables	HIPSE-PF	HIPSE-SIMON	HIPSE-GEMINI++
$\langle M_p \rangle$	1.519 ± 0.001	2.489 ± 0.002	2.957 ± 0.003
$\langle M_d \rangle$	1.133 ± 0.001	1.831 ± 0.002	1.560 ± 0.002
$\langle M_t \rangle$	1.115 ± 0.001	1.449 ± 0.001	1.285 ± 0.002
$\langle M_{^3He} \rangle$	1.046 ± 0.001	1.185 ± 0.001	1.060 ± 0.001
$\langle M_{^4He} \rangle$	1.044 ± 0.001	3.182 ± 0.002	3.411 ± 0.004

Table 4.3: Mean values of proton multiplicity (M_p), deuteron multiplicity (M_d), triton multiplicity (M_t), helium-3 multiplicity ($M_{^3He}$) and alpha multiplicity ($M_{^4He}$) for ^{48}Ca+^{27}Al (40 MeV/A) system produced by HIPSE simulations.

Using the Z and A values, the number of neutrons (N) were calculated directly from $N = A - Z$ to observe the Z and N correlation shown in Fig. 4.9. Z vs N nuclear chart was superimposed on the correlation matrix using the KVNuclearChart class from the KaliVeda toolkit (discussed earlier in Chapter 2) so as to identify the isotopic content of fragments formed in HIPSE-PF and later from the secondary decay codes in HIPSE-SIMON and HIPSE-GEMINI++. The N value is an important observable to calculate and compare the N/Z of the fragments from HIPSE with the FAZIA-PRE experimental data to understand the evolution of isospin transport within the HIPSE frameworks. This will help to verify whether HIPSE can reproduce isospin effects in nuclear reactions at intermediate energies with varying N/Z.

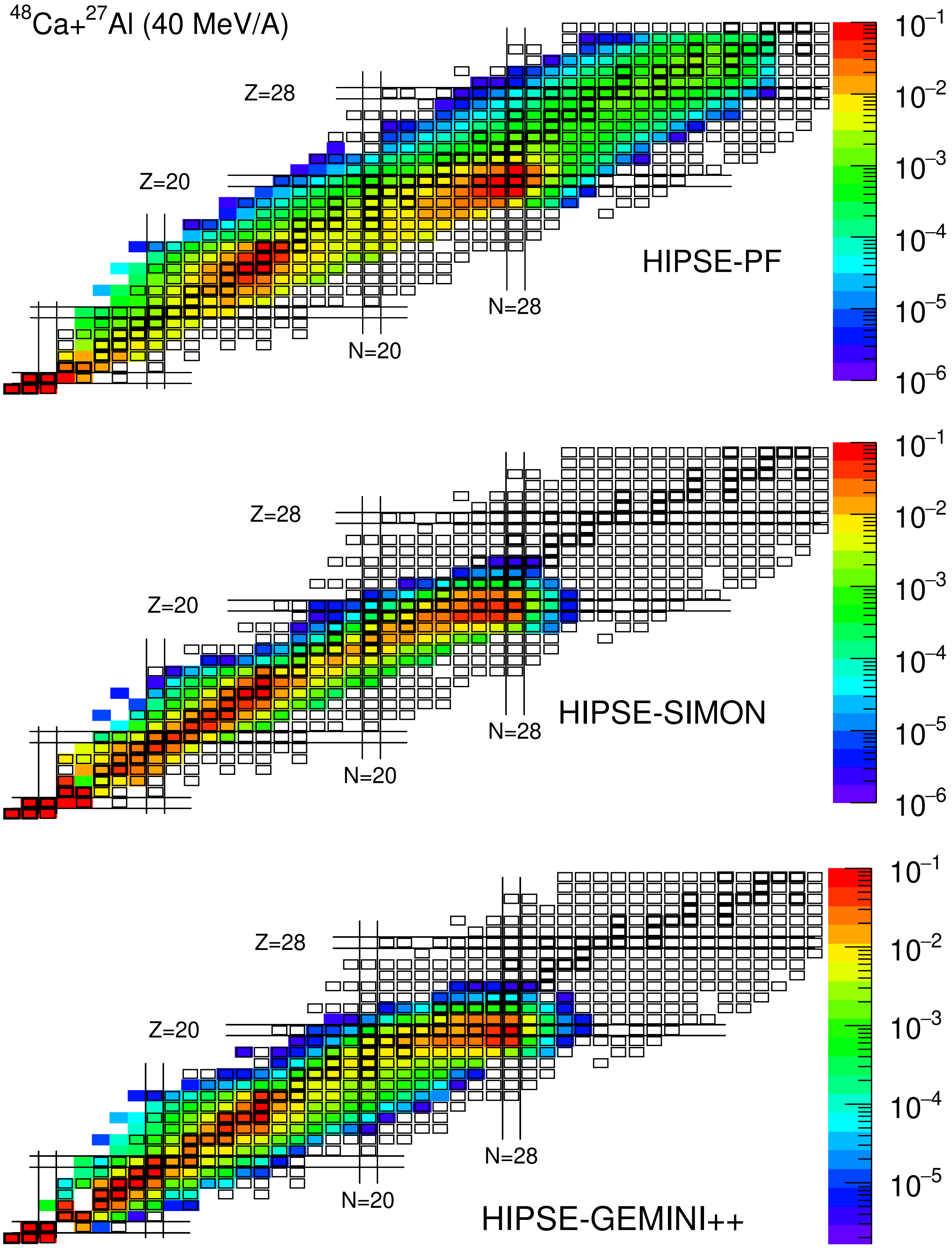

Fig. 4.9: Fragment charge (Z) vs neutron number (N) correlation for primary (HIPSE-PF) and secondary (HIPSE-SIMON and HIPSE-GEMINI++) fragments for ^{48}Ca+^{27}Al at 40 MeV/A.

Just to recall, the maximum value of the impact parameter (b_{max}) for the chosen system was 8 fm so that the ultra-peripheral region is avoided due to unavailability of sufficient energy for QT and QP production. Plotting the fragment charge (Z) as a function of the impact parameter (*b*) (Fig. 4.10) it can be seen that in HIPSE-PF (left-panel), the CN dominates at more central collisions and the QP and QT are produced at peripheral/semi-peripheral collisions. The HIPSE-SIMON (middle-panel) and HIPSE-GEMINI++ (right-panel) produce similar results.

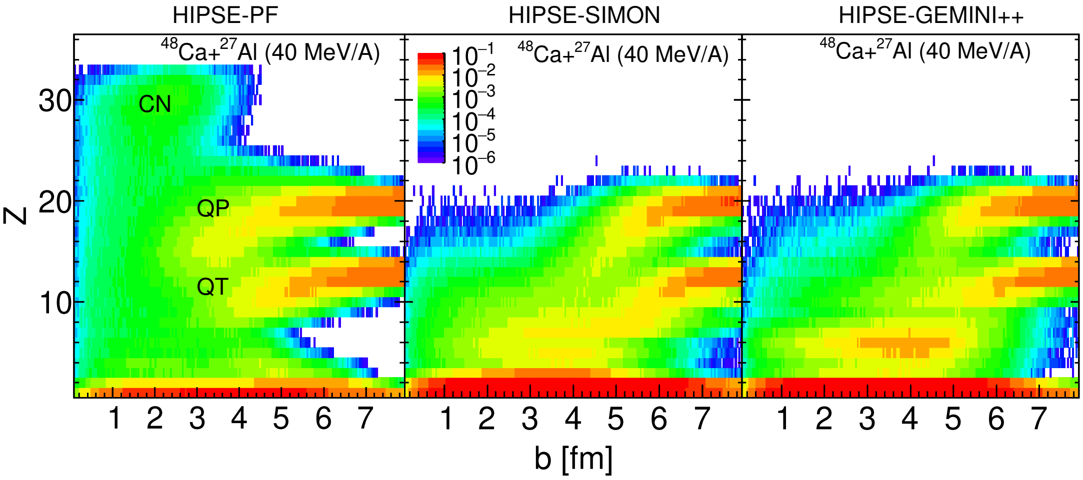

Fig. 4.10: Fragment charge (*Z*) vs impact parameter (*b*) for ^{48}Ca+^{27}Al at 40 MeV/A. The QP, QT and CN are marked in left panel.

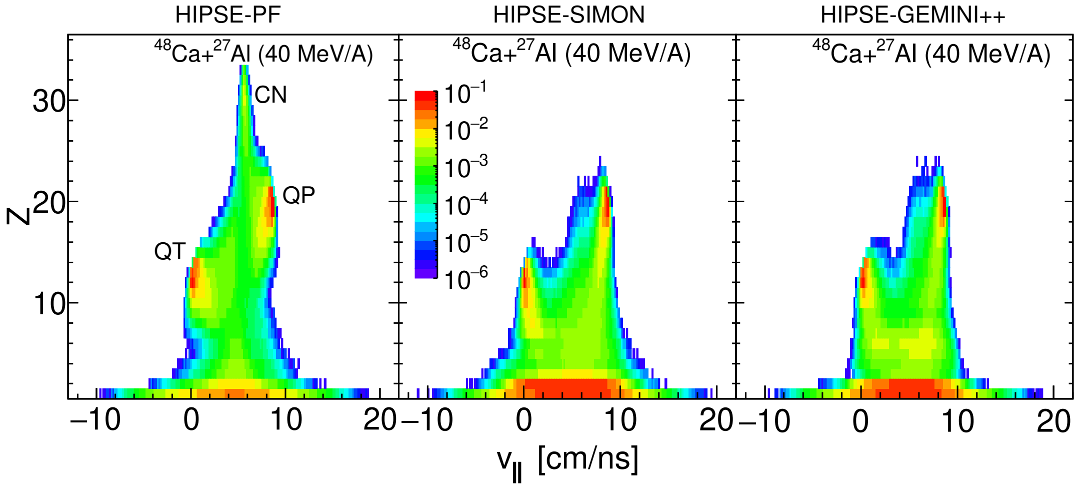

Fig. 4.11: Fragment charge (*Z*) vs longitudinal velocity ($v_{\|}$) for ^{48}Ca+^{27}Al at 40 MeV/A. The QP, QT and CN are marked.

The charge (Z) vs longitudinal velocity ($v_{\|}$) distribution is shown in Fig. 4.11. The $v_{\|}$ is boosted in the laboratory frame. The QT, QP and CN regions are marked in the panels. The target has zero longitudinal velocity and it spreads mostly in the transverse plane after interaction with the projectile. So, the QT has $v_{||} \approx 0$ cm/ns. The projectile velocity for $E_B = 40$ MeV/A is around 8.5 cm/ns and the QP is observed in the similar range of $v_{||}$ in the simulation results. Also, the CN fragments in HIPSE-PF lie around the centre-of-mass velocity. For the secondary fragments, it is seen that the de-excited QT and QP are remaining and the CN has decayed into smaller fragments. From these results, the energy or momentum of the fragments can be easily calculated.

After this, the next step is to compare HIPSE with the FAZIA-PRE experimental data. But these results cannot be compared directly. HIPSE raw data is for a full 4π distribution and the FAZIA-PRE setup had a forward acceptance limited to small angles. So, the HIPSE data has to be filtered according to the experimental constraints, i.e. geometry, energy thresholds, etc.

4.4 Filtering HIPSE data

The experimental arrangement of the FAZIA detector in the FAZIA-PRE experiment (discussed in Chapter 2) had an acceptance of very forward angles ($\sim 2° - 16°$). To compare it with the HIPSE data, the experimental constraints are put accordingly on the HIPSE simulations. This is done by filtering the simulations in the KaliVeda frameworks. KaliVeda has an interface called "kaliveda-sim" that is used to read HIPSE data files. The full 4π data is loaded into the interface which then applies the experimental constraints on the simulations and provides the filtered data files. A snapshot of the kaliveda-sim interface with available filtering options is shown in Fig. 4.12.

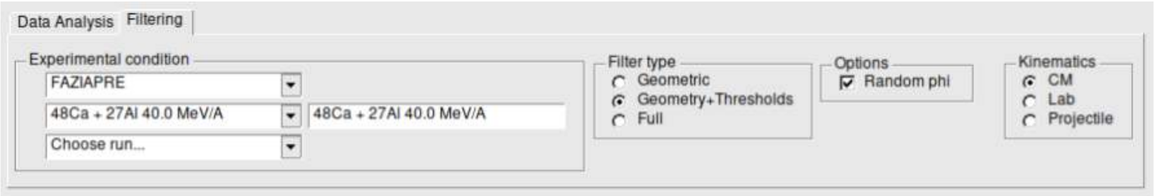

Experimental condition
FAZIAPRE
48Ca + 27Al 40.0 MeV/A
48Ca + 27Al 40.0 MeV/A
Choose run...

Filter type
○ Geometric
● Geometry+Thresholds
○ Full

Options
☑ Random phi

Kinematics
● CM
○ Lab
○ Projectile

Fig. 4.12: Snapshot of kaliveda-sim interface of KaliVeda toolkit.

To have an idea about the output of the filtered data, only the results from ^{48}Ca+^{27}Al system at 40 MeV/A for HIPSE-SIMON are presented (HIPSE-GEMINI++ had similar results for the filtered data so it was not necessary to show them here). The fragment charge (Z) distribution presented in Fig. 4.13(a) shows the comparison between filtered (black solid line) and unfiltered (blue solid line) data from HIPSE-SIMON.

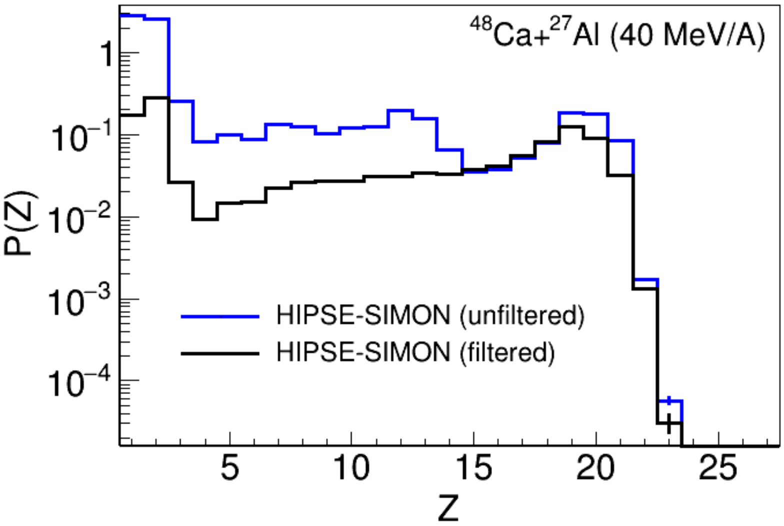

(a)

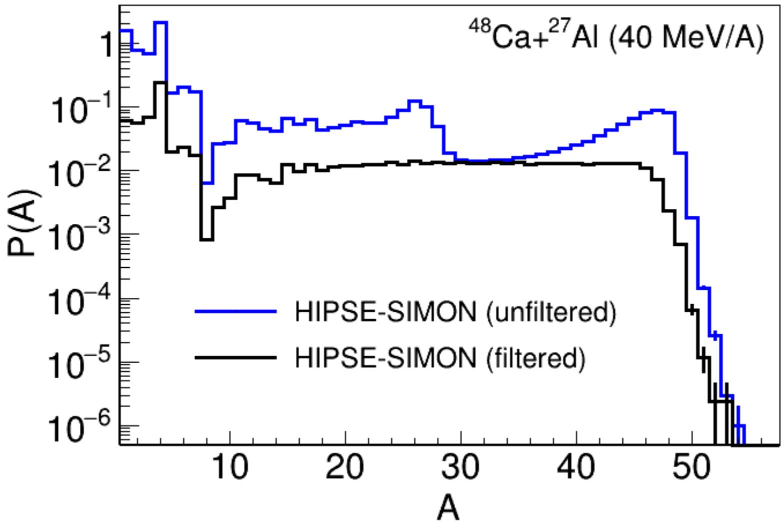

(b)

Fig. 4.13: Comparison of filtered (black solid line) with unfiltered (blue solid line) simulations from HIPSE-SIMON for ^{48}Ca+^{27}Al (40 MeV/A) system. (a): Fragment charge (Z) distribution. (b): Fragment mass (A) distribution.

It can be observed that the filtered data has the quasi-projectile (QP) peak around Z~20. This is due to the detection of mostly QP fragments in the forward acceptance angles of FAZIA detector in the experiment. The QT is not measured because it stays mostly in the transverse plane (perpendicular to both reaction and longitudinal planes) and cannot reach the detector. A similar trend in the fragment mass (A) distribution is observed from Fig. 4.13(b). But for higher masses, the distribution has a slight disagreement. This is due to the fact that the filtering algorithm tries to replicate the A identification capabilities of the FAZIA detector with a limitation up to Z ≈ 20. As the projectile has Z, A = 20, 48, the QP is not produced fully at this point. But the fragments in QP region are still produced with an appropriate velocity distribution. This can be observed by comparing Fig. 4.14 (a) and (b), that only the QP is present after the filter and with the correct longitudinal velocity in the laboratory frame. Clearly there is no detection for QT part. Effectively, only about 40% of the total fragment distribution gets accepted after applying the filter.

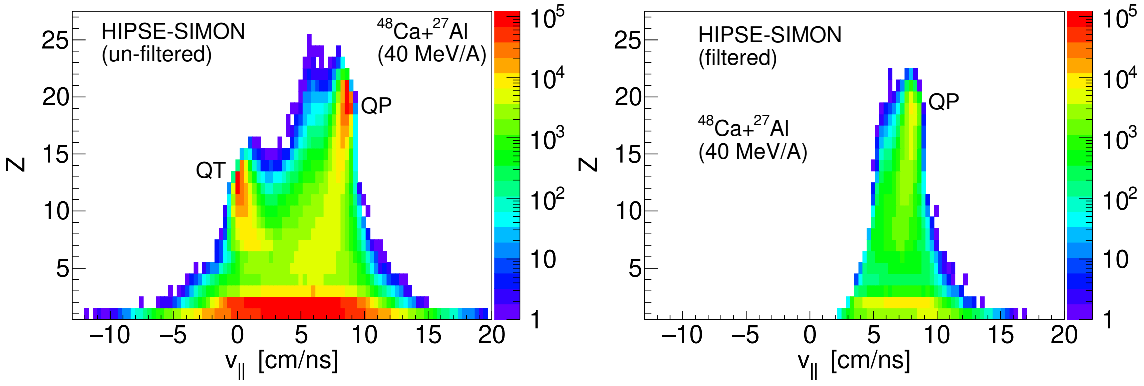

(a) (b)

Fig. 4.14: Fragment charge (Z) vs longitudinal velocity ($v_{||}$) distribution for ^{48}Ca+^{27}Al (40 MeV/A) system. (a): Unfiltered HIPSE-SIMON simulations. (b): Filtered HIPSE-SIMON simulations.

These comparisons give an overall idea of the data produced by the filtered simulations generated using KaliVeda. This filtration of the simulated data has been done for all the five systems of the FAZIA-PRE experiment. In further sections, the direct comparison of filtered HIPSE simulations with the FAZIA-PRE experimental data is shown. But before the direct comparison, it is important to have a systematic comparison of the filtered HIPSE data for all the systems with respect to the target mass and beam energy.

4.5 Systematic comparison of filtered HIPSE data

In this section, the HIPSE data is presented in a similar way like the FAZIA-PRE data was compared systematically in Chapter 3. Comparison of HIPSE data is presented in two sub-sections, for basic reaction observables and for fragment isospin effects for both HIPSE-SIMON and HIPSE-GEMINI++. Both the sub-sections have data comparison with respect to (w.r.t.) the target mass and beam energy. The results from these comparisons are shown to observe the behaviour of the data and verify whether the corresponding physical phenomena are present in the HIPSE model calculations.

4.5.1 Comparison for basic reaction observables

With respect to target mass

The fragment charge (Z) distribution for HIPSE-SIMON and HIPSE-GEMINI++ with respect to the target mass are shown in Fig. 4.15(a) and (b) and Fig. 4.16(a) and (b), respectively. Solid circles and solid triangles represent the 25 and 40 MeV/A beam energies and black, red and blue colours represent the ^{12}C, ^{27}Al and ^{40}Ca targets, respectively. It can be seen that there is no significant target dependence in relative yields of the LCPs for both afterburners and both beam energies. For 25 MeV/A systems, the relative fragment yield increases with target mass for IMFs and decreases with target mass for heavier fragments. Then at the projectile Z value (= 20), the relative yield again increases with target mass. A slight change in the pattern of HIPSE-GEMINI++ is observed with ^{27}Al target. For 40 MeV/A systems, most of the fragments have decreasing relative probability with increasing target mass. But around projectile Z, the trend becomes opposite. In comparison to trends from the experimental data, the target dependence observed in HIPSE for Z distribution is similar for $Z \geq 7$.

The fragment mass (A) distribution from HIPSE-SIMON and HIPSE-GEMINI++ is given in Fig. 4.15(c) and (d) and Fig. 4.16(c) and (d) for 25 and 40 MeV/A beam energies, respectively. The target dependence on A distribution is not very significant for $A \lesssim 15$. For 25 MeV/A systems, the relative probability distribution for $A \gtrsim 15$ to $A \lesssim 40$ first increases and then decreases with increasing target mass. In 40 MeV/A systems, the relative probability is higher for lower target mass. Above A=40, it is not very reliable to compare the effect of target mass because of improper mass distribution generated by the filter while replicating the identification limits of FAZIA. Also, staggering is observed in HIPSE-GEMINI++ A distribution except for ^{27}Al data from 40 MeV/A. Moreover, in comparison with the trends from experimental data, the A distribution has mostly similar behaviour.

Now, the M_{tot} distribution for HIPSE-SIMON and HIPSE-GEMINI++ is shown in Fig. 4.15(e) and (f) and Fig. 4.16(e) and (f) for 25 and 40 MeV/A beam energies, respectively. In 25 MeV/A systems, for M_{tot} = 1, there is no significant difference. For higher M_{tot} values, HIPSE-SIMON has decreasing relative probability with increasing target mass, but HIPSE-GEMINI++ is completely different. For 40 MeV/A systems, the M_{tot} trends are similar to the experimental data where ^{27}Al has higher relative probability at M_{tot} = 1 and then decreases for higher M_{tot} values. The reason for this trend was explained in Chapter 3 that ^{27}Al has lowest separation energies for protons and neutrons among all other targets used here which leads to emission of more and more fragments in all directions before reaching the detector, and hence, decreasing the relative yield. With all these observations for basic reaction observables, it can be said that the dependence on the target mass within HIPSE data is present to a certain reasonable level.

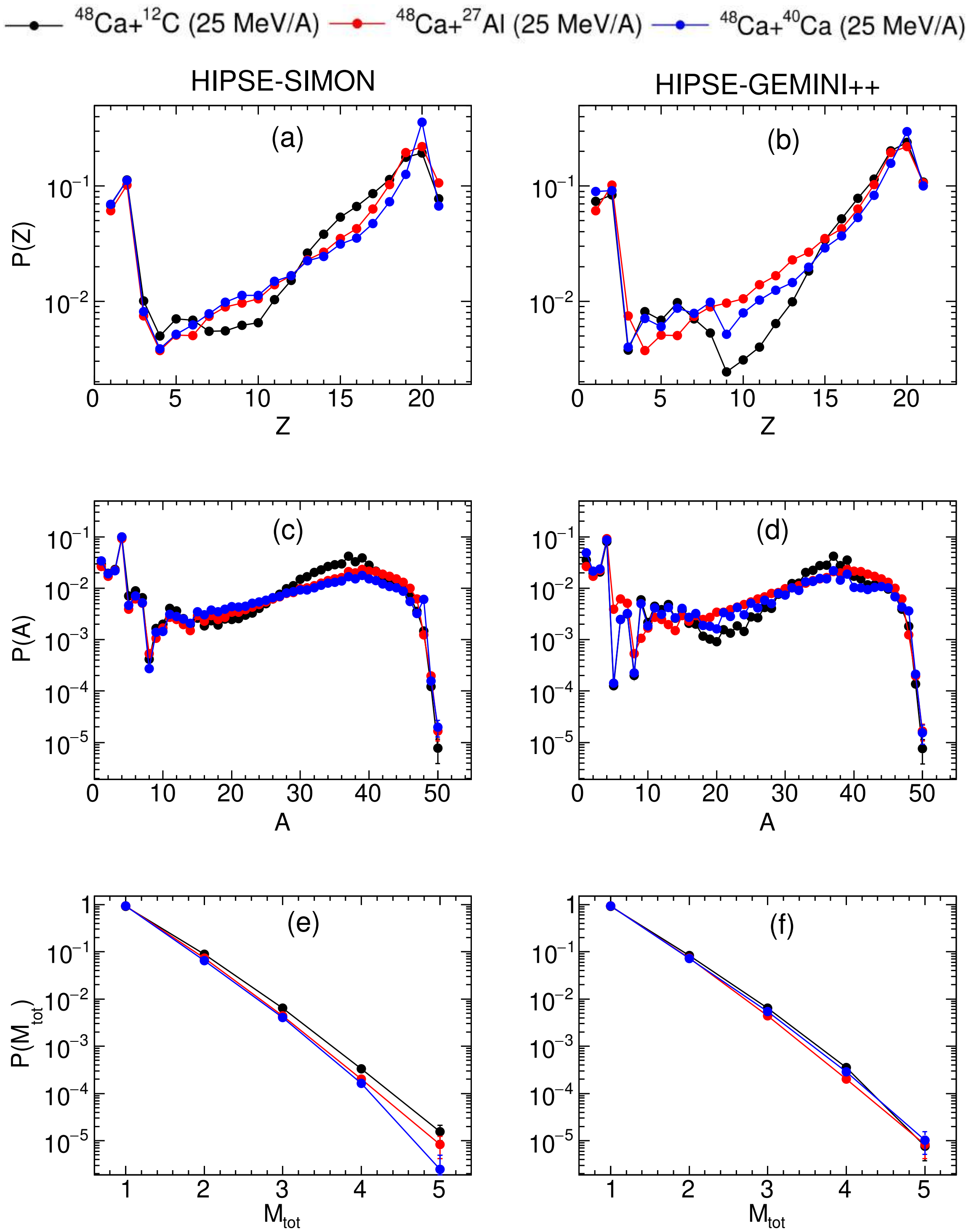

Fig. 4.15: Comparison of HIPSE data for 25 MeV/A systems w.r.t. target mass. Left column represents (a): Z ; (c): A ; (e): M_{tot} distributions from HIPSE-SIMON. Right column represents (b): Z ; (d): A ; (f): M_{tot} distributions from HIPSE-GEMINI++.

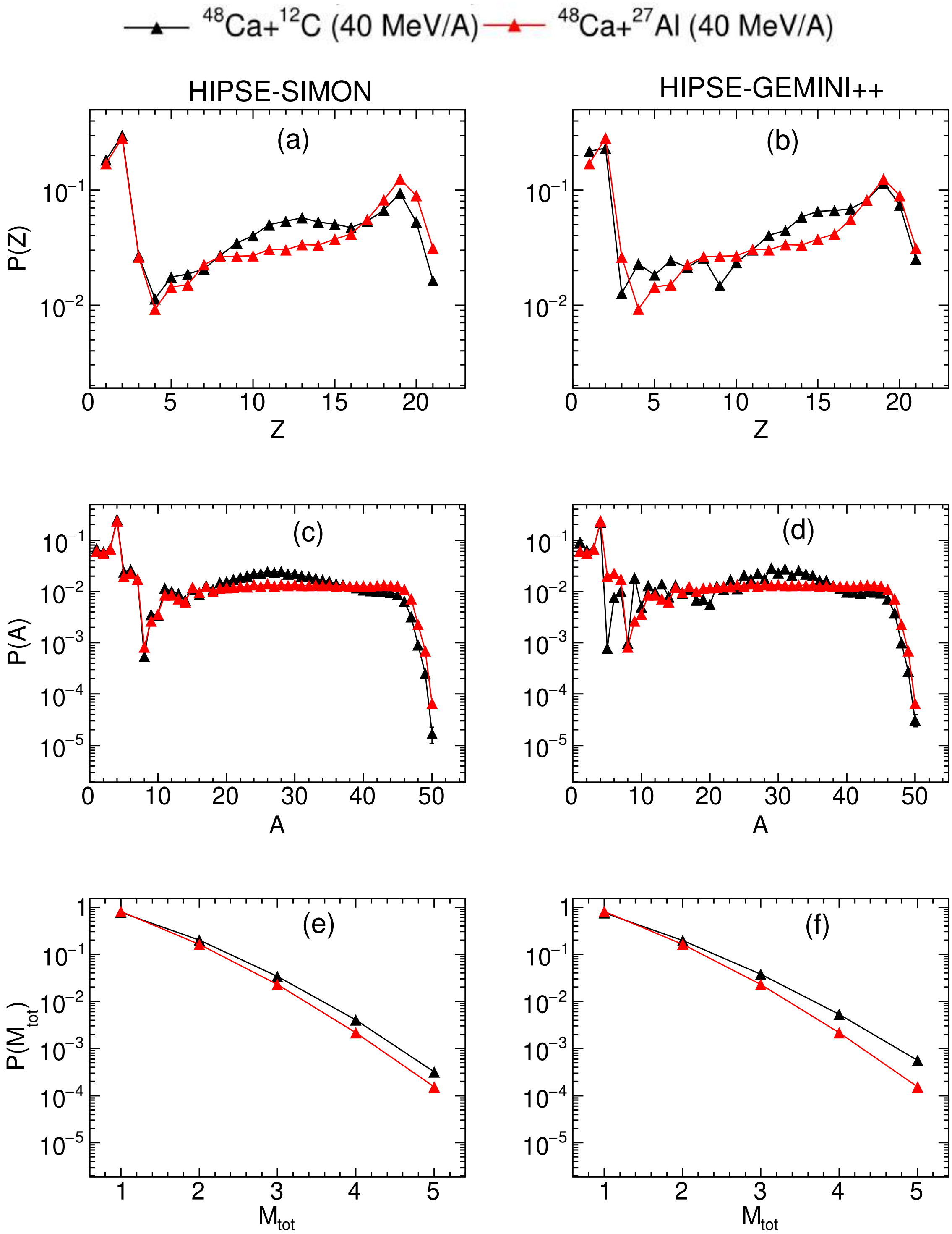

Fig. 4.16: Comparison of HIPSE data for 40 MeV/A systems w.r.t. target mass. Left column represents (a): Z ; (c): A ; (e): M_{tot} distributions from HIPSE-SIMON. Right column represents (b): Z ; (d): A ; (f): M_{tot} distributions from HIPSE-GEMINI++.

With respect to beam energy ($\mathbf{E_B}$)

The comparison of the HIPSE data w.r.t. beam energy, i.e., E_B = 25 and 40 MeV/A for ^{48}Ca+^{12}C and ^{48}Ca+^{27}Al reactions is shown in Fig. 4.17 and Fig. 4.18, respectively. This comparison cannot be shown for ^{48}Ca+^{40}Ca because the data of this system was not available for 40 MeV/A beam energy.

Starting with the Z distribution, shown in Fig. 4.17(a) and (b) and Fig. 4.18(a) and (b), it is observed that the heavier fragments (Z>15) from higher E_B systems break into smaller ones on a greater scale than those at lower E_B. This leads to lesser relative yield of heavy fragments at higher E_B. For the same reason, the fragments with Z<16 have higher relative yield confirming that the systems at higher E_B have dominance of multi-fragmentation.

The A distribution given in Fig. 4.17(c) and (d) and Fig. 4.18(c) and (d) also has similar trends to Z distribution for heavier fragments as well as IMFs and LCPs. The fall in statistics appear for ^{8}Be in all data but for ^{5}He there the dip is present only in ^{48}Ca+^{12}C and ^{48}Ca+^{27}Al at 25 MeV/A (Fig. 4.17(d) and Fig. 4.18(d)).

For the M_{tot} distribution given in Fig. 4.17(e) and (f) and Fig. 4.18(e) and (f), the systems at higher E_B have similar relative probability for M_{tot} = 1 but it increases for higher M_{tot} values as there is increased fragmentation in each interaction event.

In general, the trends observed in Z, A and M_{tot} distributions w.r.t. beam energy are reasonably similar to that of the experimental data.

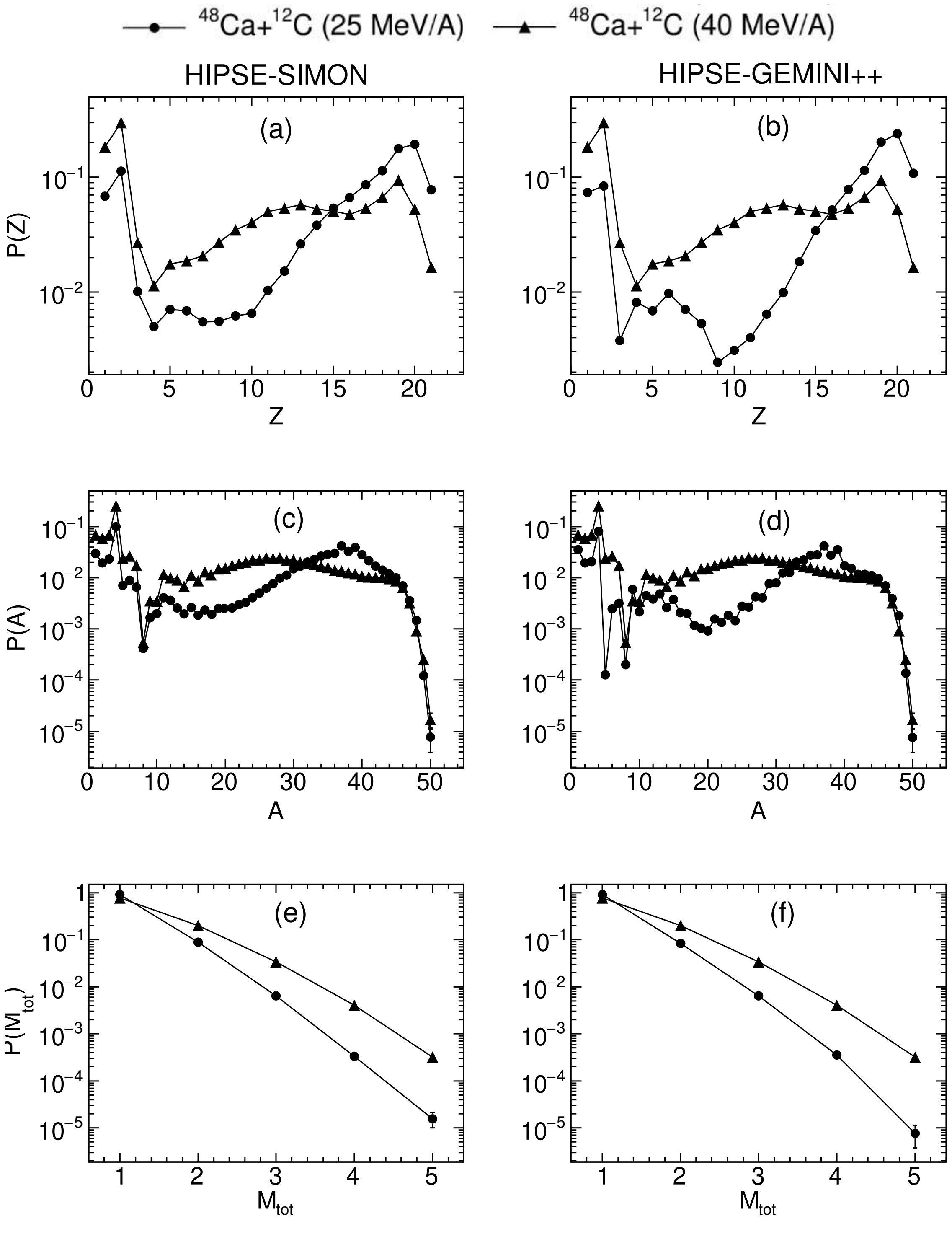

Fig. 4.17: Comparison of HIPSE data for ^{48}Ca+^{12}C system w.r.t. beam energy E_B. Left column represents (a): Z ; (c): A ; (e): M_{tot} distributions from HIPSE-SIMON. Right column represents (b): Z ; (d): A ; (f): M_{tot} distributions from HIPSE-GEMINI++.

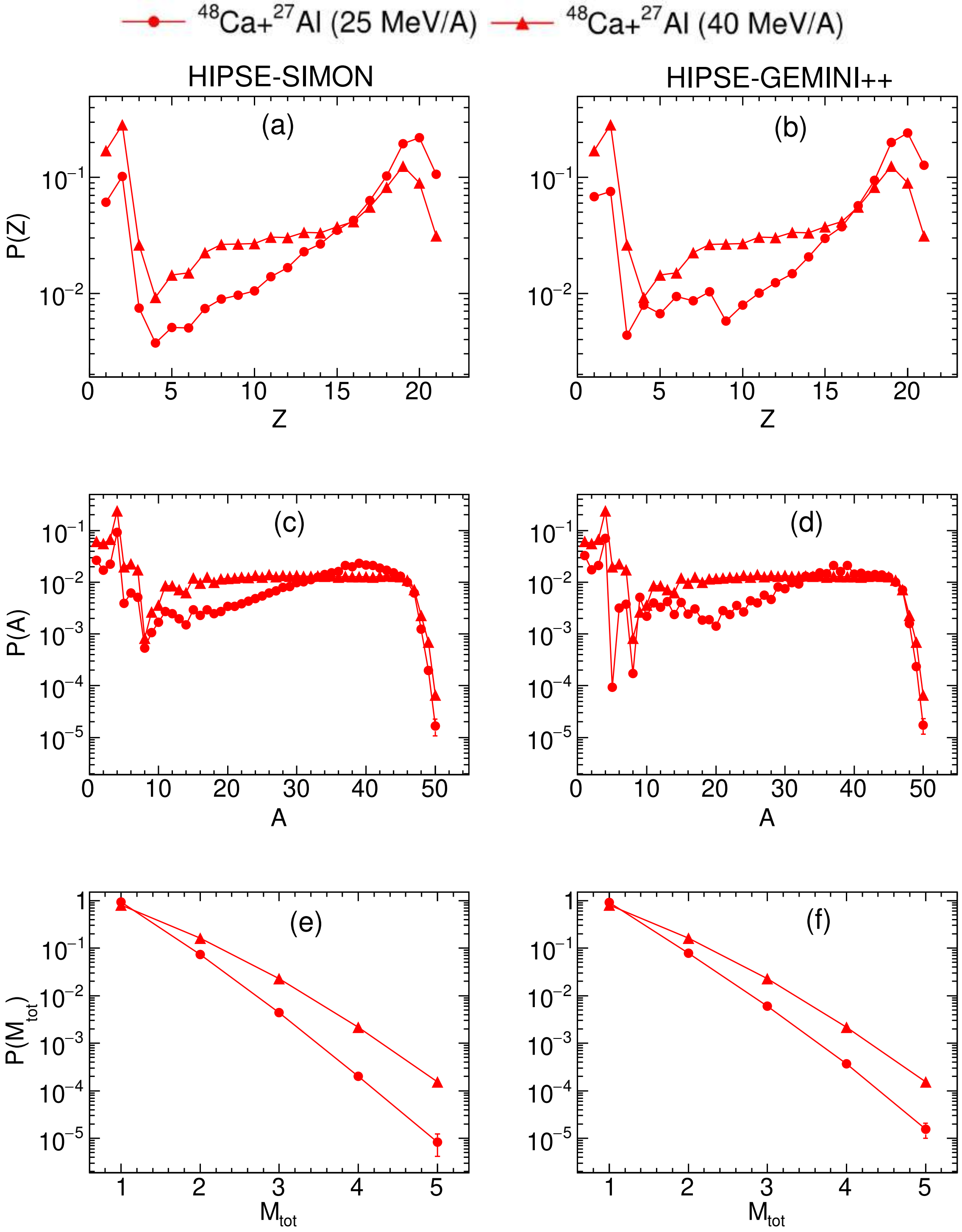

Fig. 4.18: Comparison of HIPSE data for ^{48}Ca+^{27}Al system w.r.t. beam energy E_B. Left column represents (a): Z ; (c): A ; (e): M_{tot} distributions from HIPSE-SIMON. Right column represents (b): Z ; (d): A ; (f): M_{tot} distributions from HIPSE-GEMINI++.

4.5.2 Comparison for isospin effects

Just to recall, one of the main reasons to choose the HIPSE model for comparison with FAZIA-PRE experimental data was to check the consistency for isospin (N/Z) effects on reaction products. Proceeding in a similar systematic way like it was done with the experimental data, it is essential to check the dependence of these N/Z effects in HIPSE w.r.t. target mass or beam energy, E_B.

With respect to target mass

Similar procedure taken from [83] which was also used in Chapter 3 for isospin studies has been adapted here. The N distributions were used to get the ⟨N⟩/Z vs Z correlation for Z>2 fragments, shown in Fig. 4.19 w.r.t. target mass for HIPSE-SIMON and HIPSE-GEMINI++. For HIPSE-SIMON data in Fig. 4.19(a) and (c), the heavier fragments near the projectile Z (= 20), the fragment ⟨N⟩/Z is high. This corresponds to the fact that the QP fragments detected at very forward angles come from the neutron projectile (^{48}Ca).

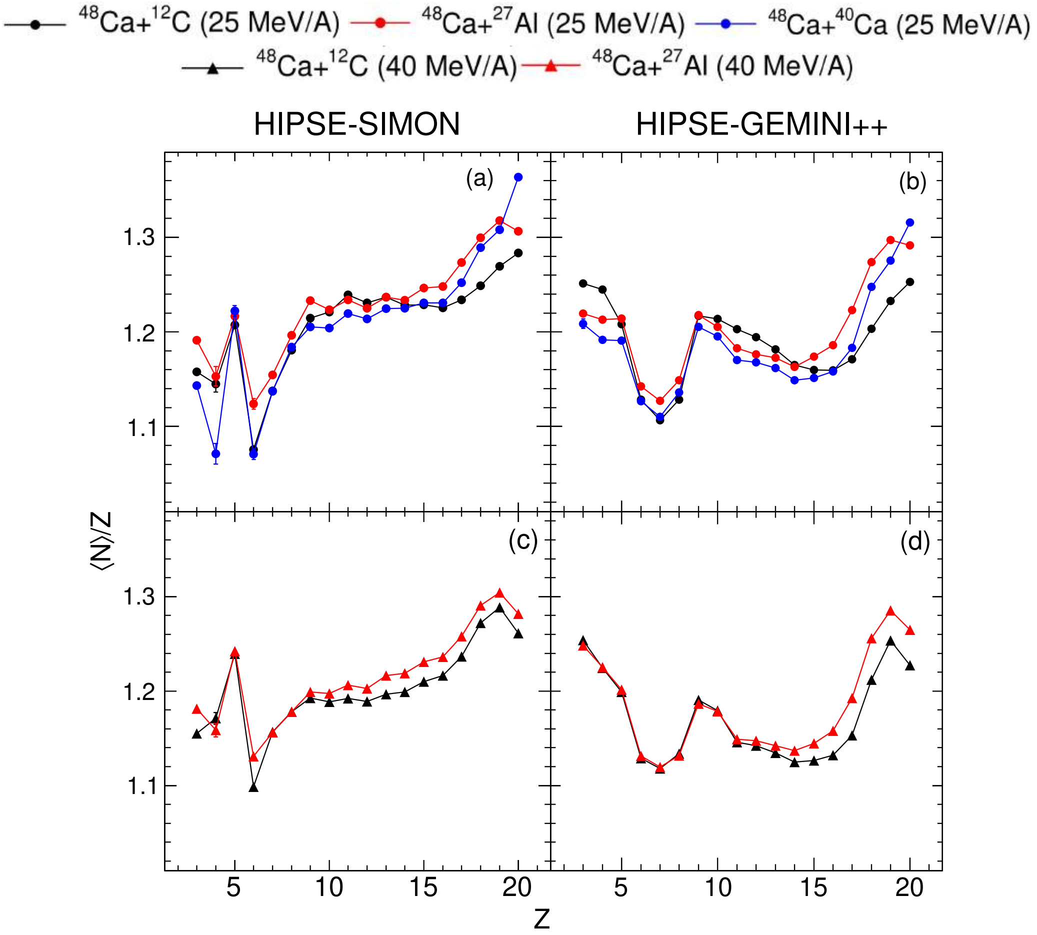

Fig. 4.19: ⟨N⟩/Z and Z correlation from HIPSE data w.r.t. the target mass. E_B = 25 MeV/A systems from (a): HIPSE-SIMON data ; (b): HIPSE-GEMINI++ data. E_B = 40 MeV/A systems from (c): HIPSE-SIMON data ; (d): HIPSE-GEMINI++ data.

The N/Z values of all systems and individual projectile and all targets were already given in Table 2.1. The lighter fragments (Z<10) have comparatively low ⟨N⟩/Z. For HIPSE-GEMINI++ data in Fig. 4.19(b) and (d), fragment ⟨N⟩/Z is again higher for heavier fragments due to the neutron rich projectile. But here, the lighter fragments (Z = 3, 4, 5) also have higher ⟨N⟩/Z than other IMFs. From these correlations, the target dependence on fragment ⟨N⟩/Z is not very substantial. Recalling the experimental observations, the fragment ⟨N⟩/Z trends w.r.t. target mass in HIPSE data do not agree with the experiment.

With respect to beam energy (E_B)

The ⟨N⟩/Z vs Z correlation w.r.t. E_B is shown in Fig. 4.20 for both HIPSE-SIMON and HIPSE-GEMINI++. The fragment ⟨N⟩/Z for higher E_B (here 40 MeV/A) seems mostly to be lower than the fragment ⟨N⟩/Z for lower E_B. To verify this, the difference between fragment ⟨N⟩/Z for both E_B ($\delta_E\langle N\rangle/Z = \langle N\rangle/Z_{25} - \langle N\rangle/Z_{40}$) as a function of Z is presented

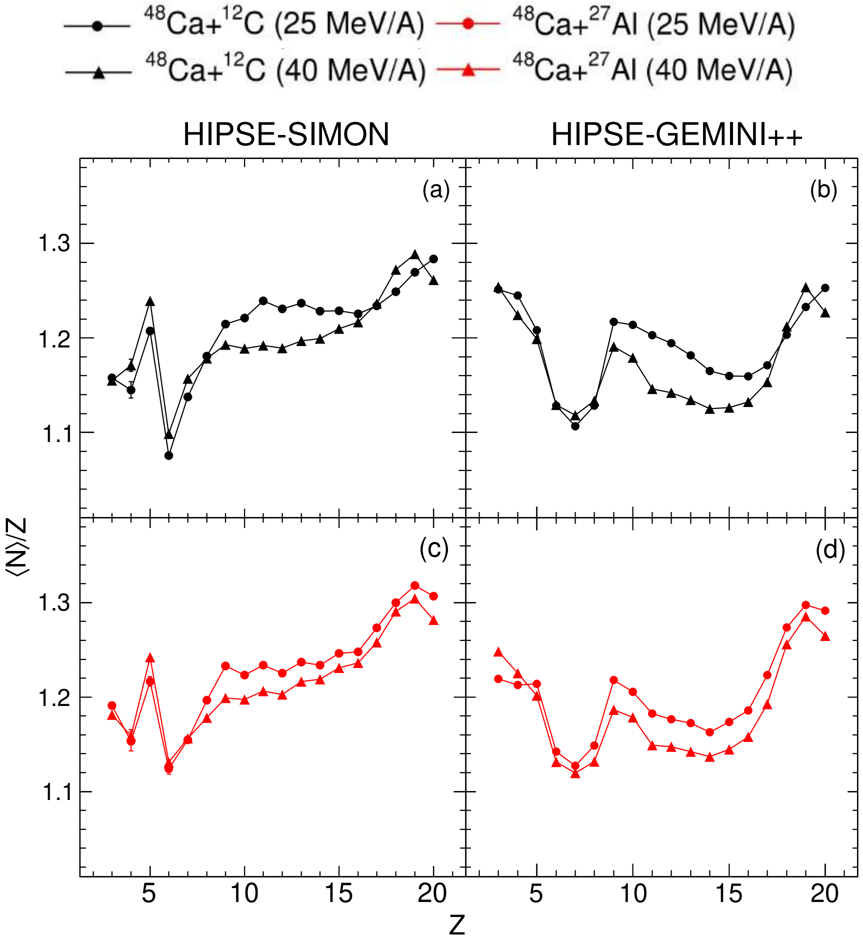

Fig. 4.20: ⟨N⟩/Z and Z correlation from HIPSE data w.r.t. the beam energy E_B. ^{48}Ca+^{12}C system from (a): HIPSE-SIMON data ; (b): HIPSE-GEMINI++ data. ^{48}Ca+^{27}Al system from (c): HIPSE-SIMON data ; (d): HIPSE-GEMINI++ data.

in Fig. 4.21. It can be seen that the value of $\delta_E\langle N\rangle/Z$ is positive for majority of the Z values indicating that fragment ⟨N⟩/Z is lower for higher E_B. This correlated to the fact that the pre-equilibrium emission of neutrons from the neutron rich projectile decreases the overall system ⟨N⟩/Z. For higher energy, there is more pre-equilibrium neutron emission which leads to lower ⟨N⟩/Z of reaction products. This can be considered to be in a reasonable agreement with the experimental observations for fragment ⟨N⟩/Z.

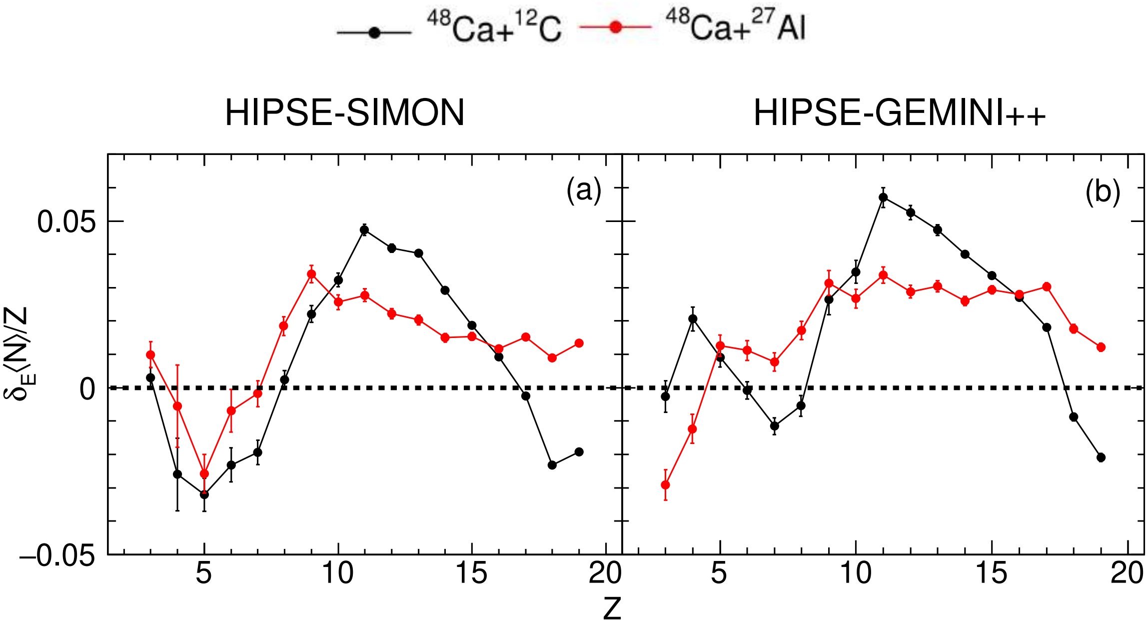

Fig. 4.21: $\delta_E\langle N\rangle/Z = \langle N\rangle/Z_{25} - \langle N\rangle/Z_{40}$ as a function of Z w.r.t. E_B. (a): HIPSE-SIMON ; (b): HIPSE-GEMINI++. Black and red solid squares represent ^{12}C and ^{27}Al target systems, respectively.

Another important observation can be made from the Δ⟨N⟩/Z vs Z correlation given in Fig. 4.22. The Δ⟨N⟩/Z is the difference between the ⟨N⟩/Z of particles emitted in the backward and forward directions in the QP phase space. It is observed that the Δ⟨N⟩/Z for HIPSE-SIMON is positive and has some staggering for Z<8 and then it becomes negative for increasing Z. For HIPSE-GEMINI++, the Δ⟨N⟩/Z remains nearly zero for lighter fragments and then stays negative for increasing Z. Not much details can be inferred from the Δ⟨N⟩/Z values of lighter fragments. The negative value of Δ⟨N⟩/Z for heavier fragments represents that fragments emitted in forward direction have higher ⟨N⟩/Z because they come from neutron rich QP region. The difference arises for 40 MeV/A systems when the Δ⟨N⟩/Z suddenly becomes positive indicating a higher ⟨N⟩/Z of the backward emitted fragments. This sudden decrease of ⟨N⟩/Z in forward emitted fragments is a result of the increased pre-equilibrium emission of neutrons at higher E_B. These observations for heavier fragments w.r.t. E_B can be said to be in agreement with the experimental data. But for the lighter fragments, the observations are inconclusive.

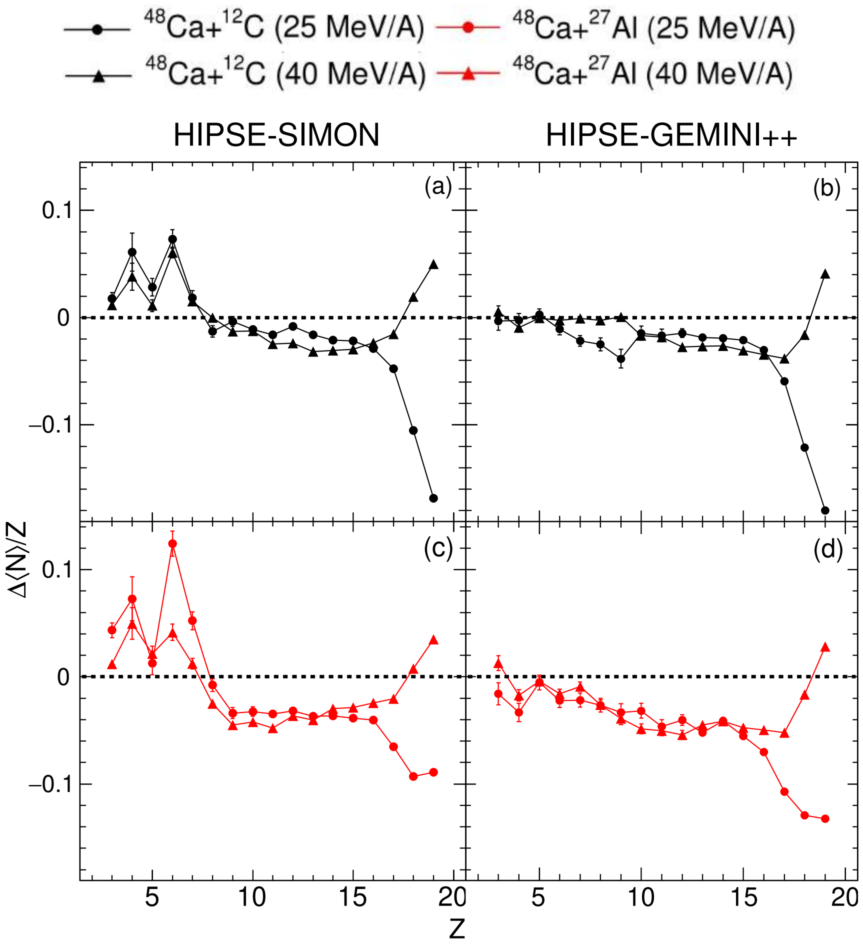

Fig. 4.22: Δ⟨N⟩/Z (= $\langle N\rangle/Z_{BWD} - \langle N\rangle/Z_{FWD}$) and Z correlation from HIPSE data w.r.t. the beam energy E_B. ^{48}Ca+^{12}C system from (a): HIPSE-SIMON data ; (b): HIPSE-GEMINI++ data. ^{48}Ca+^{27}Al system from (c): HIPSE-SIMON data ; (d): HIPSE-GEMINI++ data.

Chapter 5

Comparison of FAZIA-PRE experimental data with HIPSE simulations

In this chapter, the direct comparison of filtered HIPSE simulations with both SIMON and GEMINI++ after-burners with the FAZIA-PRE experimental data is presented. The colour scheme used in this section is as follows: HIPSE-SIMON is represented by red solid circles, HIPSE-GEMINI++ is represented by blue solid circles and the experimental data (EXP) is represented by black solid circles. The comparison between HIPSE data and EXP was done by following the similar procedure of showing firstly the basic reaction observables and then moving on to the isospin related observables.

5.1 For basic reaction observables

The data comparison for basic reaction observables, namely, fragment charge (Z), mass (A) and charged particle multiplicity (M_{tot}) is given in Fig. 5.1. The ratios of the HIPSE data to the EXP are also given in same format in the Fig. 5.2. The ratios help to provide a more quantitative comparison of these data. There are 3 columns for Z, A and M_{tot}, respectively. Also, there are 5 rows for each reaction system which are marked on the left side of the figure. Beginning with the Z distributions, in Fig. 5.1(a)-(e), a qualitative agreement can be observed for all systems. From their ratios in Fig. 5.2(a)-(e), a slight under-estimation of fragments for 25 MeV/A systems in HIPSE-GEMINI++ for $Z \lesssim 15$ is observed. A slight over-estimation of fragments is also seen in 40 MeV/A systems in HIPSE-SIMON for $Z \sim 9-11$. Also, there is an overestimation of heavier fragments around Z=20.

In the A distribution given in Fig. 5.1(f)-(j), the qualitative agreement is observed up to $A \sim 40$ for 25 MeV/A and $A \sim 30$ for 40 MeV/A. The disagreement for higher A values arise due to the inability of fragment production after filtering the HIPSE data because these fragments lie near the mass identification limit of FAZIA. Also, the presence of ^{5}He in EXP in 25 MeV/A systems is not shown by HIPSE-SIMON but is produced by HIPSE-GEMINI++ not fully, but to some extent. For qualitative observations, Fig. 5.2(f)-(j) for the ratios of HIPSE and EXP data provides some insight. Slight under-estimation of fragments in 25 MeV/A systems in HIPSE-GEMINI++ is observed for A$\sim$20$-$30. Over-estimation of fragments is observed in HIPSE-SIMON for 40 MeV/A systems for A$\sim$18$-$25.

For the M$_{tot}$ distributions given in Fig. 5.1(k)-(o), again a qualitative agreement is observed between HIPSE and EXP. The M$_{tot}$ generation by HIPSE does not exactly match with the EXP only for ^{48}Ca+^{12}C and ^{48}Ca+^{40}Ca systems at 25 MeV/A but the slopes of the distributions are similar. This can be also confirmed from the ratios of the data. The Fig. 5.2(k) and (m) show the disagreement in both HIPSE simulations with the EXP.

It is also important to compare with the EXP, the velocity distribution of the fragments generated by HIPSE. Using the longitudinal velocity (v$_{||}$) distribution of the fragments in the laboratory frame, the Z and v$_{||}$ correlation is shown in Fig. 5.3 for all FAZIA-PRE systems. The centre-of-mass velocity (v$_{CM}$) and beam velocity (v$_B$) are marked with vertical red and black dotted lines, respectively. A fine production of fragments is observed for both HIPSE-SIMON and HIPSE-GEMINI++. The only thing that is not observed in HIPSE is the narrowing of distribution around the projectile Z. To recall this fact, due to the increased elastic scattering of the projectile with increasing target mass, the peak of the projectile-like fragments becomes narrower around the projectile Z (here Z=20). This is not observed in HIPSE because of the choice of the maximum value of impact parameter, $b_{max} = R_T + R_P$, where R_T and R_P are radii of target and projectile, respectively. Due to this choice, the domain of elastic scattering events was not present in the HIPSE simulations.

The mean values of all the basic reaction observables discussed above, i.e., mean fragment charge ⟨Z⟩, mean fragment mass ⟨A⟩, mean multiplicity of charged particles ⟨M$_{tot}$⟩ and mean longitudinal velocity ⟨v$_{||}$⟩ are shown in the Table 5.1 for all systems from a brief quantitative perspective. The mean values of the observables from HIPSE-SIMON and HIPSE-GEMINI++ simulations which are relatively closer to the EXP values have been marked in bold text. A clearer picture can be seen by plotting these values, as shown in Fig. 5.4. The four panels show (a): mean fragment charge ⟨Z⟩, (b): mean fragment mass ⟨A⟩, (c): mean multiplicity of charged particles ⟨M$_{tot}$⟩ and (d): mean longitudinal velocity ⟨v$_{||}$⟩ as a quantitative comparison between HIPSE and EXP. From these comparisons, it can be said that the quantitative description of the nuclear reactions by HIPSE is not in a complete agreement with the experimental data.

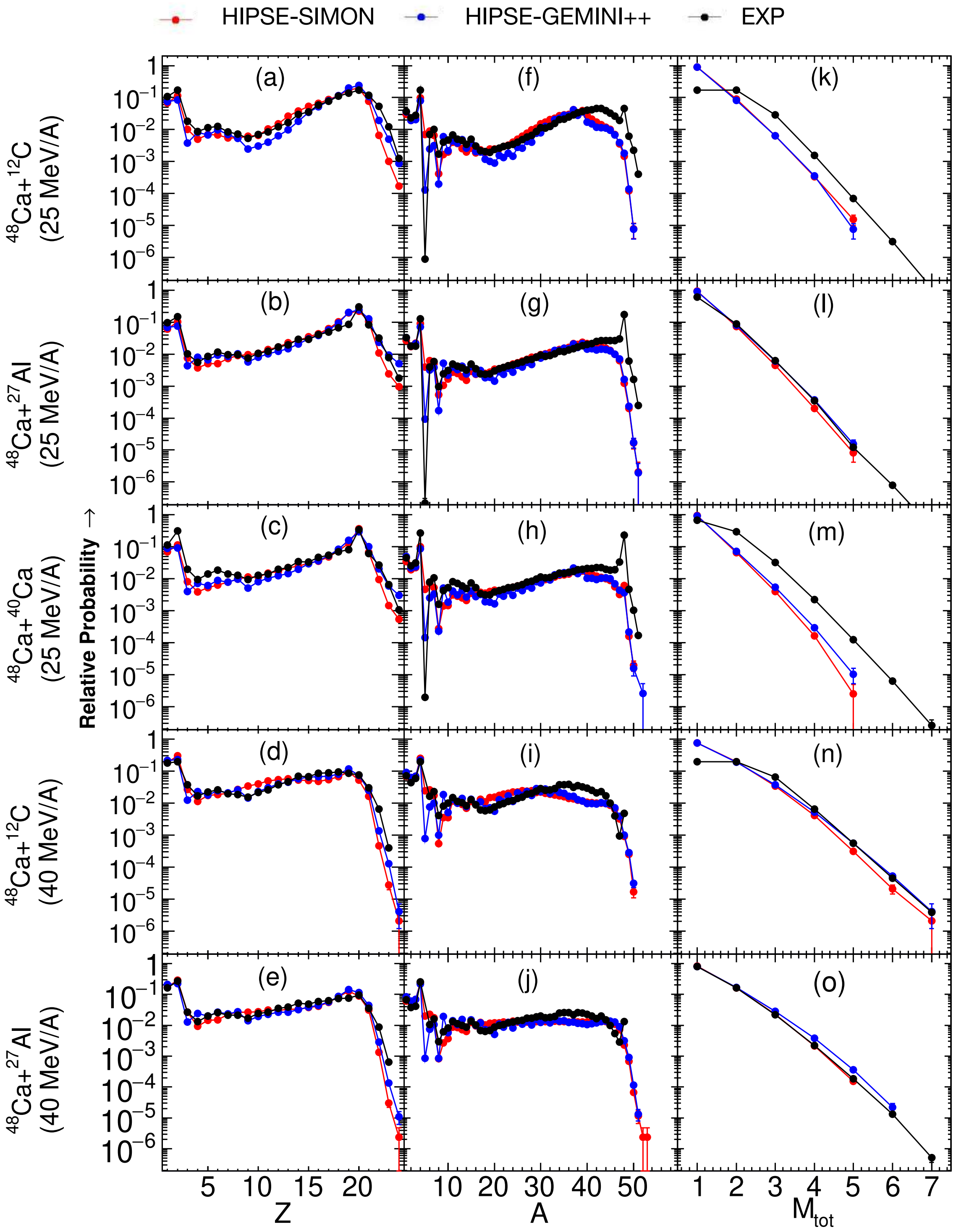

Fig. 5.1: Direct relative comparison of HIPSE simulations from HIPSE-SIMON and HIPSE-GEMINI++ with FAZIA-PRE experimental data (EXP) for basic reaction observables. Each row represents a FAZIA-PRE reaction system. The systems are marked on the left hand side of the figure. Beam energies are given as numbers in parenthesis in implicit units MeV/A. First column shows the Z distributions, second column shows the A distributions and third column shows the M_{tot} distributions.

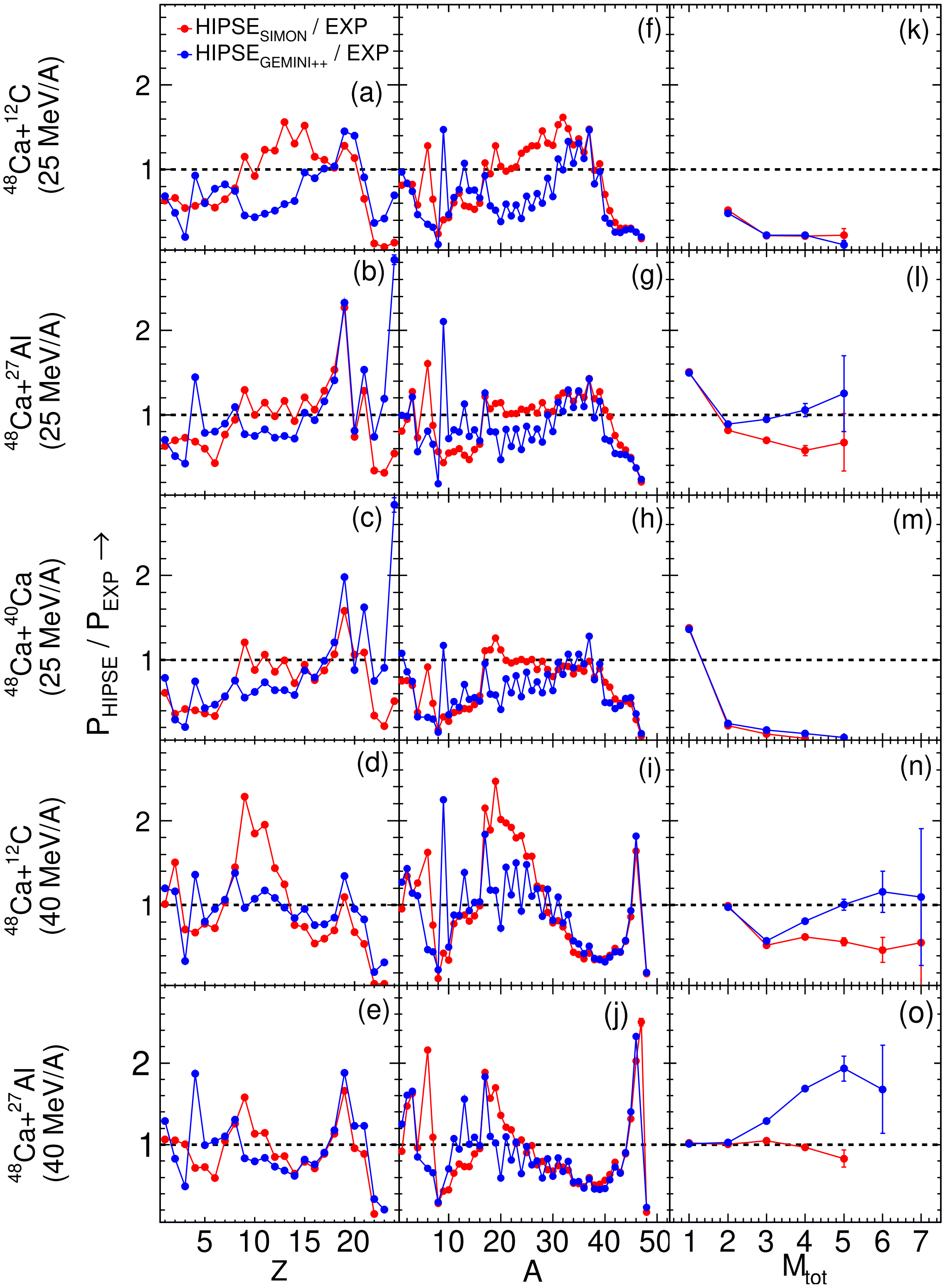

Fig. 5.2: Relative ratios of HIPSE simulations from HIPSE-SIMON and HIPSE-GEMINI++ to the FAZIA-PRE experimental data (EXP) for basic reaction observables. Each row represents a FAZIA-PRE reaction system. The systems are marked on the left hand side of the figure. Beam energies are given as numbers in parenthesis in implicit units MeV/A. First column shows the Z distributions, second column shows the A distributions and third column shows the M_{tot} distributions.

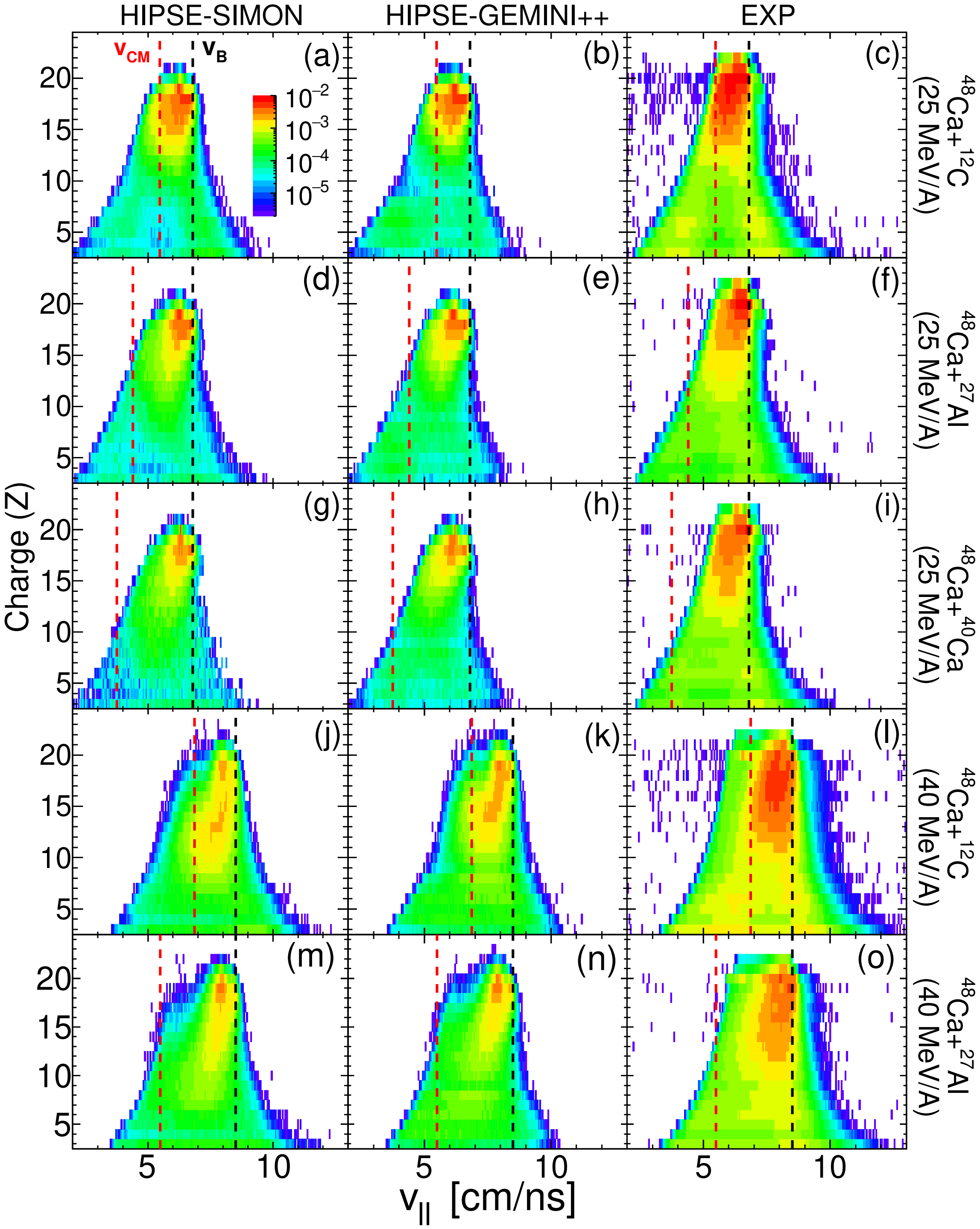

Fig. 5.3: Correlation of Z vs $v_{||}$ as a comparison between HIPSE-SIMON, HIPSE-GEMINI++ and EXP for 25 MeV/A systems ((a) - (i)) and 40 MeV/A systems ((j)-(o)). The v_{CM} (red dashed vertical line) and v_B (black dashed vertical line) are marked in the panels.

Observables	HIPSE-SIMON	HIPSE-GEMINI++	EXP
^{48}Ca+^{12}C (25 MeV/A)			
$\langle Z \rangle$	14.744 ± 0.009	15.716 ± 0.009	12.7 ± 0.001
$\langle A \rangle$	**25.6 ± 0.03**	**25.3 ± 0.03**	25.14 ± 0.002
$\langle M_{tot} \rangle$	1.103 ± 0.001	1.1 ± 0.001	1.4 ± 0.001
$\langle v_{\parallel} \rangle$ [cm/ns]	**6.213 ± 0.002**	**6.123 ± 0.002**	6.31 ± 0.0001
^{48}Ca+^{27}Al (25 MeV/A)			
$\langle Z \rangle$	15.3 ± 0.01	15.9 ± 0.01	14.01 ± 0.001
$\langle A \rangle$	24.654 ± 0.032	24.3 ± 0.034	30.492 ± 0.004
$\langle M_{tot} \rangle$	**1.082 ± 0.0004**	**1.092 ± 0.0004**	1.102 ± 0.001
$\langle v_{\parallel} \rangle$ [cm/ns]	**6.084 ± 0.002**	5.84 ± 0.003	6.4 ± 0.0002
^{48}Ca+^{40}Ca (25 MeV/A)			
$\langle Z \rangle$	15.02 ± 0.011	15.27 ± 0.011	12.2 ± 0.002
$\langle A \rangle$	21.8 ± 0.04	21.514 ± 0.04	26.163 ± 0.005
$\langle M_{tot} \rangle$	1.073 ± 0.0004	1.083 ± 0.001	1.36 ± 0.0001
$\langle v_{\parallel} \rangle$ [cm/ns]	**6.05 ± 0.003**	5.8 ± 0.003	6.4 ± 0.0003
^{48}Ca+^{12}C (40 MeV/A)			
$\langle Z \rangle$	**9.2 ± 0.01**	10.041 ± 0.01	9.1 ± 0.001
$\langle A \rangle$	16.13 ± 0.02	16.674 ± 0.021	17.832 ± 0.001
$\langle M_{tot} \rangle$	1.3 ± 0.001	1.3 ± 0.001	1.6 ± 0.001
$\langle v_{\parallel} \rangle$ [cm/ns]	**7.721 ± 0.002**	**7.6 ± 0.002**	7.6 ± 0.0001
^{48}Ca+^{27}Al (40 MeV/A)			
$\langle Z \rangle$	**9.9 ± 0.01**	**10.44 ± 0.01**	9.97 ± 0.002
$\langle A \rangle$	16.1 ± 0.024	16.1 ± 0.024	19.22 ± 0.003
$\langle M_{tot} \rangle$	**1.22 ± 0.001**	**1.234 ± 0.001**	1.212 ± 0.0001
$\langle v_{\parallel} \rangle$ [cm/ns]	**7.452 ± 0.003**	**7.15 ± 0.003**	7.62 ± 0.0003

Table 5.1: Comparison between HIPSE-SIMON and HIPSE-GEMINI++ with the EXP data for mean fragment charge ⟨Z⟩, mean fragment mass ⟨A⟩, mean multiplicity of charged particles $\langle M_{tot} \rangle$ and mean longitudinal velocity $\langle v_{\parallel} \rangle$ for all FAZIA-PRE systems.

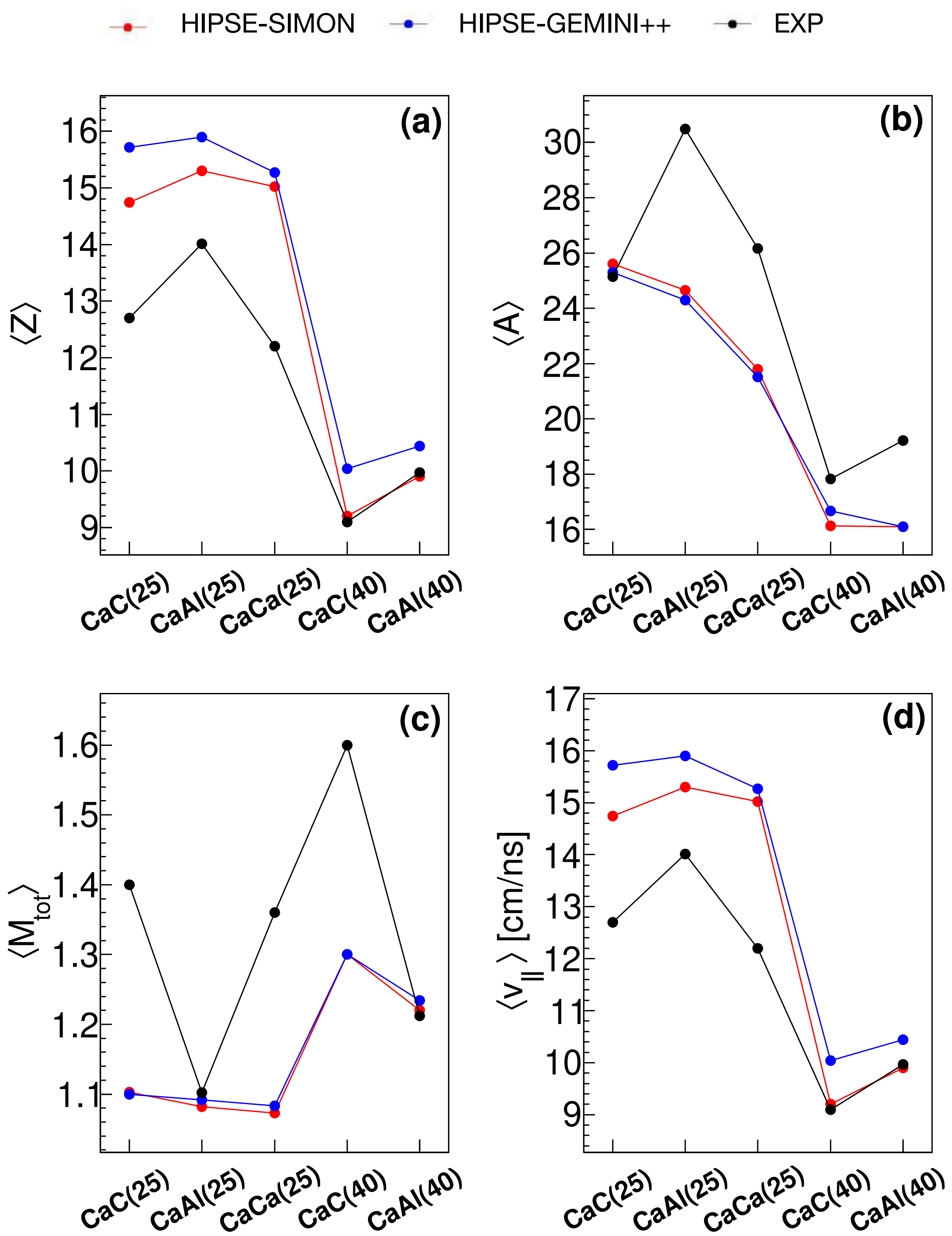

Fig. 5.4: A quantitative comparison between HIPSE-SIMON (red circles), HIPSE-GEMINI++ (blue circles) and EXP (black circles). (a): mean fragment charge ⟨Z⟩, (b): mean fragment mass ⟨A⟩, (c): mean multiplicity of charged particles $\langle M_{tot} \rangle$ and (d): mean longitudinal velocity $\langle v_{\parallel} \rangle$.

5.2 Isospin related observables

After establishing a qualitative agreement between HIPSE and EXP for basic reaction observables, it is important to check whether the model can produce the isospin (N/Z) related effects of a nuclear reaction at intermediate energies. Repeating the same procedure of investigating ⟨N⟩/Z of reaction products, the Fig.5.5 − Fig.5.9 show the N distributions as a comparison between HIPSE and EXP for isotopic content of fragments from all FAZIA-PRE systems for Z=3−20. It can be seen that overall, HIPSE-SIMON and HIPSE-GEMINI++ do a fine production of the isotopes of fragments up to Z∼16. Just a slight disagreement is found in HIPSE-SIMON for Z=4. From these N distributions, the ⟨N⟩ was calculated for HIPSE-SIMON and HIPSE-GEMINI++ to compare the fragment ⟨N⟩/Z with the EXP.

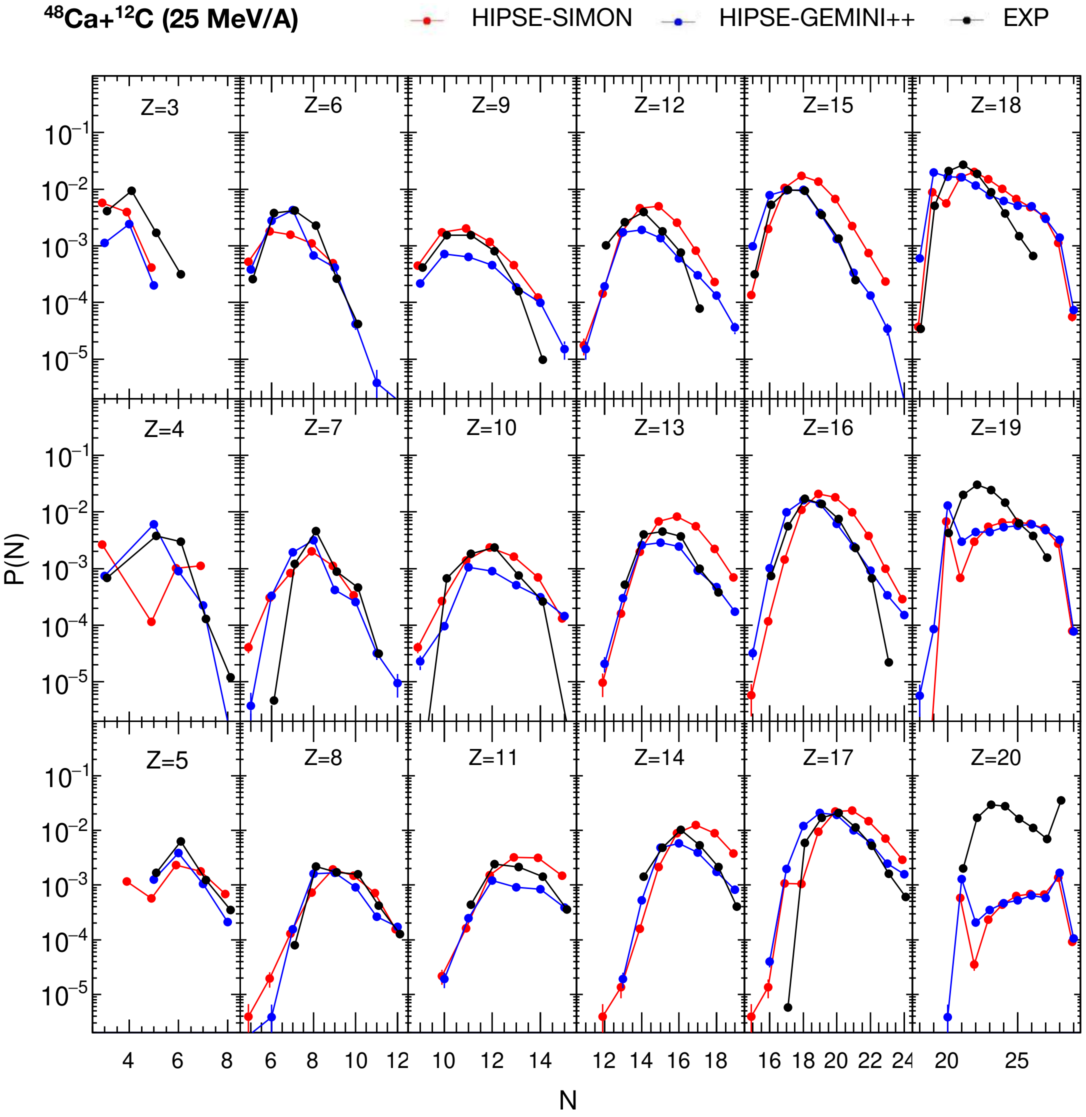

Fig. 5.5: Neutron (N) distribution for each Z (= 3-20) for ^{48}Ca+^{12}C (25 MeV/A) system as a comparison between HIPSE and EXP.

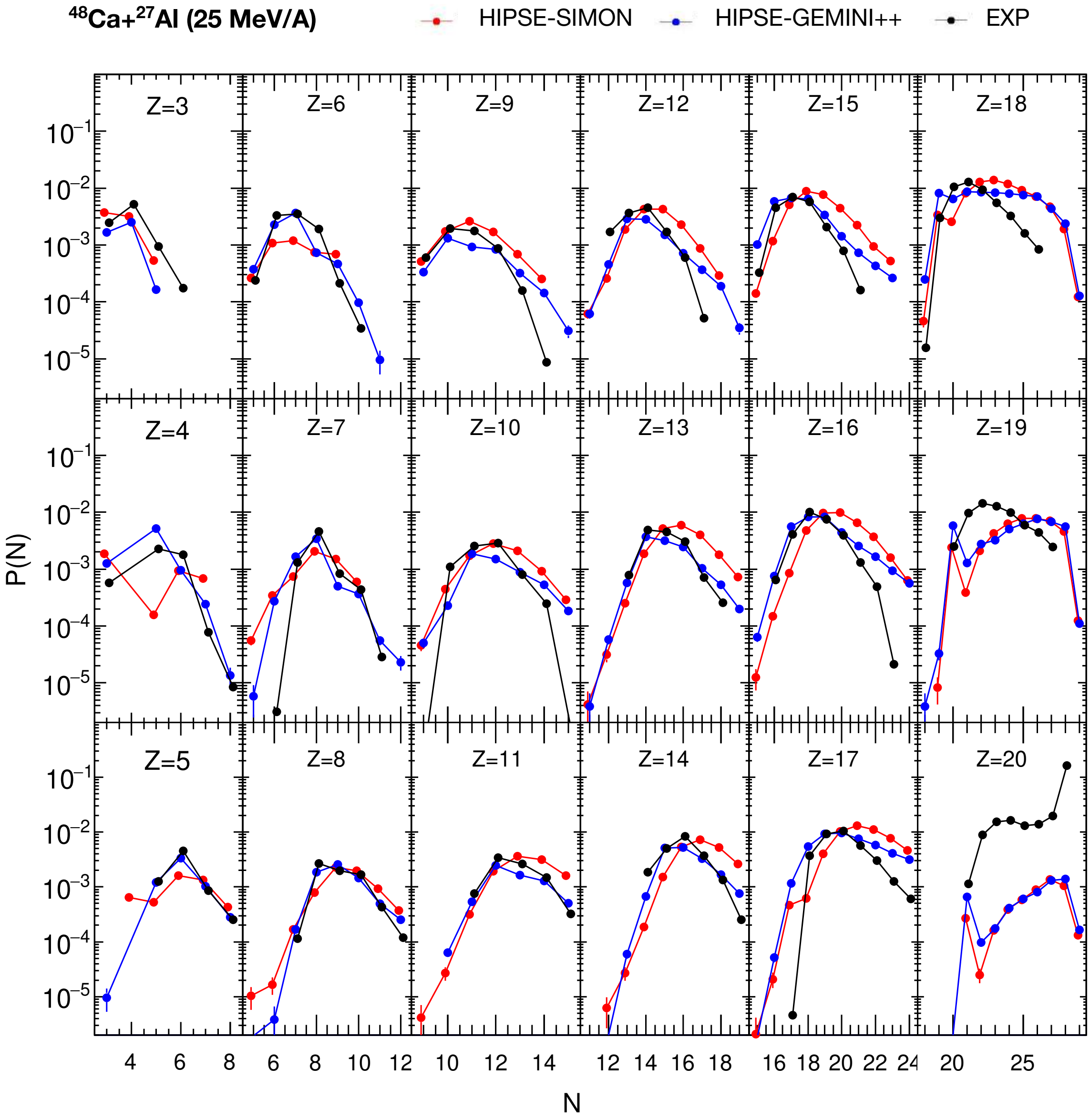

Fig. 5.6: Neutron (N) distribution for each Z (= 3-20) for ^{48}Ca+^{27}Al (25 MeV/A) system as a comparison between HIPSE and EXP.

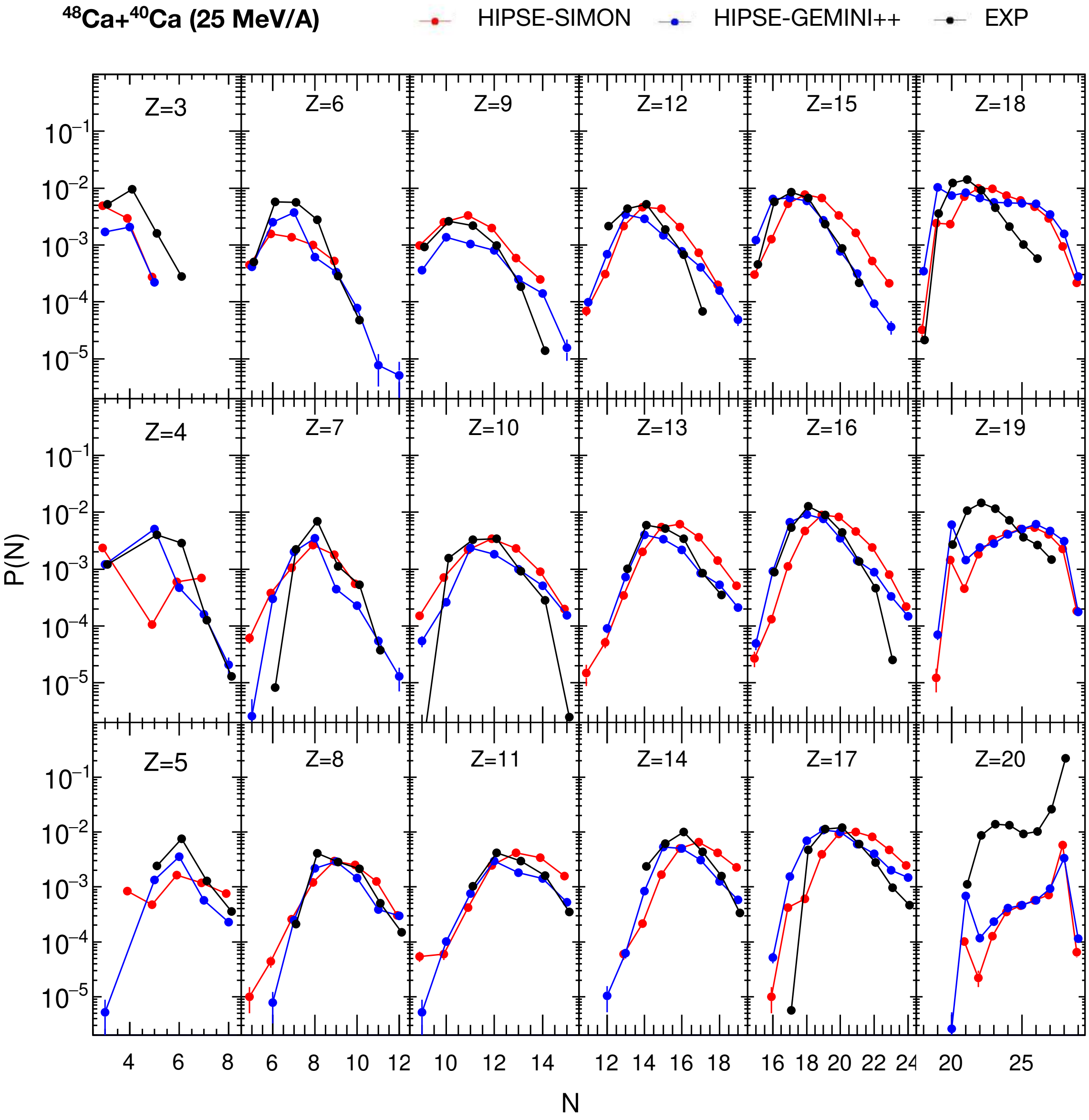

Fig. 5.7: Neutron (N) distribution for each Z (= 3-20) for ^{48}Ca+^{40}Ca (25 MeV/A) system as a comparison between HIPSE and EXP.

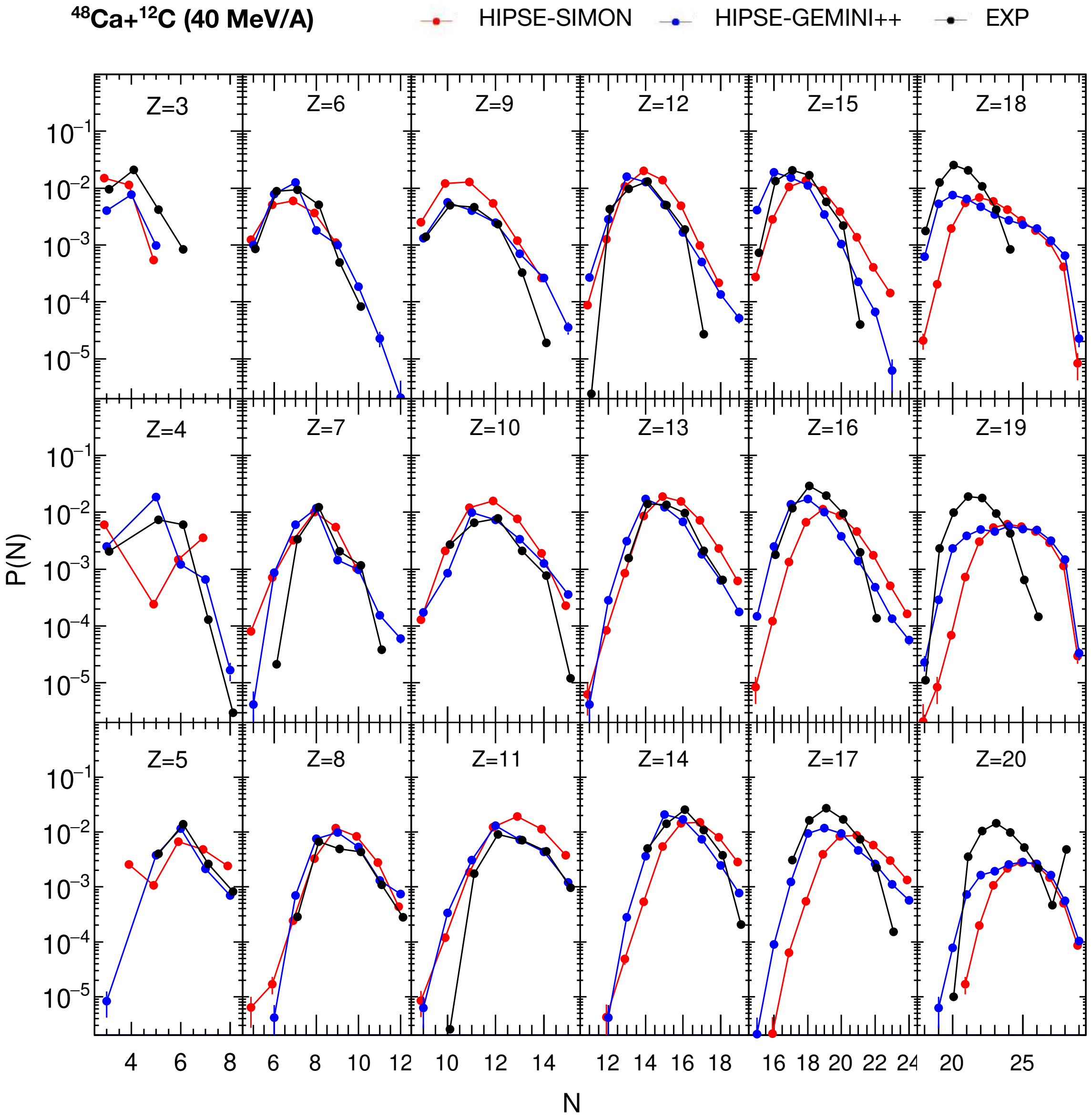

Fig. 5.8: Neutron (N) distribution for each Z (= 3-20) for ^{48}Ca+^{12}C (40 MeV/A) system as a comparison between HIPSE and EXP.

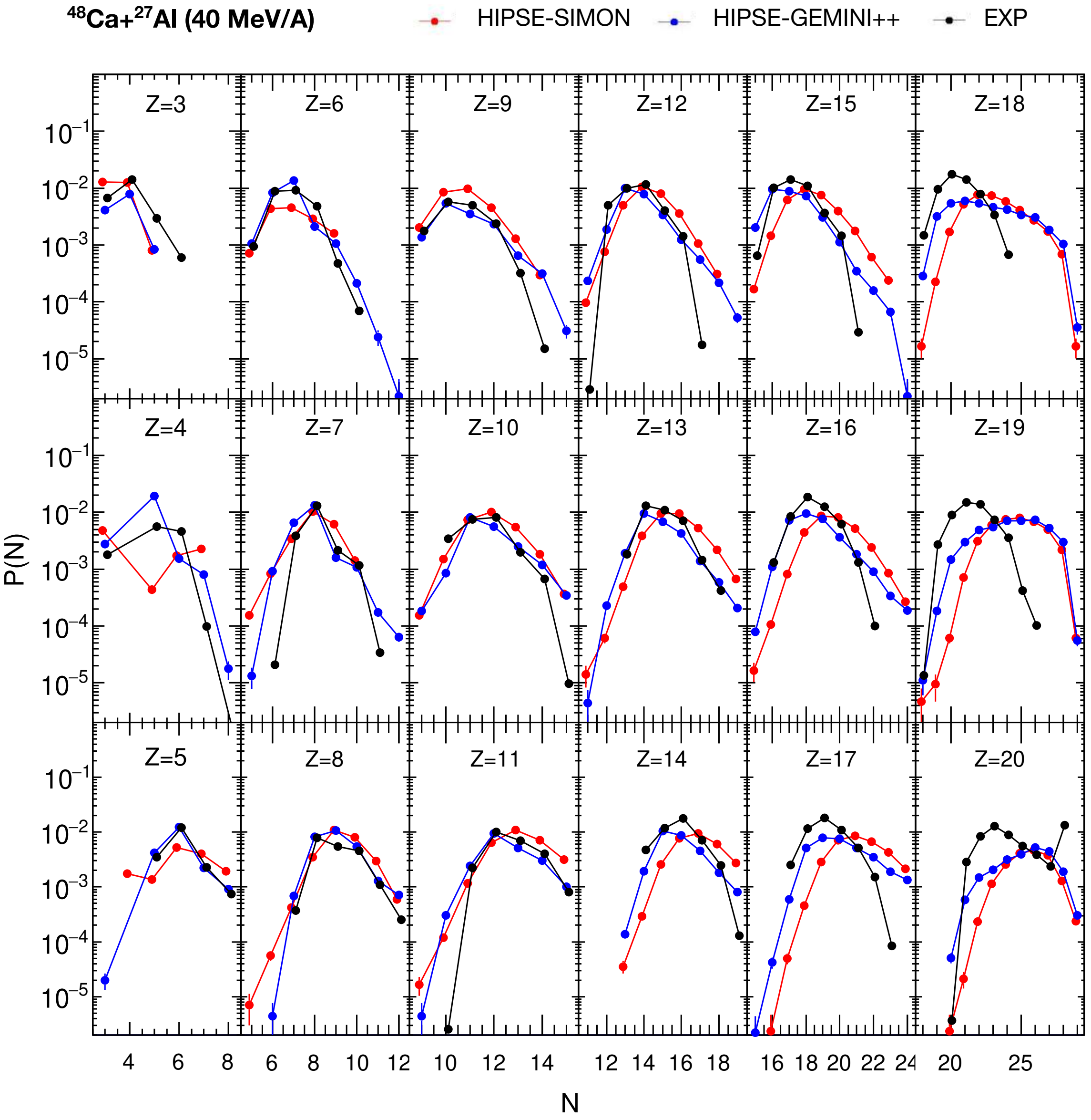

Fig. 5.9: Neutron (N) distribution for each Z (= 3-20) for ^{48}Ca+^{27}Al (40 MeV/A) system as a comparison between HIPSE and EXP.

The ⟨N⟩/Z was then plotted as a function of Z for Z=3 to Z=20 fragments for HIPSE-SIMON, HIPSE-GEMINI and EXP. This is shown here in Fig. 5.10(a)-(e) for all FAZIA-PRE systems (names of the systems are marked within the panels). For the lighter fragments (Z< 5), ⟨N⟩/Z from HIPSE has lower value than the EXP. For the fragments with Z=5−10, the ⟨N⟩/Z values of HIPSE and EXP are very close to each other. For the heavier fragments (Z>10), HIPSE-SIMON produced fragments with higher ⟨N⟩/Z than EXP, whereas, the HIPSE-GEMINI++ produced fragments with comparable ⟨N⟩/Z up to a certain point which then increases more than EXP near the projectile Z (=20). From these observations, one can say that in comparison to the EXP, there is a reasonable agreement in the ⟨N⟩/Z of the fragments generated by HIPSE.

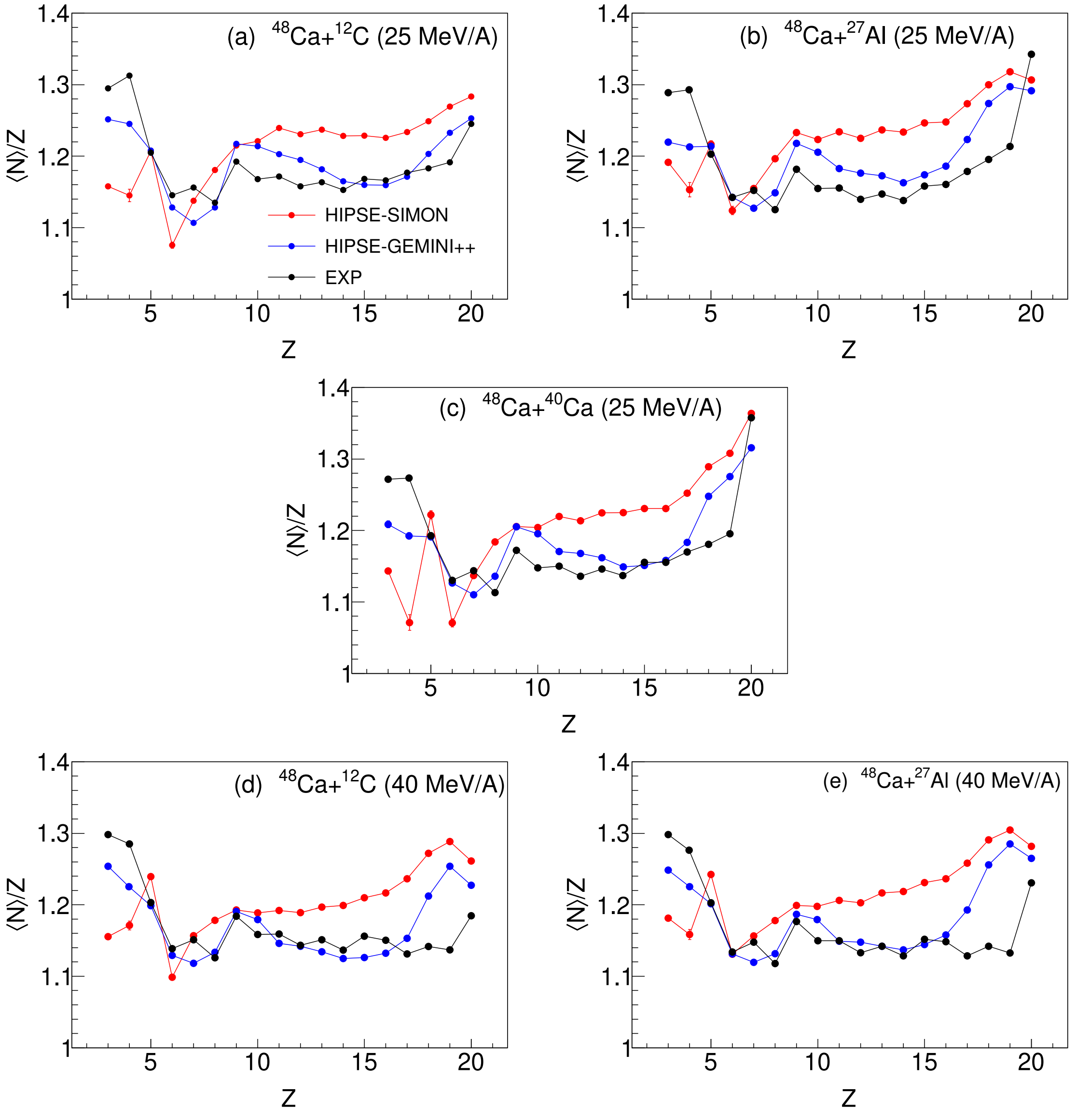

Fig. 5.10: ⟨N⟩/Z vs Z correlation for all FAZIA-PRE systems as a comparison between HIPSE and EXP. (a): ^{48}Ca+^{12}C (25 MeV/A); (b): ^{48}Ca+^{27}Al (25 MeV/A); (c): ^{48}Ca+^{40}Ca (25 MeV/A); (d): ^{48}Ca+^{12}C (40 MeV/A); (e): ^{48}Ca+^{27}Al (40 MeV/A).

Moving towards a more detailed investigation of comparing the ⟨N⟩/Z of the fragments produced by HIPSE to the EXP, the ⟨N⟩/Z and $v_{\parallel}$ correlation is given in Fig. 5.11(a)-(e) for all FAZIA-PRE systems (names of the systems are marked within the panels). The vertical black dotted line represents the v_B in laboratory frame. The overall shape of the distribution of ⟨N⟩/Z on the velocity scale has a reasonable agreement between HIPSE and EXP. HIPSE data matches with the EXP around the v_B for 25 MeV/A. But for 40 MeV/A, ⟨N⟩/Z of HIPSE data around v_B, having lower values than 25 MeV/A systems, still have high values compared to the EXP. The fragments produced by HIPSE-SIMON and HIPSE-GEMINI have low ⟨N⟩/Z than the EXP near the v_{CM} (between 3-5 cm/ns for all the systems).

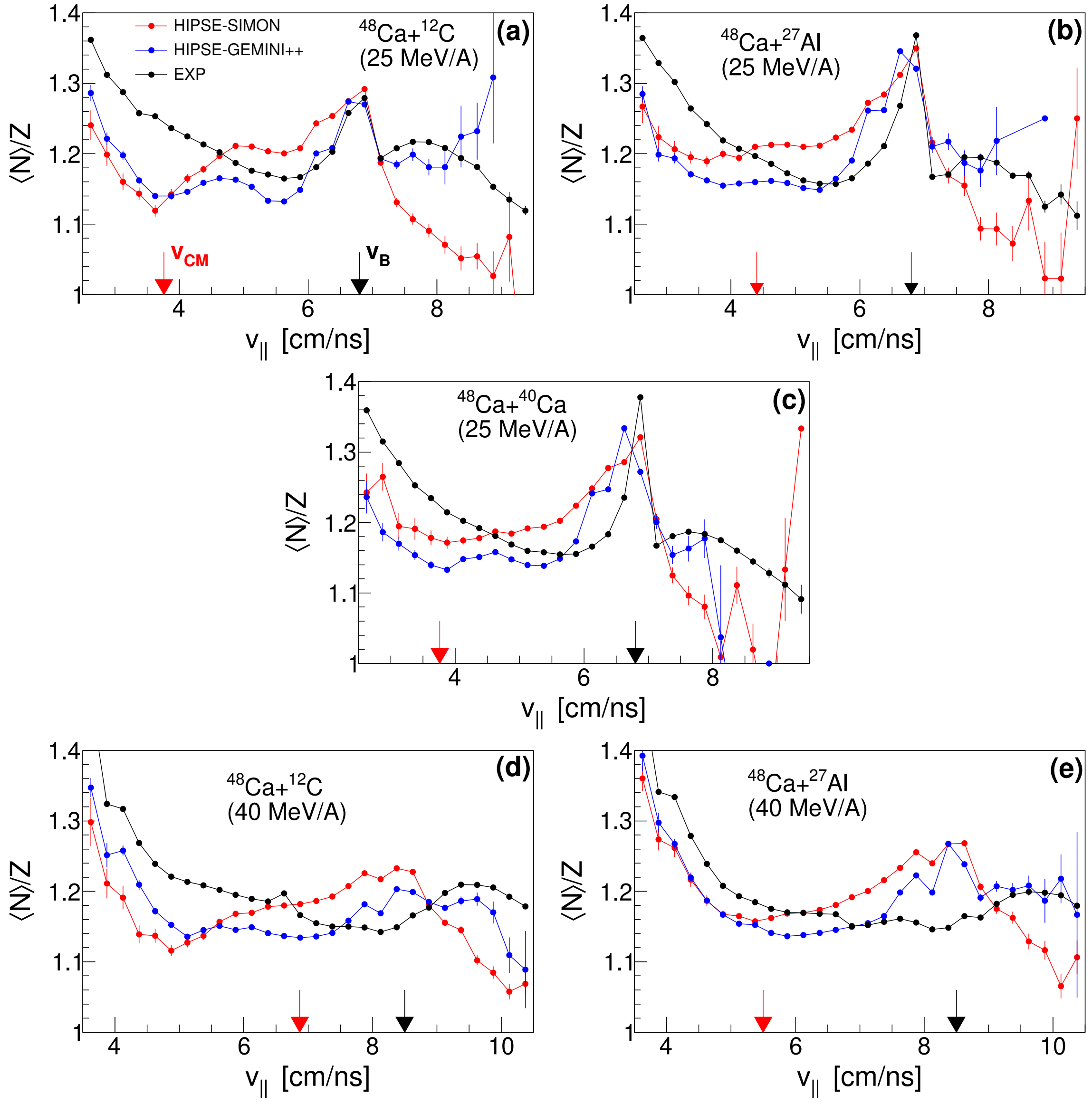

Fig. 5.11: ⟨N⟩/Z vs $v_{\parallel}$ correlation for all FAZIA-PRE systems as a comparison between HIPSE and EXP. (a): ^{48}Ca+^{12}C (25 MeV/A); (b): ^{48}Ca+^{27}Al (25 MeV/A); (c): ^{48}Ca+^{40}Ca (25 MeV/A); (d): ^{48}Ca+^{12}C (40 MeV/A); (e): ^{48}Ca+^{27}Al (40 MeV/A).

To check whether the HIPSE fragments coming from the neck have high ⟨N⟩/Z due to isospin drift, the detailed ⟨N⟩/Z and $v_{||}$ correlation is given in Fig. 5.12 – Fig. 5.16 for fragments with Z=3 to Z=20. From these plots, it is visible that the HIPSE is not able to produce a detailed structure of the fragment ⟨N⟩/Z. The light fragments generated by HIPSE supposed to be coming from the neutron rich neck have comparatively low ⟨N⟩/Z closer to the v_{CM}. This ⟨N⟩/Z stays nearly same up to Z=8. This is a disagreement with the trends from the experimental data. Also, moving towards higher Z values, the ⟨N⟩/Z near v_B in HIPSE data is high for all fragments. This is clearly an over-estimation of fragment ⟨N⟩/Z by HIPSE.

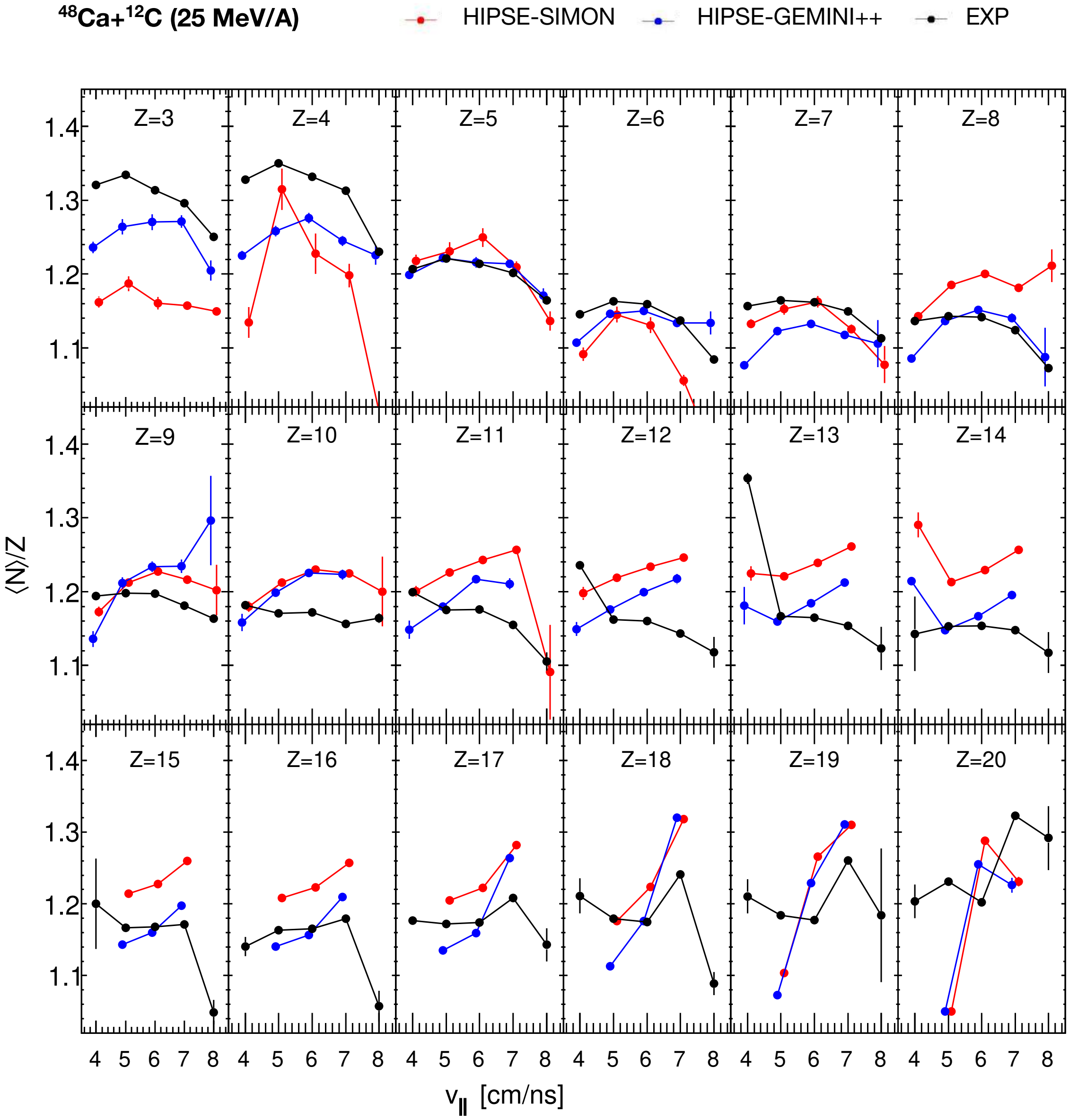

Fig. 5.12: ⟨N⟩/Z as a function of longitudinal velocity ($v_{||}$) for each Z (= 3-20) for ^{48}Ca+^{12}C (25 MeV/A) system as a comparison between HIPSE and EXP.

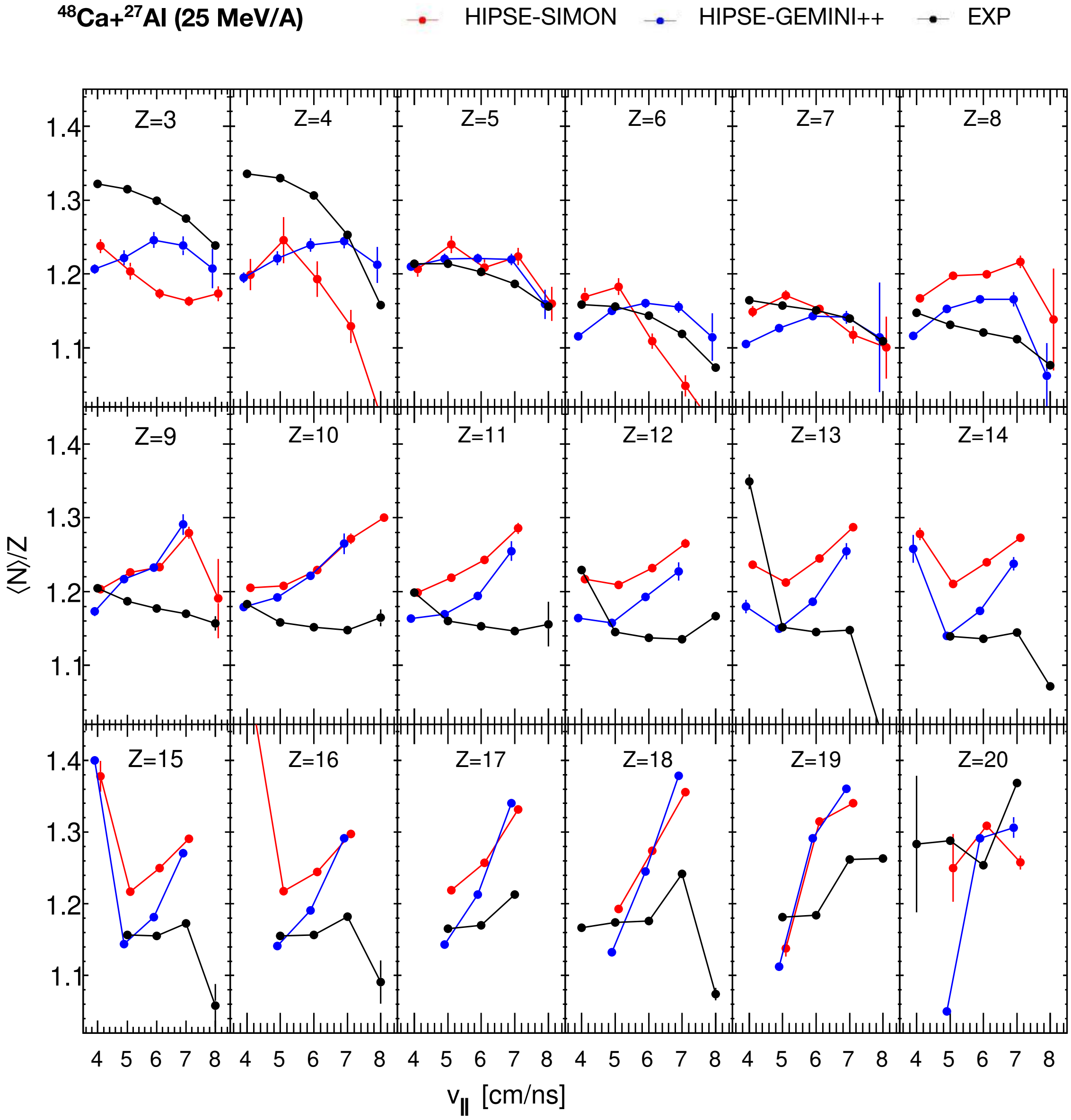

Fig. 5.13: ⟨N⟩/Z as a function of longitudinal velocity ($v_{||}$) for each Z (= 3-20) for ^{48}Ca+^{27}Al (25 MeV/A) system as a comparison between HIPSE and EXP.

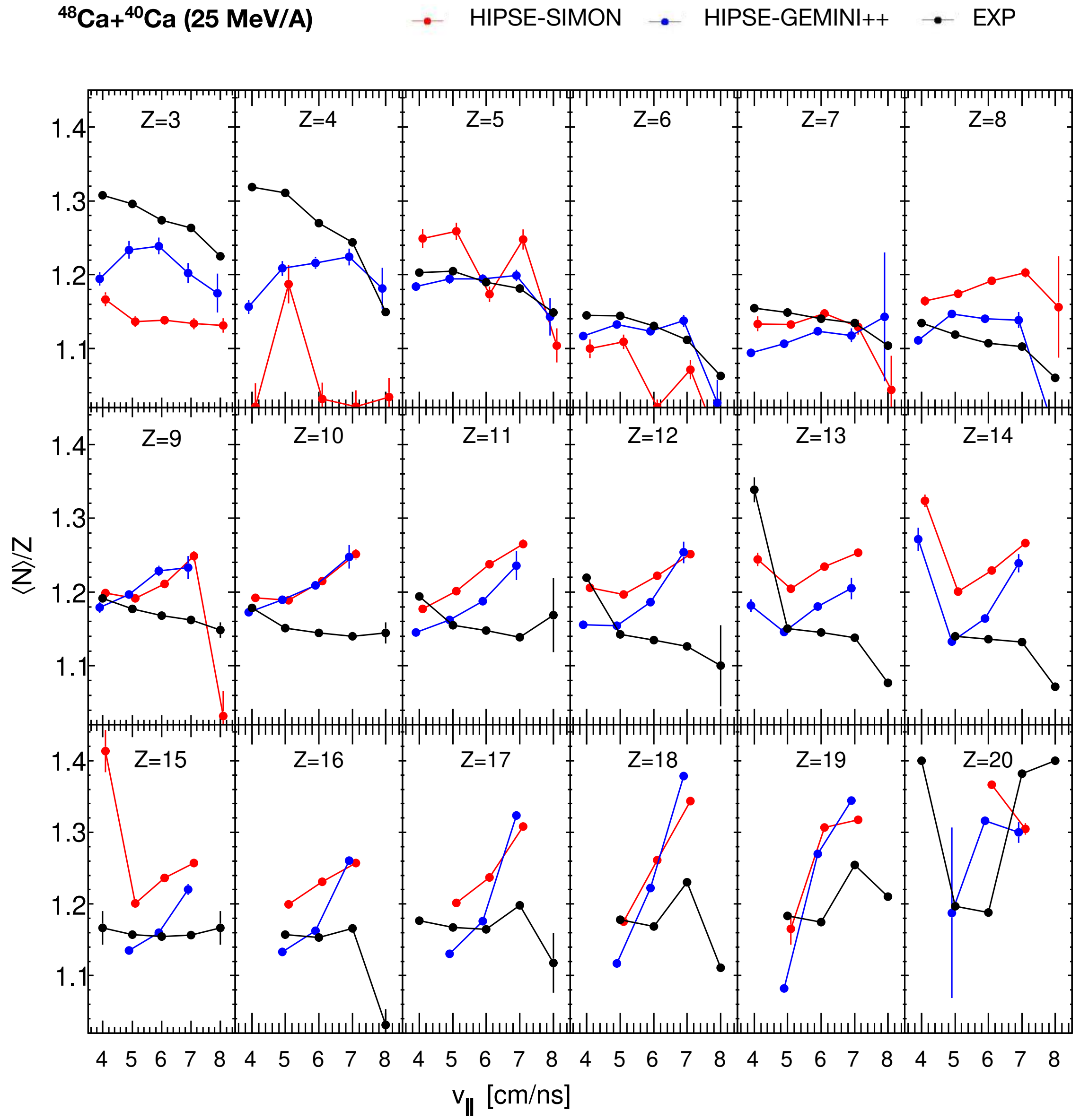

Fig. 5.14: $\langle N \rangle /Z$ as a function of longitudinal velocity ($v_{\parallel}$) for each Z (= 3-20) for ^{48}Ca+^{40}Ca (25 MeV/A) system as a comparison between HIPSE and EXP.

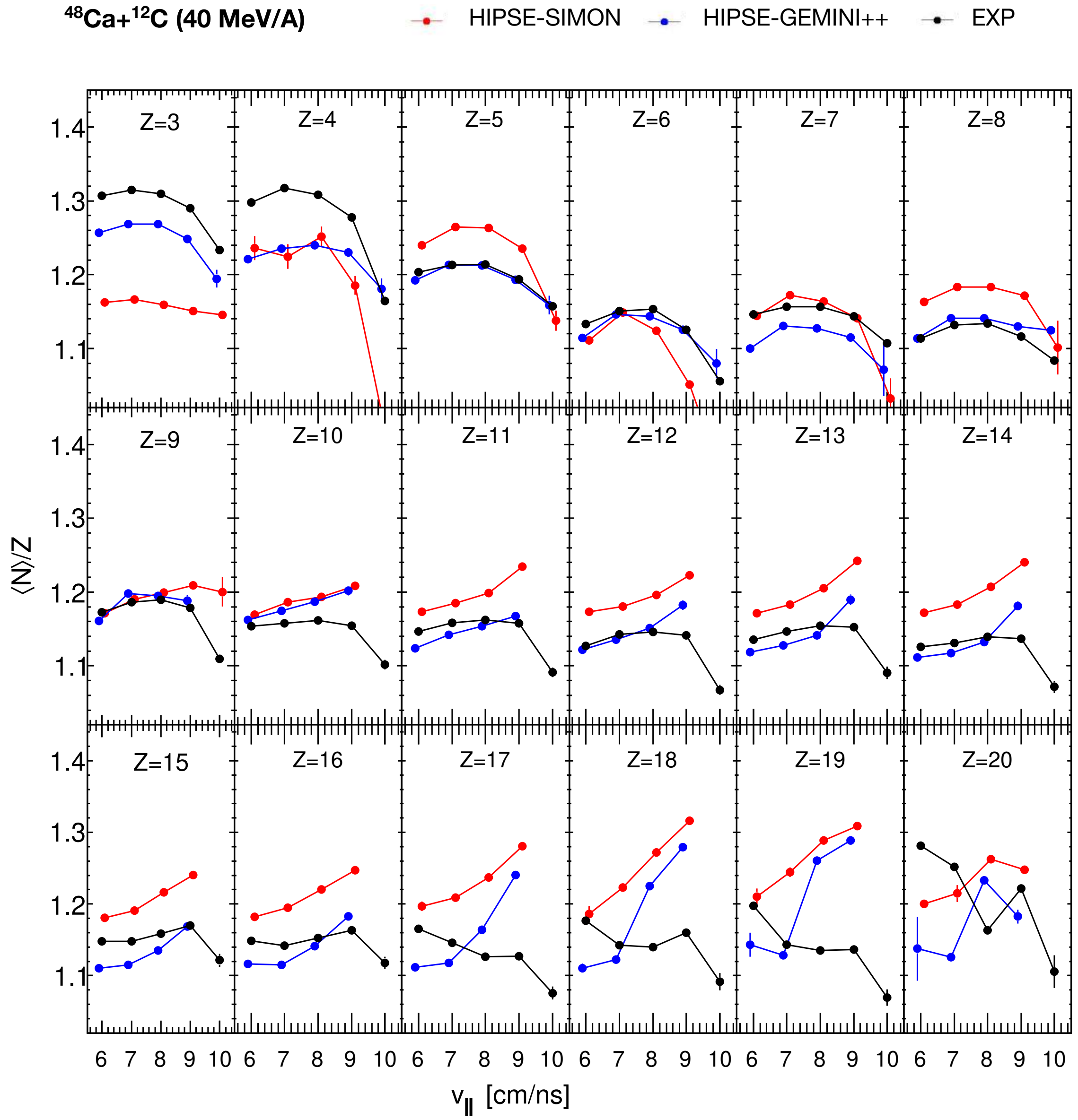

Fig. 5.15: ⟨N⟩/Z as a function of longitudinal velocity ($v_{\parallel}$) for each Z (= 3-20) for ^{48}Ca+^{12}C (40 MeV/A) system as a comparison between HIPSE and EXP.

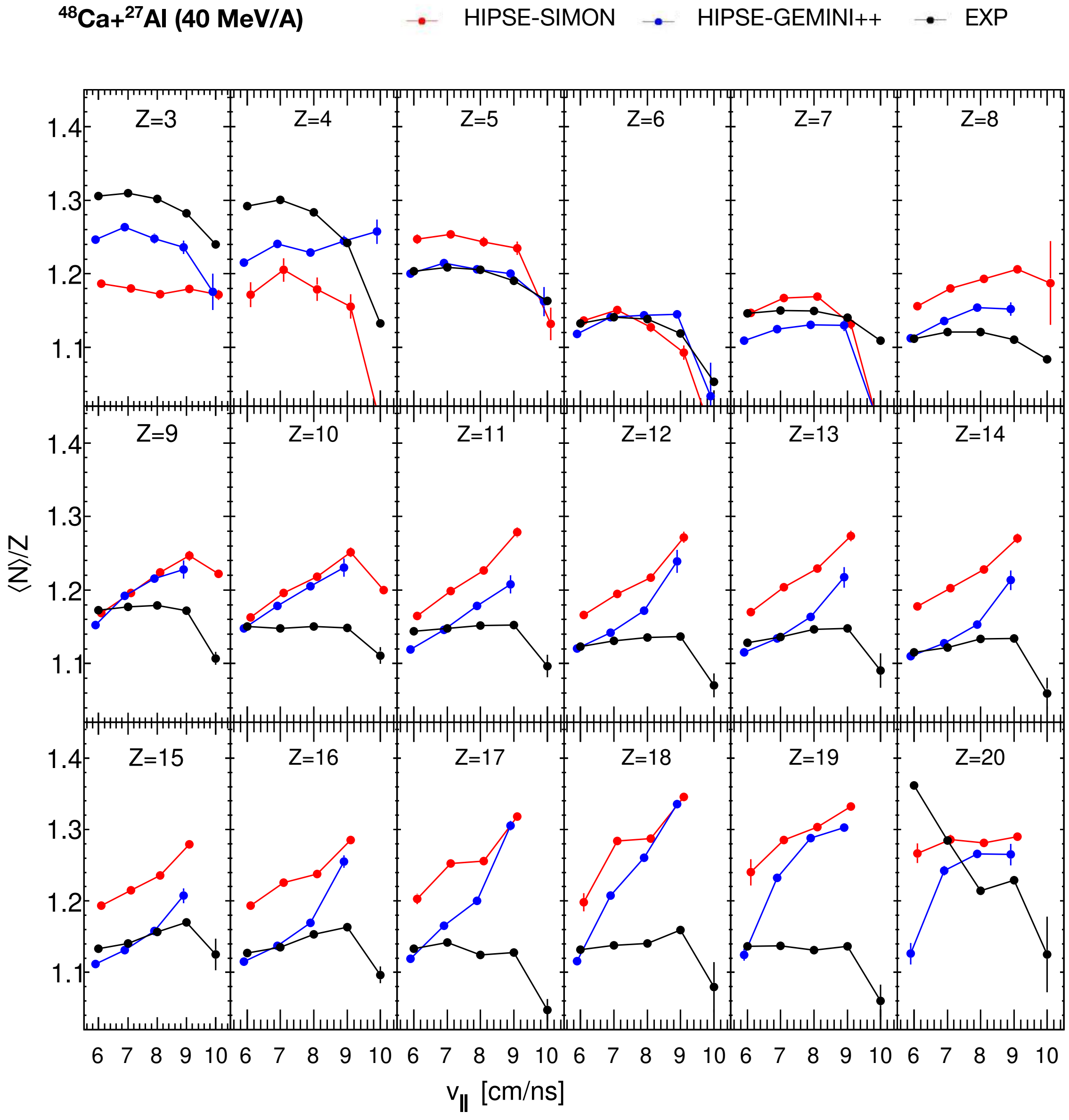

Fig. 5.16: ⟨N⟩/Z as a function of longitudinal velocity ($v_{\|}$) for each Z (= 3-20) for ^{48}Ca+^{27}Al (40 MeV/A) system as a comparison between HIPSE and EXP.

After this, the method of splitting the fragments emitted in the backward (BWD) and forward (FWD) directions in the QP phase space as explained in Chapter 3 was used. Just for recollection, the $\langle N \rangle/Z$ of the BWD fragments had contributions of the backward emitted fragments in QP reference frame as well some neck emissions. on the other hand, the FWD fragments are the ones which were emitted in the forward direction in the QP reference frame. Subtracting the $\langle N \rangle/Z$ of FWD from BWD helps to verify the presence of neck contributions. Therefore, we had used $\Delta\langle N \rangle/Z = \langle N \rangle/Z_{BWD} - \langle N \rangle/Z_{FWD}$. For the comparison of HIPSE data with EXP, the $\Delta\langle N \rangle/Z$ as a function of Z is shown in Fig. 5.17(a)-(e) for all FAZIA-PRE systems. The first observation here is that the shape of the

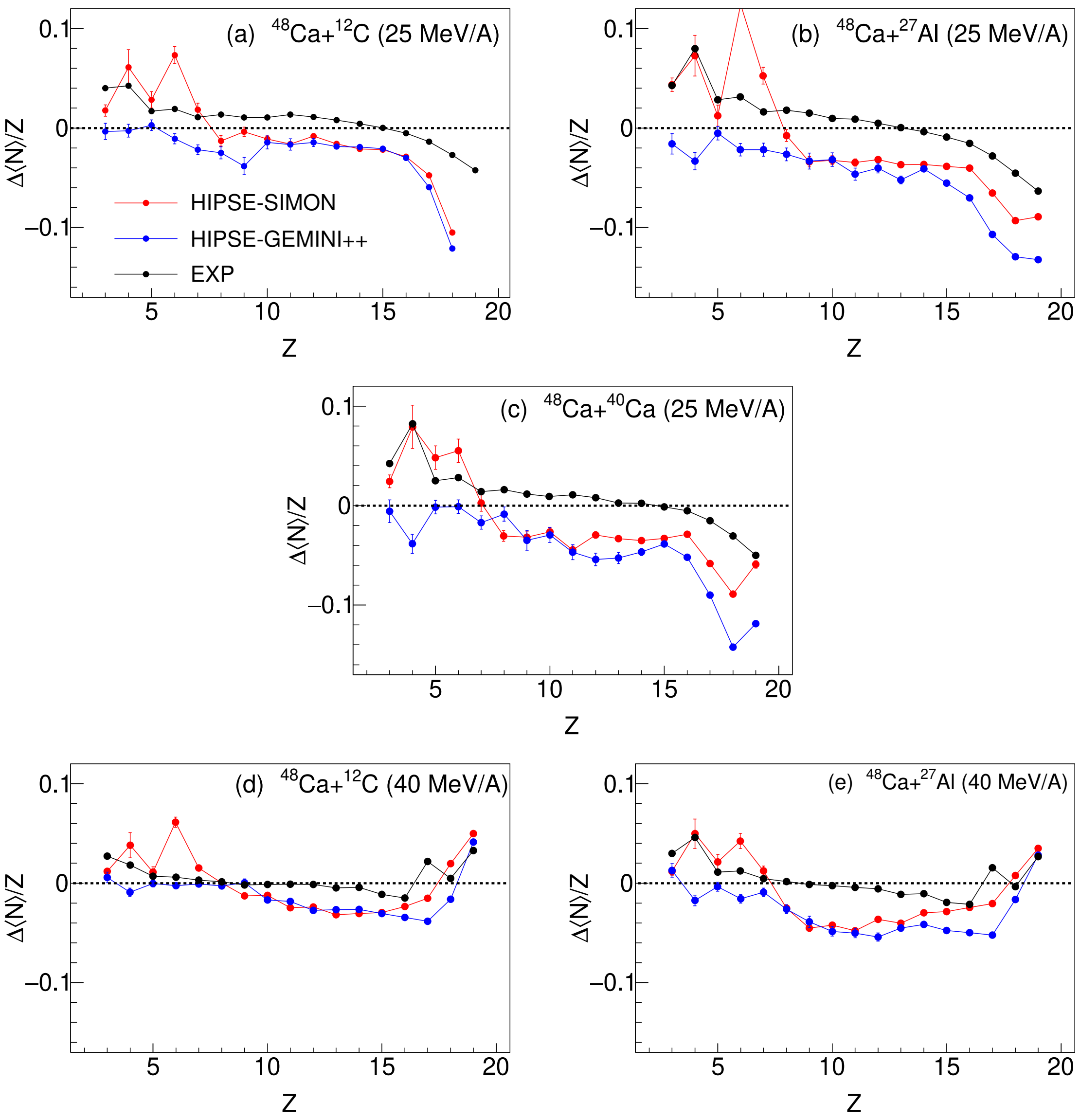

Fig. 5.17: $\Delta\langle N \rangle/Z$ (= $\langle N \rangle/Z_{BWD} - \langle N \rangle/Z_{FWD}$) and Z correlation for all FAZIA-PRE systems as a comparison between HIPSE and EXP. (a): ^{48}Ca+^{12}C (25 MeV/A) ; (b): ^{48}Ca+^{27}Al (25 MeV/A) ; (c): ^{48}Ca+^{40}Ca (25 MeV/A) ; (d): ^{48}Ca+^{12}C (40 MeV/A) ; (e): ^{48}Ca+^{27}Al (40 MeV/A).

$\Delta\langle N\rangle/Z$ produced by both HIPSE simulations as compared to the EXP has a reasonable agreement. HIPSE-SIMON has clearly shown better neck contributions, i.e., the positive $\Delta\langle N\rangle/Z$ for $Z<6$ fragments indicating a neutron rich neck. Although there is some staggering present. HIPSE-GEMINI++ does not show any N/Z effects for lighter fragments as $\Delta\langle N\rangle/Z$ stays near zero. For the fragments with $Z>7$, both HIPSE-SIMON and HIPSE-GEMINI++ have very strong FWD effects in fragment $\langle N\rangle/Z$ (also observed in previous figures). For 40 MeV/A, the inversion of $\Delta\langle N\rangle/Z$ from negative to positive around projectile Z due to increased pre-equilibrium neutron emissions at higher beam energy is well presented in HIPSE data.

Chapter 6

Summary and conclusion

The research work presented here is mainly focused on the analysis of the data from the FAZIA-PRE experiment, performed using 6 FAZIA blocks at LNS-INFN, Catania, Italy in February 2018. The considered reaction systems were ^{48}Ca+^{12}C (25 and 40 MeV/A), ^{48}Ca+^{27}Al (25 and 40 MeV/A) and ^{48}Ca+^{40}Ca (25 MeV/A). The aim of the experiment was to study the effects of pre-equilibrium neutron emissions from a neutron rich projectile, on the N/Z of reaction products. As the detector setup consisting of 6 blocks had a small angular acceptance ($\sim 2^\circ - 18^\circ$), most of the fragments that were detected in the experiment belong to the quasi-projectile (QP) region of the reaction system.

The projectile (^{48}Ca) was neutron rich and has a high N/Z (= 1.4), and the targets were mostly N/Z symmetric, i.e. N/Z $\approx$ 1. Also, there were two beam energies, 25 and 40 MeV/A. Due to these experimental specifications, it was possible to study the dependence of the target mass and beam energy on various basic reaction observables such as charge (Z), mass (A), multiplicity of charged particles (M_{tot}), longitudinal (parallel) velocity ($v_{\parallel}$). Also, the target mass and beam energy dependence was observed for the N/Z of the reaction products.

The observations made from the experimental data analysis were as follows:

- The relative yield of light fragments and intermediate-mass fragments increases with increasing target mass.
- The relative yield of heavier fragments decreases with increasing target mass.
- Lighter fragments (Z<7) formed in the ^{48}Ca+^{27}Al system have lowest yield due to the lowest neutron and proton separation energies of ^{27}Al.
- The relative yield of heavier fragments decreases with increasing beam energy due to increasing multi-fragmentation. This leads to increased break-up of heavier fragments consequently increasing the relative yield of lighter fragments.
- The fragment $\langle N \rangle /Z$ was observed to be decreasing with increasing target mass.

- The fragment ⟨N⟩/Z was observed to be decreasing with increasing beam energy. This observation is related to the effects of pre-equilibrium neutron emissions and secondary decays.
- Isospin drift was also observed in this data.
- The variation in fragment ⟨N⟩/Z in backward and forward directions in the QP reference frame was observed to be stronger at lower beam energy.

After the experimental data analysis, the HIPSE model was used to check its consistency for the intermediate energy nuclear reactions. It was coupled with SIMON and GEMINI++ de-excitation codes to obtain the secondary decay fragments. The ability of HIPSE to generate the fragment ⟨N⟩/Z was also checked. Simulated data from same reaction systems from FAZIA-PRE experiment were produced to check the target mass and beam energy dependence within the HIPSE model. The following are the conclusions:

- No substantial dependence on the mass of the target was observed in HIPSE data for either Z, A, M_{tot}, $v_{||}$ or fragment ⟨N⟩/Z.
- Effects of beam energy dependence on fragments was observed in HIPSE data.
- The effects on the fragment ⟨N⟩/Z due to pre-equilibrium neutron emissions at high beam energy were also observed.

Later, a detailed study of HIPSE simulations in comparison with the FAZIA-PRE experimental data for 5 different systems led to the following conclusions:

- HIPSE gives an overall qualitative reproduction of the experimental data with respect to basic reaction observables (Z, A, M_{tot} and $v_{||}$). A low quantitative agreement is found.
- HIPSE is able to produce the fragment ⟨N⟩/Z with a reasonable agreement to the experimental data. But it cannot give a detailed structure of the fragment ⟨N⟩/Z. This is probably due to the absence of an explicit isospin transport mechanism within the HIPSE frameworks.

We can conclude that the HIPSE event generator is a fine tool to generate the fragments from nuclear reactions at intermediate energy range with respect to the basic reaction observables and to have an idea about the overall dynamics. But due to its inability to produce a detailed structure of N/Z of the reaction products, it is not advisable to use HIPSE to study isospin effects in nuclear reactions at intermediate energy range. One would rather use models such as AMD to investigate the fragment ⟨N⟩/Z and other isospin and symmetry energy related studies.

Bibliography

[1] D. Durand et al., Nuclear dynamics in the nucleonic regime, Series in Fundamental and Applied Nuclear Physics (Taylor & Francis, 2000)

[2] V. Baran et al., *Phys. Rep.* **410** 335 (2005)

[3] R. Kaufmann and R. Wolfgang, *Phys. Rev.* **121** 192 (1961)

[4] W. U. Schröder et al., *Phys. Rep.* **45** 301 (1978)

[5] W. Reisdorf, *Nucl. Phys. A* **630(1)** 15 (1998)

[6] J. A. Hauger et al., *Phys. Rev. Lett.* **77** 235 (1996)

[7] P. Hodgson *Nature* **292** 671 (1981)

[8] Proceedings of a Specialists' Meeting on Preequilibrium Nuclear Reactions, Semmering, Austria, 10th-12th February 1988

[9] Y. Zhang et al., *Phys. Rev. C* **85** 024602 (2012)

[10] B. Borderie & M. F. Rivet, *Progress in Particle and Nuclear Physics* **61(2)** 551 (2008)

[11] E. Plagnol et al., *Phys. Rev. C* **61** 014606 (1999)

[12] J. Lukasik et al., *Phys. Rev. C* **55** 1906 (1997)

[13] S. Piantelli et al., *Phys. Rev. C* **76** 061601 (2007)

[14] E. De Filippo et al., *Phys. Rev. C* **86** 014610 (2012)

[15] M. Di Toro, A. Olmi & R. Roy, *Eur. Phys. J. A* **30** 65 (2006)

[16] D. E. Fields et al., *Phys. Rev. Lett.* **69** 3713 (1992)

[17] G. Poggi, *Nucl. Phys. A* **685** 296 (2001)

[18] F. Bocage, *Annual Review of Nuclear and Particle Science* **43** 379 (1993)

[19] F. Bocage, *37th International Winter Meeting on Nuclear Physics, Bormio, Italy* (1999) 241-256

[20] H. Johnston et al., *Physics Letters B* **371** 186 (1996)

[21] J. F. Dempsey et al., *Phys. Rev. C* **54** 1710 (1996)

[22] P. Danielewicz & J. Lee, *Nucl. Phys. A* **818** 36-96 (2009)

[23] L. W. Chen et al., *Eur. Phys. J. A* **50** 29 (2014)

[24] X. Viñas et al., *Eur. Phys. J. A* **50** 27 (2014)

[25] M. Di Toro et al., *J. Phys. G: Nucl. Part. Phys.* **37** 083101 (2010)

[26] G. Ademard et al., *Eur. Phys. J. A* **50** 33 (2014)

[27] M. B. Tsang, W. G. Lynch, H. Xi and W. A. Friedman, *Phys. Rev. Lett.* **78** 3836 (1997)

[28] M. B. Tsang et al., *Phys. Rev. Lett.* **86** 5023 (2001)

[29] A. Ono et al., *Phys. Rev. C* **68** 051601(R) (2003)

[30] V. Baran et al., *Phys. Rev. C* **72** 064620 (2005)

[31] V. Baran, M. Colonna, V. Greco, M. Di Toro, *Physics Reports* **410** 5–6 (2005), 335-466

[32] C. Fuchs & H. H. Wolter, *Eur. Phys. J. A* **30** 5–21 (2006)

[33] J. Dechargé and D. Gogny, *Phys. Rev. C* **21** 1568 (1980)

[34] M. Kleban et al., *Phys. Rev. C* **65** 024309 (2002)

[35] B. Cochet et al., *International Journal of Modern Physics E* **13** 187-190 (2004)

[36] P. G. Reinhard & M. Bender, Extended Density Functionals in Nuclear Structure Physics, *Lecture Notes in Physics* **641** 249 (2004)

[37] P. Ring, Extended Density Functionals in Nuclear Structure Physics, *Lecture Notes in Physics* **641** 175 (2004)

[38] B. D. Serot, J. D. Walecka, *Int. J. Mod. Phys. E* **6** 515 (1997)

[39] R. J. Furnstahl, *Lect. Notes Phys.* **641** 1 (2004)

[40] M. Lutz, B. Friman, Ch. Appel, *Phys. Lett. B* **474** 7 (2000)

[41] P. Finelli, N. Kaiser, D. Vretenar & W. Weise, *Eur. Phys. J. A* **17** 573–578 (2003)

[42] D. Vretenar & W. Weise, *Lect. Notes Phys.* **641** 65 (2004)

[43] V. R. Pandharipande, R. B. Wiringa, *Rev. Mod. Phys.* **51** 821 (1979)

[44] A. Akmal, V.R. Pandharipande, D.G. Ravenhall, *Phys. Rev. C* **58** 1804 (1998)

[45] K. A. Brueckner, J. L. Gammel, *Phys. Rev.* **109** 1023 (1958)

[46] M. Jaminon, C. Mahaux, *Phys. Rev. C* **40** 354 (1989)

[47] W. Zuo, A. Lejeune, U. Lombardo, J.F. Mathiot, *Nucl. Phys. A* **706** 418 (2002)

[48] X. R. Zhou, G. F. Burgio, U. Lombardo, H. J. Schulze, W. Zuo, Phys. Rev. C 69, 018801 (2004)

[49] B. ter Haar, R. Malfliet, *Phys. Rep.* **149** 207 (1987)

[50] R. Brockmann, R. Machleidt, *Phys. Rev. C* **42** 1965 (1990)

[51] F. de Jong, H. Lenske, *Phys. Rev. C* **58** 890 (1998)

[52] T. Gross-Boelting, C. Fuchs, A. Faessler, *Nucl. Phys. A* **648** 105 (1999)

[53] E. Schiller, H. Müther, *Eur. Phys. J. A* **11** 15 (2001)

[54] C. Fuchs, *Lect. Notes Phys.* **641** 119 (2004)

[55] E. van Dalen, C. Fuchs, A. Faessler, *Phys. Rev. C* **72** 065803 (2005)

[56] H. Müther, A. Polls, *Prog. Part. Nucl. Phys.* **45** 243 (2000)

[57] W. H. Dickhoff, C. Barbieri, *Prog. Part. Nucl. Phys.* **52** 377 (2004)

[58] J. Carlson, J. Morales, V.R. Pandharipande, D.G. Ravenhall, *Phys. Rev. C* **68** 025802 (2003)

[59] M. B. Tsang et al., *Phys. Rev. C* **86** 015803 (2012)

[60] C. J. Horowitz and J. Piekarewicz, *Phys. Rev. Lett.* **86** 5647 (2001)

[61] Bao-An Li et al., *Phys. Lett. B* **727** 276 (2013)

[62] M. Colonna, M. Di Toro, G. Fabbri and S. Maccarone, *Phys. Rev. C* **57** 1410 (1998)

[63] V. Baran et al., *Nucl. Phys. A* **703** 603 (2002)

[64] The FAZIA Collaboration - `http://fazia.in2p3.fr/`

[65] R. Bougalt et al., *Eur. Phys. J. A* **50**, 47 (2014)

[66] S. Carboni et al., *Nucl. Instrum. Methods A* **664**, 251 (2012).

[67] L. Bardelli et al., *Nucl. Instrum. Methods A* **654**, 272 (2011)

[68] J. Pouthas et al., *Nucl. Instrum. Methods A* **357**, 418 (1995)

[69] S. Upadhyaya, *Acta Phys. Pol. B* **51**, 399 (2020)

[70] F. Salomon et al., *2016 JINST* **11** C01064

[71] S.Valdré et al., *Nucl. Instrum. Methods A* **930**, 27 (2019)

[72] G. Pastore et al., *Nucl. Instrum. Methods A* **860**, 42 (2017)

[73] D. Gruyer et al., *Nucl. Instrum. Methods A* **847**, 142 (2017)

[74] M. F. Rivet et al., *2013 J. Phys.: Conf. Ser.* **420** 012160

[75] S. Aiello et al., *Nuclear Physics A* **583** (1995) 461

[76] J. Łukasik et al., *Nucl. Instrum. Methods A* **709** (2013) 120

[77] P. Ottanelli, Ph.D. Thesis (University of Florence, 2019)

[78] J. Alarja et al., *Nucl. Instrum. Methods A* **242** (1986) 352

[79] F. Benrachi et al., *Nucl. Instrum. Methods A* **281** (1989) 137

[80] KaliVeda Toolkit - `http://indra.in2p3.fr/kaliveda/`

[81] INDRA Collaboration - `http://indra.in2p3.fr/`

[82] ROOT Data Analysis Framework - `https://root.cern/`

[83] S. Barlini et al., *Phys. Rev. C* **87** 054607 (2013)

[84] S. Piantelli et al., *Phys. Rev. C* **101** 034613 (2020)

[85] S. Piantelli et al., *Phys. Rev. C* **103** 014603 (2021)

[86] A. Camaiani et al., *Phys. Rev. C* **103** 014605 (2021)

[87] G. Ademard et al., *Phys. Rev. C* **83** 054619 (2011)

[88] G. Cardella et al., *Phys. Rev. C* **85** 064609 (2012)

[89] A. L. Keksis et al., *Phys. Rev. C* **81** 054602 (2010)

[90] I. Lombardo et al., *Phys. Rev. C* **84** 024613 (2011)

[91] S. Piantelli et al., *Phys. Rev. C* **88** 064607 (2013)

[92] L. Lassen et al., *Phys. Rev. C* **55**, 1900 (1997)

[93] M. Wang et al., *CPC (HEP & NP)*, 2012, **36** (12): 1603–2014

[94] D. Bazin et al., *Nucl. Phys. A* **515** 349 (1990)

[95] S. Piantelli et al., *Phys. Rev. Lett.* **88** 052701 (2002)

[96] S. Hudan et al., *Phys. Rev. C* **70** 031601(R) (2004)

[97] E. De Filippo et al., *Phys. Rev. C* **71** 064604 (2005)

[98] C. P. Montoya et al., *Phys. Rev. Lett.* **73** 3070 (1994)

[99] J. Colin et al., *Phys. Rev. C* **67** 064603 (2003)

[100] Y. Kanada-En'yo, M. Kimura and A. Ono, *Progress of Theoretical and Experimental Physics* **2012**(1) 01A202 (2012)

[101] M. Papa, T. Maruyama and A. Bonasera, *Phys. Rev. C* **64** 024612 (2001)

[102] M. Papa, G. Giuliani and A. Bonasera, *Journal of Computational Physics* **208**(2) (2005) 403-415

[103] D. Lacroix, A. Van Lauwe and D. Durand, *Phys. Rev. C* **69**, 054604 (2004)

[104] D. Lacroix, A. van Lauwe and D. Durand, *International Workshop on Multifragmentation and Related Topics (IWM2003)*, Nov 2003, CAEN, France. pp.58-61.

[105] D. Durand, *Nucl. Phys. A* **541**, 266 (1992)

[106] R. J. Charity, *Joint ICTP-IAEA Advanced Workshop on Model Codes for Spallation Reactions, IAEA, Trieste, Italy*, 2008, p. 139

[107] S. Hudan et al., *Phys. Rev. C* **67**, 064613 (2003)